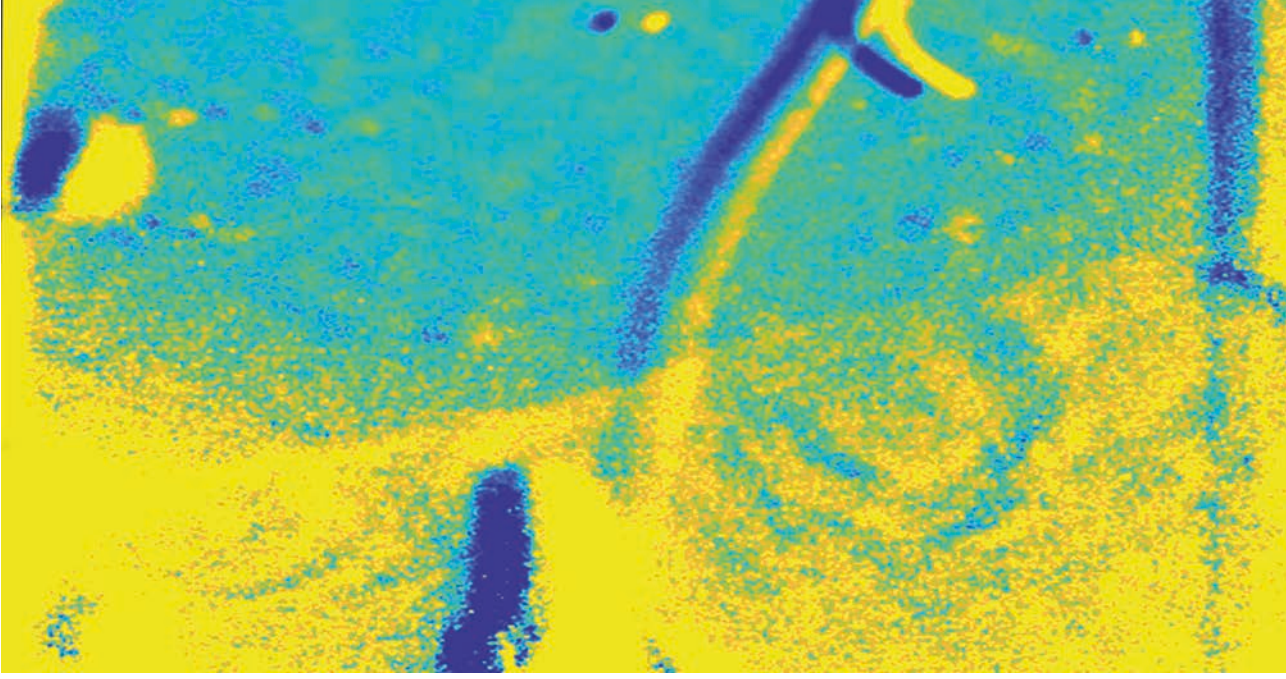

FAU Studien aus dem Maschinenbau 446

Moritz Späth

Assessment of microcirculation by shifted position-diffuse reflectance imaging (SP-DRI)

FAU University Press

Moritz Späth

Assessment of microcirculation by shifted position-diffuse reflectance imaging (SP-DRI)

FAU Studien aus dem Maschinenbau

Band 446

Moritz Späth

Assessment of microcirculation by shifted position-diffuse reflectance imaging (SP-DRI)

Dissertation aus dem Lehrstuhl für Photonische Technologien (LPT), Prof. Dr.-Ing. Michael Schmidt

Erlangen
FAU University Press
2024

Bibliografische Information der Deutschen Nationalbibliothek:
Die Deutsche Nationalbibliothek verzeichnet diese Publikation in der Deutschen Nationalbibliografie; detaillierte bibliografische Daten sind im Internet über http://dnb.d-nb.de abrufbar.

Kontakt: Moritz Späth, Friedrich-Alexander-Universität Erlangen-Nürnberg, (ROR https://ror.org/00f7hpc57), https://orcid.org/0000-0002-9852-1212

Bitte zitieren als
Späth, Moritz. 2024. *Assessment of microcirculation by shifted position-diffuse reflectance imaging (SP-DRI).* FAU Studien aus dem Maschinenbau Band 446. Erlangen: FAU University Press. DOI: 10.25593/978-3-96147-760-9

Der vollständige Inhalt des Buchs ist als PDF über OPEN FAU
der Friedrich-Alexander-Universität Erlangen-Nürnberg abrufbar:
https://open.fau.de/home

Verlag und Auslieferung:
FAU University Press, Universitätsstraße 4, 91054 Erlangen

Druck: docupoint GmbH

ISBN: 978-3-96147-759-3 (Druckausgabe)
eISBN: 978-3-96147-760-9 (Online-Ausgabe)
ISSN: 2625-9974
DOI: 10.25593/978-3-96147-760-9

Assessment of microcirculation by shifted position-diffuse reflectance imaging (SP-DRI)

Beurteilung der Mikrozirkulation mittels Shifted Position-Diffuse Reflectance Imaging (SP-DRI)

Der Technischen Fakultät
der Friedrich-Alexander-Universität
Erlangen-Nürnberg

zur
Erlangung des Doktorgrades Dr.-Ing.

vorgelegt von

Moritz Späth, M.Sc.

aus Ingolstadt

Als Dissertation genehmigt
von der Technischen Fakultät
der Friedrich-Alexander-Universität Erlangen-Nürnberg

Tag der mündlichen Prüfung:	22.04.2024
Gutachter:	Prof. Dr.-Ing. Michael Schmidt
	Prof. Dr. Jürgen Popp
	(Friedrich-Schiller-Universität Jena)

Preface

This dissertation was written during my stay at the Institute of Photonic Technologies at the Friedrich-Alexander-Universität Erlangen-Nürnberg (FAU). In this respect, I would first and foremost like to thank Prof. Dr.-Ing. Michael Schmidt for giving me the opportunity to gain advanced scientific knowledge and to work on the topic outlined in this dissertation. I appreciate that you are providing an environment in which it is a pleasure to collaborate and discuss science.

I would like to thank the Medical Photonics research group for constantly allowing for discussions on the topic and for providing me with valuable advice. In particular, Dr.-Ing. Florian Klämpfl and Dr.-Ing. Martin Hohmann are to be mentioned in this regard. Moreover, I appreciate the support of the colleagues at the University Hospital Erlangen - in particular Prof. Dr. med. Dr. med. dent. Florian Stelzle and Dr. med. Dr. med. dent. Maximilian Rohde - in medical questions.

A significant contributor in making this work intellectually and financially possible was also the Erlangen Graduate School in Advanced Optical Technologies (SAOT). Thank you!

I wish to express my sincere gratitude to my family and friends for always paving my way and therefore enabling me to prepare this doctoral thesis.

Dedicated to Marie, Emil and Lotta.

Table of Contents

List of Symbols and Abbreviations

Symbol	*Unit*	*Description*
A_N	-	numerical aperture
A_{norm}	a.u.	modulation parameter
β_0	-	intercept
β_1	-	slope
CAD	-	computer aided design
CV	-	coefficient of variation
DRI	-	diffuse reflectance imaging
DRS	-	diffuse reflectance spectroscopy
FCD	-	functional capillary density
FDM	-	fused deposition modeling
FOP	-	fiber-optic plate
g	-	anisotropy factor
HSI	-	hyperspectral imaging
IDF	-	incident dark field illumination
K	a.u.	modulation parameter
K_{norm}	a.u.	modulation parameter
LED	-	light-emitting diode
MC	-	Monte Carlo
MTF	-	modulation transfer function
μ_a	mm^{-1}	absorption coefficient
μ_s	mm^{-1}	scattering coefficient
μ_s'	mm^{-1}	reduced scattering coefficient
n	-	refractive index
OPS	-	orthogonal polarization spectral imaging
PDMS	-	polydimethylsiloxane
px	-	pixel
R^2	-	coefficient of determination
$\bar{R}^2$	-	adjusted coefficient of determination

Symbol	*Unit*	*Description*
RBC	-	red blood cell
RF	-	random forest
RTE	-	radiative transfer equation
RTV	-	room-temperature-vulcanizing
SDF	-	sidestream dark field imaging
SDS	-	source detector separation
SEM	-	standard error of the mean
SERDS	-	shifted-excitation Raman difference spectroscopy
SNR	-	signal-to-noise ratio
SP-DRI	-	shifted position-diffuse reflectance imaging
SVP	-	superficial vascular plexus

List of Figures

List of Tables

1 Introduction

”Microcirculation describes the blood flow within the terminal section of the vascular system on the level of the capillary bed, the afferent arterioles and the efferent venules. It ensures the basic nutrient supply of the tissues and aims to keep the blood circulation going even in the event of a central change in the blood pressure [1].

In order to cope with these tasks, microcirculation is subject to local and systemic regulatory mechanisms [2]. The capillary bed as the location of the microcirculation thus fulfills two separate functions: On the one hand, superordinate regulatory mechanisms take effect there, on the other hand, the capillary bed itself influences the overall organism and the global circulatory situation of the individuum through local effects. As an example, large quantities of venous blood can be mobilised from the capillary bed or moved thereto in order to change the preload of the heart and thus the cardiac output, if necessary [3, 4].

Changes in capillary blood flow, peripheral resistance and microcirculation, however, do not only occur in physiological metabolic and circulatory states. Multiple diseases - ranging from diabetes mellitus to hypertension and autoimmune diseases - can be associated with a wide spectrum of microvascular dysfunctions, microangiopathies and microcirculatory disorders [2]. Furthermore, pathologic circulatory states such as those associated with hypovolemia can significantly influence the peripheral blood flow and the blood flow in the capillary bed [5]. In the worst case, this results in a generalised circulatory collapse with pathological circulatory dysregulation after the adaptability of the capillary system has been exhausted [6].

This means, in summary, that through adaptive reactions of the capillary bed, it is possible to influence both the local circulatory state of a limited body region as well as the patient’s overall blood circulation. Vice versa, local and superordinate processes cause (reactive) changes within the capillary bed. Based on the physiological correlations mentioned before, it can be assumed that monitoring the microcirculation could thus be useful to diagnose various local and systemic circulatory disorders and could be used to monitor critically ill patients [7, 8].” [P1]

”On the outer skin, changes in microcirculation can be observed by the unaided eye. In doing so, clinical signs such as capillary refill time, marbling of the skin (mottling score) or its temperature can be employed [7]. These skin signs can help in identifying pathological conditions, but they need to

be supplemented by further examination techniques and by considering the overall patient.

In the case of a hemorrhagic shock, for example, the primary effect on the level of microcirculation is a mobilization of volume out of the capillary bed and a reactive increase in peripheral resistance. The aim of this is to maintain central blood flow on the expense of peripheral blood flow (centralization). Initially, this results in intense vasoconstriction of the arteries and arterioles in skeletal muscle and skin, culminating in a breakdown of perfusion in the corresponding tissues. After about one minute, reperfusion follows with an alternating vasodilation of the arterioles and venules, respectively [6, 9].

The clinical example above clearly demonstrates the relationship between the microcirculation (i.e., more precisely, between its constriction and dilation) and a pathological state of perfusion. The challenging part, however, is the following: Even in the case of pathological processes, the adaptation of the capillary perfusion can lead to the clinical appearence of a healthy patient for a long time; the clinical signs mentioned in the above paragraph will fail. Decompensation will only occur when the adaptation mechanisms are exhausted. Thus, by detecting the body's early adaptation reactions at the level of the capillary bed and the microcirculation, non-physiological local and systemic circulatory conditions can be detected as early as possible, i.e. before they reach systemic relevance.

Various clinically applicable scores as well as instrumental, invasive and laboratory testings and easy-to-survey indices are available to help identify the impending or manifest state of a microcirculatory disorder in a patient. [...] It is critical to note that several of these methods leave room for interpretation and only provide indicators towards a diagnosis [10].

For monitoring critically ill patients as in the clinical example above, a stand-alone measurement method that allows a reliable detection of impending or manifest local or systemic circulatory malfunctions would be of great value." [P2] Within the framework of this doctoral thesis, a suitable method was developed from scratch: shifted position-diffuse reflectance imaging (SP-DRI). "It is an optical and thus non-invasive method based on the diffuse reflected light. [...] The method is quite easy to be implemented in practice and has the potential to serve as a stand-alone method [P1, P3]." [P2]

This doctoral thesis presents the SP-DRI method and explains the algorithms behind it in detail. It is set in relation to already existing diagnostic approaches for the assessment of the microcirculatory function. The current state of research on SP-DRI is described along with an outline of the future potential of this imaging technique.

2 State of the Art

2.1 Technologies assessing the state of microcirculation

"An impaired microcirculation may be suspected in the presence of mottled skin, acrocyanosis, slow recoloration time, or increased central to toe temperature gradient. These signs of impaired cutaneous perfusion lack specificity (and even sensitivity) for disclosing more central microcirculatory alterations." [11] This is also true for the observation of standard vital signs such as heart rate, blood pressure, oxygen saturation, laboratory data, a patient's fluid balance and electrocardiography [12]. Although this set of standard techniques may provide the clinician with indications for making a diagnosis, the specific scoring of the parameters leaves scope for interpretation [10]. Accordingly, a variety of more specific techniques for this use case has been developed over time.

This section provides an overview of relevant technologies and approaches for identifying "the impending or manifest state of a microcirculatory disorder in a patient" [P2]. "Various instrumental, invasive and laboratory tests as well as easy-to-use scores are available" [P1] for this purpose. It is, however, important to emphasise that there is no gold standard in this regard to date [13]. Accordingly, the different methods focus on (one or more) different parameters.

The functional capillary density (FCD) - the path length of perfused capillaries per area [14] - is suggested to be the strongest functional parameter for the assessment of microcirculation [15] and correlates with a poor outcome [11]. As a general rule, the perfusion of adjacent capillaries is significantly homogeneous under physiological conditions. In disease states (e.g. sepsis or low-flow conditions like haemorrhage or cardiogenic shock), however, a heterogeneous pattern is emerging: The FCD is decreasing in a way that "some areas become deprived of capillaries while others are not, so that perfused capillaries are in close vicinity to non-perfused capillaries" [11]. However, a sufficiently high spatial resolution is required to detect FCD, implying, as a consequence, that not all systems used to observe microcirculation are actually capable of assessing the heterogeneity of perfusion [11].

In general, morphological as well as functional parameters can be studied to assess microcirculation [16]. The former include FCD, vessel density and diameter, microcirculatory blood flow velocity and blood cell concentration [16] as well as an indirect assessment by measuring tissue oxygenation [11]. The latter are mainly focussing on microcirculatory endothelial function

and are based on pharmacological and occlusive tests [16]. The class of functional parameters is not considered in the context of this work as they are no monitoring techniques; a comprehensive review of reactivity tests can be found in the literature [17, 18].

The technologies to register morphological changes mainly can be grouped into two categories: Systems measuring microvascular perfusion and systems acquiring tissue oxygenation [11, 19]. This will be discussed in more detail below. Some of the methods presented in the following are commonly used in clinical practice, while others have not reached the state of market maturity.

Important to note: Although any microcirculation monitoring system can inherently only assess microcirculation in the monitored capillary bed, it is reasonable to assume that alterations of at least the same severity are also likely to occur at other sites [11]. Due to its good accessibility, the skin thus offers an appropriate spot for examination and "human cutaneous circulation could be used as a surrogate marker of systemic microvascular function in various diseases" [20].

2.1.1 Systems directly measuring microvascular perfusion

The most direct way to assess the status of the microcirculation is to use microscopy (microvideoscopic) and Doppler-derived techniques [11, 19]. In this context, the microscopy techniques are aiming on visualizing the vascular structures so that conclusions can be drawn based on an analysis of these images. Accordingly, organs can be examined that are only covered by a thin epithelial layer [11]. "For many years, the clinical approach to the direct intravital observation of microcirculation was restricted to the use of bulky capillary microscopes, which were mainly utilized on the nailfold capillary bed." [21] In the course of time, orthogonal polarization spectral imaging (OPS), sidestream dark field imaging (SDF) and incident dark field illumination (IDF) were then introduced successively, each to be regarded as a modification of the respective preceding approach [19]. With IDF, the skin surface (usually sublingual) is illuminated with light pulses ($\lambda = 530\,\text{nm}$) of 2 ms and subsequently an image of the surface is taken. With appropriate software, parameters such as vessel diameter and length can be quantified [23].

The advantage of these approaches is that the resolution of such systems theoretically can be tuned to capture the heterogeneity of the capillary blood flow and thus the FCD [23]. Despite this advantage, these systems have not found their way into clinical routine. Reasons for that include the technology-related relatively large design, implemented as a hand-held probe [19]. The

Table 1: Systems directly measuring microvascular perfusion [11, 17, 19–27].

Technique	Variable measured	Disadvantages
Nailfold video-capillaroscopy	Capillary density, flow and heterogeneity	high sensitivity to changes in ambient/body temperature, limited use in critically ill patients
OPS, SDF and IDF	Capillary density, flow, diameter, length and heterogeneity	Semiquantitative scoring, movement/pressure artefacts, continuos observation only in sedated patients, no accessibility of sublingual area under ventilation
Confocal Laser Scanning Microscopy	Capillary density and loop diameter, flow	limited penetration depth, space requirement of device, expensive, slow imaging speed
Laser Doppler flowme-try/imaging	Relative flow, relative perfusion	Large sampling volume (capillaries, arterioles, venules), only relative changes from baseline, movement artefacts
Doppler optical coherence tomography	Capillary density and loop diameter, relative flow	Interferometric setup, movement artefacts, expensive, lack of validation data to date, only relative (flow) changes from baseline
Laser speckle contrast imaging	Relative flow, relative perfusion	movement and other artefacts, limited penetration depth and scanning area, limited use in state of low perfusion, only relative changes from baseline, sensitivity to ambient light

sublingual measurements are therefore manually conducted by the clinician, resulting in point rather than continuous long-term measurements and potentially introducing inter-observer variability [28]. Likewise, observing the same tissue site over a longer period of time is not practical or only feasible in sedated patients [23]. Furthermore, the achievable resolution is still in need of improvement [19]. The individual limitations of those systems are listed in table 1.

The high resolution of the aforementioned procedures is in contrast to laser Doppler flowmetry, which is not able to trace information back to single capillaries: Even up-to-date devices are capturing volumes containing approximately 50 vessels (capillaries, arterioles, venules). The heterogeneity inherent to microcirculatory disorders is therefore not accessible with this approach. This disadvantage is compensated by the different Doppler imaging techniques and by laser speckle contrast imaging, but these techniques suffer from other specific drawbacks (see table 1).

2.1.2 Systems acquiring tissue oxygenation

The methods to be summarized under this category are measuring O_2 tension or saturation as they "reflect the balance between O_2 transport and O_2 consumption (...). These measurements are, therefore, influenced by flow but also by hemoglobin content, arterial pO_2, and O_2 consumption." [11]

Table 2 provides an overview of systems acquiring tissue oxygenation along with their individual major disadvantages. A significant proportion of the techniques listed there is (at least minimally) invasive. (Minimally) invasive methods have the disadvantage of being associated with complications and the risk of iatrogenic damage [32]. In addition, they often demand substantial time on the part of the clinical staff due to calibration, supply and care activities [29]. This is true for gastric tonometry [33], Clark electrodes (transcutaneous blood gas analysis) and pulmonary artery catheters [29]. Further techniques falling within this scope are the insertion of an arterial line for the intravascular measurement of blood pressure and a central venous catheter to determine the central venous pressure and the oxygen saturation of the superior vena cava [33]. They are not listed in table 2 as they are mainly used for monitoring shock patients rather than providing information on basic microcirculatory alterations.

In particular, the following applies: A method that is (minimally) invasive and time-consuming cannot be optimally suited for this application since there are a multitude of possible scenarios in clinical routine where those methods are not applied immediately and thus potentially too late for the individual patient [34].

Motivated by this, non-invasive approaches capable of providing equivalent information at a reduced risk of iatrogenic impairment have been investigated [10]. Among these, two established methods are sublingual pCO_2 tonometry - which provides data that correlates well with gastric pCO_2 values and is intended to replace the gastrointestinal measurement [35] - and pulse oximetry for the measurement of arterial oxygen saturation (to be classified within

Table 2: Systems measuring tissue oxygenation [10, 11, 19, 21, 26, 29–31].

Technique	Variable measured	Disadvantages
Near-infrared spectroscopy (NIRS)	Tissue O_2 saturation (S_tO_2), total tissue haemoglobin (HbT), tissue haemoglobin index (THI)	S_tO_2 non-specific (similar values in septic patients and healthy volunteers, huge inter-person variations between septic patients), large sampling volume (capillaries, arterioles, venules)
Photoacoustic tomography	HbT, O_2 saturation (SO_2)	Long image acquisition time, movement artefacts, limited spatial resolution, lack of validation data to date
Reflectance spectroscopy	SO_2	Large sampling volume (capillaries, arterioles, venules)
Hyperspectral imaging, polarisation spectroscopy	S_tO_2, THI	Limited resolution, movement artefacts, S_tO_2 non-specific, inaccuracies on dark skin
Gastric tonometry	Tissue CO_2, adequacy of flow (proportion of perfused capillaries)	Not applicable in patients with sepsis, discrimination between low flow and anaerobic metabolism difficult
Sublingual tonometry	Tissue CO_2, adequacy of flow	Discrimination between low flow and anaerobic metabolism difficult
Clark electrode	Partial pressure of oxygen (pO_2) in tissue	Not applicable in conditions of heterogeneity, large sampling volume (capillaries, arterioles, venules)
Pulmonary artery catheter	Venous oxygen saturation (S_vO_2)	Little information on alterations in microcirculation

near-infrared spectroscopy) [29]. The latter is not suitable for monitoring small capillaries as larger vessels dominate the measurement. For the detection of early changes in microcirculation, however, the assessment of systemic haemodynamic variables is of minor importance, the focus is on local effects

[36]. Furthermore, measurement errors are likely in patients suffering from reduced capillary perfusion, which is part of a microcirculation disorder [37].

The situation is similar for hyperspectral imaging (HSI) with its comparatively high procurement costs and a limited resolution as major drawbacks: Up-to-date systems achieve a resolution of 640 pixel (px) · 480 px at approximately 520 µm/px [38], which is not suitable for the detection of local effects. Thus, HSI does not allow for a direct assessment of the microcirculation either, but only for a rough estimation of its state (within the mentioned resolution) by simultaneously recording tissue oxygen saturation (S_tO_2) and other parameters [39, 40]. Consequently, although evidence of typical parameter patterns was found, for instance, in individuals with previously medically diagnosed sepsis, only partially significant differences were found between this group of individuals and healthy volunteers [39]. Thus, it cannot be assumed that HSI is able to detect the onset of microcirculatory changes at an early stage. This assumption is supported by the finding that there is no reliable interpersonal difference between S_tO_2 levels of healthy and diseased subjects. [30]. "In fact, S_tO_2 represents the oxygen saturations of all vessels with a diameter less than 1 mm (arterioles, capillaries, and venules) comprised in the sampling volume, with venules accounting for 75% of the blood volume." [41]

In addition, the typically long integration time of HSI systems is, on the one hand, not suitable for resolving dynamic processes and, on the other hand, requires immobilization of the patient. The latter is also necessary as HSI systems cannot be permanently attached to the patient due to their size - mobile use on an emergency ambulance as well as continuous monitoring are therefore in fact not possible. HSI has to be understood as a single-point measurement system.

2.1.3 Other approaches

Another way to evaluate the microcirculatory function is in the measurement of biomarkers, specifically lactate, pyruvate and hyaluronan. Studies have demonstrated that an increase in microcirculatory perfusion is related to lower lactate and hyaluronan levels; the lactate/pyruvate ratio is raised under the condition of septic shock [11]. The main limitation in this context is that these parameters lack sensitivity and specificity. Moreover, they capture the patient's situation with a certain time delay only. Specifically, this means that one "cannot detect alterations in microvascular perfusion before they are associated with cellular hypoxia" [11].

2.2 Capillary diameter variations as parameter

In the preceding section of this thesis, a distinction was made between systems that are capable of directly assessing microvascular perfusion and systems aiming at the same goal, but in an indirect manner via the acquisition of tissue oxygenation. The latter were found to be not ideal for monitoring microcirculation mainly because they rely on a non-specific parameter, cover a sampling volume that is too large or have a limited resolution. However, also the systems belonging to the first category mentioned are not fully satisfactory: The Doppler systems, in particular, are prone to artefacts, while the microvideoscopic techniques are of limited use in critically ill patients or those under ventilation. It can thus be concluded that there is still a need for improvement.

In the introductory chapter of this thesis, the main tasks of microcirculation have already been pointed out. It has been explained that microcirculation is subject to local and systemic regulatory mechanisms in order to accomplish these tasks. "The parameter that enables this regulatory function is the constriction or dilation of the arterioles or venules. Moreover, there is some evidence that also the capillary bed itself is capable of active and passive changes in caliber [42–47]. This change in diameter causes increased or decreased blood flow in the capillary bed. Thus, (...) the predominant reaction of the capillary bed and its afferent and efferent vessels to different metabolic and circulatory situations is - to put it simply - a change in the capillary blood flow due to a variation in the capillaries' diameter." [P1]

To overcome the deficits of the currently existing monitoring systems, it is necessary to rely on direct physiological correlates of the microcirculation (and its alterations, respectively). With constriction/dilation of the microvessels, a parameter to focus on is available. Diffuse reflectance spectroscopy (DRS) is considered to offer the potential to capture this parameter. According to table 2, the limitation of DRS to date is the large sampling volume. Literature results, however, indicate the scalability of this method. This will be outlined in the following.

2.3 Scalability of diffuse reflectance spectroscopy

DRS has been widely investigated as a tool for the non-invasive characterization of biological tissues and has proven to be an effective technique for the determination of optical and physiological properties of the skin. To determine the absorption and scattering properties of the tissue of interest, the steady-state diffuse reflectance of the skin surface is assessed [49]. In this regard, DRS is based on the assumption that light is mainly forward scattered

in skin so that photons travelling back to the surface have been scattered many times on average [50].

The achievable penetration depth depends in particular on the source-detector separation (SDS; distance between the spots of entrance and detection of a photon) [51] and the illumination wavelength [52] and is in the range of 100 µm to 1 mm [53]. A typical experimental setup for measuring the diffuse reflectance of biological tissues consists of a light source, a spectrometer and a fibre-optic probe used to direct light towards or away from the site of study [54]; a sketch for illustration can be found in figure 1. Following this, the quantitative estimations of optical tissue properties using DRS are to be understood as mean values of the respective volume elements [49].

The method of DRS has inherent advantages: A compact design with low-cost components is possible, and the patient can move freely during the measurements. DRS is not dependent on constant measurement or ambient conditions (ambient light, measurement distance) and allows short measurement durations.

As described previously in section 2.1.2, the main reason why existing DRS systems cannot be used or adapted for the detection of microcircular alterations is their limited spatial resolution. It depends on the diameter of the fibres [53] and is too low to resolve the spatial pattern of the microvessels with their diameters of around 10 µm (those micro-vessels of the capillary network specify the target resolution to be achieved; refer to section 2.4 for the anatomical dimensions of the human microvascular system). Typically,

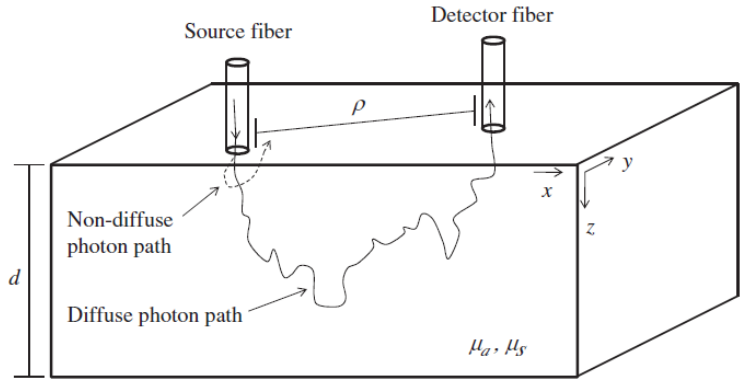

Figure 1: Exemplary sketch of a DRS setup. The source-detector separation (here: ρ) between the source and the detector fibre is shown. Only those photons that have been scattered many times can be regarded as "diffuse". [48]

optical fibres with core diameters of, for example, 100 µm [51], 300 µm [52] or 600 µm [55] are used for detection in DRS setups. Additionally, the number of optical fibres in those setups is usually small, resulting in a poor lateral resolution.

Nevertheless, the general feasibility - i.e. an investigation of the capabilities on a non-anatomical scale - of DRS to derive spatially resolved haemoglobin concentrations within turbid media has already been shown in the literature with the help of optical phantoms and Monte Carlo (MC) simulations. There is, for example, a simulation study demonstrating that vessel diameters of 1 mm can be localized at depths of 1 mm to 5 mm on the basis of the diffuse reflection [56].

In laboratory experiments on this topic, optical phantoms mimicking vessels with a diameter of 200 µm [57] or 300 µm [58], respectively, and three discrete wavelengths were used (spacing of two neighbouring vessels: 500 µm). The illumination was realized by 28 spatially arranged and serially switched optical fibres with a core diameter of 50 µm each, and another such optical fibre was used to derive the diffuse reflection. It was demonstrated that the spatial configuration of the vessels could be reproduced after an appropriate data processing step. Moreover, a sufficiently high tissue penetration depth was found [59].

Similarly, DRS was found to be functional in a scanner-based approach in which a detection fibre (core diameter: 10 µm) was moved over a scattering phantom with embedded absorbing channels of rectangular cross-section (depth of one channel: 30 µm; width: 34 µm; distance between two neighbouring channels: 82 µm) aligned parallelly to the surface of the phantom: A change in contrast was observed on the camera image matching the pattern of the absorbing structures [60]. Besides the fact that the cross-section of the structures is multiple times larger than that of human capillaries, these authors were also able to demonstrate a proof of concept.

If the lateral resolution of the DRS technique is to be increased significantly, it might not be sufficient to solely decrease the core diameters of the detection fibres, but rather to completely overcome the previously mentioned approach of detecting the diffuse reflection with single fibres. In this context, it is also expedient to abandon the spectral decomposition of the detected light at the expense of, for example, a serial illumination with single wavelengths. This allows to establish setups in which the diffuse reflection is directly - i.e. without the introduction of dispersive optical components - mapped onto a camera with the help of lenses, fibre bundles or a fibre-optic plate (FOP). Generally, this approach is referred to as diffuse reflectance imaging (DRI). In this way, for example, a lateral resolution of 16.7 µm could be achieved (pixel

pitch at the camera: 1.67 µm; single fibre diameter within the FOP: 6 µm) [61]. Note: Theoretically, it is also possible to apply the camera chip directly to the surface of interest [62]; due to the fact that the circuit board significantly extends beyond the photosensitive area of the camera chip, illumination within a reasonable SDS, however, is then constructively quite challenging to be implemented (if at all).

In addition to constructional considerations, algorithmic aspects must also be taken into account when trying to increase lateral resolution. In this context, it is worthwhile reviewing recent developments within other spectroscopic approaches: In Raman spectroscopy, for example, the technique of shifted-excitation Raman difference spectroscopy (SERDS) allows to significantly increase the signal-to-noise ratio (SNR) by eliminating the fluorescence background as well as systematic noise [63]. This enables the observation of comparatively very weak Raman peaks. With SERDS, "the subtraction of two spectra from each other acquired with slightly different excitation wavelengths makes the elimination of the fluorescence background possible, while a Raman difference spectrum remains." [63] Such approaches are not yet known in the context of DRS or DRI, respectively.

2.4 Human skin anatomy

In terms of the dimensions, the studies just outlined do not adequately represent the human vascular anatomy. Since the microcirculatory network - which is central to the present doctoral thesis - is particularly localized in the papillary dermis [65], this statement will be justified in the following by referring to the vascular situation in this skin layer.

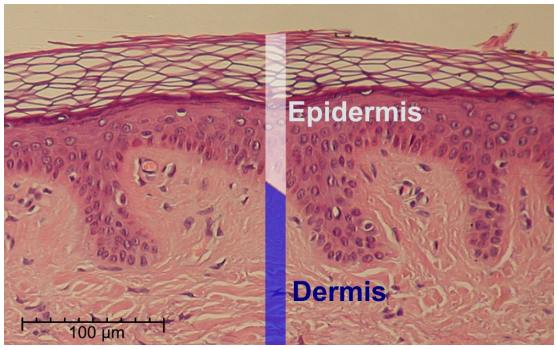

Figure 2: Exemplary illustration of a longitudinal section through mammalian skin. The distinctive structure of the stratum corneum made up of dead corneocytes is particularly prominent. [64]

In general, human skin consists of three layers, namely epidermis, dermis and subcutaneous tissue. The two layers mentioned first can be further differentiated. For the epidermis, a rough subdivision into non-living and living epidermis can be made [66]. The former - called stratum corneum - "consists of dead corneocytes and functions as a barrier to protect underlying tissue [67]. In this manner, the stratum corneum exhibits high values for μ_s', especially when compared to the air surrounding the skin [68]." [P2] The epidermis is absent of vessels [66]. Its thickness is around 100 µm, of which about 20 µm relate to the stratum corneum [69]. An exemplary microscope image is given in figure 2.

The dermis is basically divided into two layers, the papillary dermis and the reticular dermis. It is traversed by two horizontal vascular plexuses: A superficial one within the papillary dermis at the interface between papillary and reticular dermis and a deep one at the dermis-subcutis junction. Vertical capillary loops extend from the superficial vascular plexus (SVP) to the tips of the dermal papillae [65, 70]. Therefore, the situation is as follows: "The vessels in the papillary dermis are composed entirely of terminal arterioles, arterial and venous capillaries, and postcapillary venules. The majority of vessels, however, are postcapillary venules, the physiologically most reactive segment of the microcirculation." [71] In the deep plexus, conversely, larger arterioles and venules dominate [70]. The thickness of the dermis varies with the bodily region; it is, roughly stated, 150 µm for the papillary dermis, 100 µm

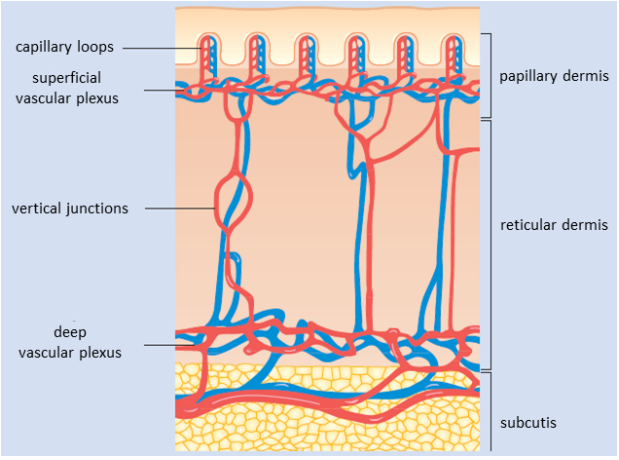

Figure 3: Sketch of the microvasculatory system within human skin. A description of the elements depicted can be found in the running text. Figure adapted from [70].

for the superficial plexus, 1 mm to 4 mm for the reticular dermis and 100 µm for the deep plexus [66]. Figure 3 illustrates what has been described so far.

Meanwhile, the following is known about the diameters of the aforementioned segments of the microcirculatory system: In general, "the microvessels in the papillary dermis vary in diameter from 10 µm to 35 µm, but most are in the 17 µm to 22 µm range. (...) The arterioles in the papillary dermis vary from 17 µm to 26 µm in diameter and represent terminal arterioles. (...) The arterial capillary, the next contiguous microvascular segment, has an outside diameter of 10 µm to 12 µm. (...) As the arterial capillary is traced, the basement membrane material progressively begins to develop lamellae within its homogeneous framework until a segment is reached in which the entire vascular wall is multilaminated. (...) The outside diameters of the vessels remain at 10 µm to 12 µm. (...) [This] venous capillary connects with the postcapillary venule, a vessel whose external diameter increases from 12 µm to 35 µm." [71] Values on a similar scale have been replicated several times [50, 65, 72].

As described above and shown in figure 3, capillaries are present in the skin in the form of capillary loops. In general, they are perpendicular to the skin surface (an exception is the nailfold region with a parallel arrangement). On average, these capillary loops have a width of 44 µm ± 5 µm and a height of 240 µm ± 38 µm. The distance between two neighbouring capillary loops (intercapillary distance) is on average 137 µm ± 13 µm [72]. By one capillary

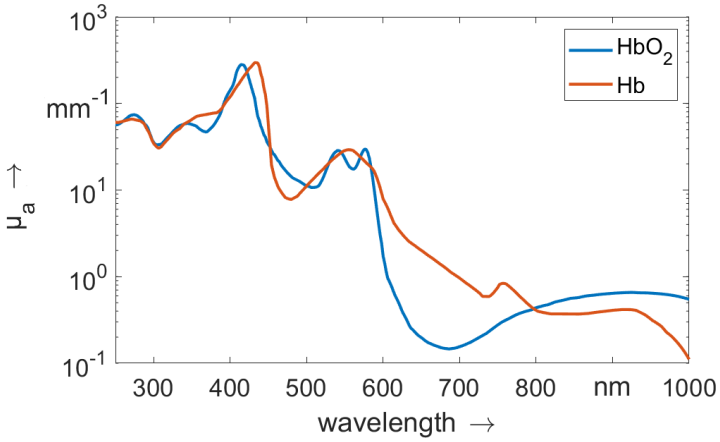

Figure 4: Absorption curves of oxyhaemoglobin, HbO_2, and deoxyhaemoglobin, Hb, for a typical concentration of 150 g haemoglobin per litre of blood. Plot prepared based on molar extinction coefficient data retrieved from [73].

loop, a skin surface of approximately 2.1×10^4 µm^2 is supplied with blood [65].

The capillaries are perfused with blood. Blood owes its typical red colour to haemoglobin, the blood pigment found in the red blood cells (RBCs) of vertebrates. In the wavelength range of 250 nm to 1100 nm, the optical properties of whole blood can be approximated very well by those of haemoglobin. This is true as the absorption contribution of the RBCs is up to three orders of magnitude above that of the other blood constituents, and RBCs dominate the scattering to the same extent (stemming from the refractive index difference between RBCs and their surrounding blood plasma) [74, 75]. For all blood cells, strong forward scattering is characteristic [74].

Depending on the molecule bound to haemoglobin, the optical properties of blood vary slightly. The absorption spectra that result for the two predominant forms of haemoglobin - oxyhaemoglobin, HbO_2, and deoxyhaemoglobin, Hb [75] - are plotted in figure 4 for a typical concentration of 150 g haemoglobin per litre of blood [76].

2.5 Monte Carlo simulation of photon transport

To be able to answer research questions like those underlying this doctoral thesis in a simulative way, models of photon transport in tissue are usually employed. While a description of the effects using Maxwell's equations is theoretically possible, their solution requires a precise knowledge of each structure within the medium under investigation, leading to an extreme complexity in the case of human skin [50]. Therefore, various approximations are available; the most commonly used one in the field of skin optics is the radiative transfer equation (RTE) [77]. It considers light transport in the form of rays and as a function of the absorption and scattering coefficient and the anisotropy factor [50]. To solve RTE, it is again necessary to adopt appropriate approximations and statistical methods, mainly depending on whether absorption or scattering dominates in the medium [77].

A computationally low-demanding solution of the RTE is the diffusion approximation, a well-established analytical (deterministic) method in the field of biophotonics [78]. The applicability of this approximation is limited to media for which $\mu_s' \gg \mu_a$ holds, a condition that is satisfied for biological tissue only in the wavelength range from 600 nm to 900 nm [79]. Moreover, a homogeneous and semi-infinite sample [80] with a large SDS is assumed [79]. Near to interfaces and light sources, the diffusion approximation gives inadequate results [81].

Due to the limitations mentioned above, the present doctoral thesis will not make use of the diffusion approximation. Instead, MC simulations of photon transport will be used for the simulative assessment of the research questions. "In case of radiative transfer in biological tissue, the MC method is a method to estimate the exact solution of RTE" [69] by tracing photons which undergo numerous scattering and absorption events. It is a numerical (stochastic) approach [54]. MC simulations are often time-consuming, especially for precise approximations. Nevertheless: As they do not require any significant approximations, MC simulations are acknowledged as the gold standard in modelling photon transport in heterogeneous media like skin [82].

The basic principle of a MC simulation of photon transport is straightforward. The essential steps are driven by random processes and as follows (to focus on the key aspects, details such as boundary conditions, layers or different beam geometries will not be discussed) [69, 83, 84]:

- Important simulation parameters have to be defined during initialization, including the dimensions of the volume and its absorption coefficient μ_a, scattering coefficient μ_s, anisotropy factor g and refractive index n.
- The first photon packet is launched at its initial position in its initial direction with its initial weight w (mostly $w = 1$).
- The step size is calculated as a function of μ_a and μ_s to determine the new position of the photon packet.
- To account for absorption, the weight of the photon packet must be adjusted at the new position: While a portion of $\frac{\mu_a}{\mu_a+\mu_s}$ is absorbed, a portion of $\frac{\mu_s}{\mu_a+\mu_s}$ is maintained for the next cycle.
- Scattering is considered by determining a new direction of the photon packet according to a phase function (mostly Henyey-Greenstein).
- If the weight of the photon packet is still above a certain threshold after these steps, the process is repeated (starting from calculating a new step size).
- If, in contrast, the weight of the photon packet drops below the threshold value, this photon packet is terminated. To conserve energy, usually the Russian roulette method is used: A random number between 0 and 1 "is generated; and if this random number is less than a small fraction called chance, typically 0.10, then the photon weight is increased by dividing w by chance. For chance = 0.10, this would be a 10-fold increase in w. Otherwise, the photon is terminated. Consequently, 9 out of 10 times the photon is terminated, but 1 out of 10 times the photon's weight is increased 10–fold and the photon continues to propagate. The result is that photons are usually terminated, but energy is conserved by the occasional surviving photon being given extra weight." [83]

- The simulation will continue with the initialization of a new photon packet until the specified number of photon packets to be launched is reached.

Typically, the output of a MC simulation comprises the energy absorbed within each voxel of the simulation volume. Moreover, the positions at which the photon packets have left the volume as well as their weights may be of interest. In general, any parameter can be tracked in the course of the simulation, allowing the output to be tailored to almost any research question.

Up to now, numerous MC software implementations have been released, each having its specific strengths and weaknesses. In particular, cubic voxels are used [85–88]. "Some solvers assume certain geometrical symmetries (usually cylindrical) [83] or make other numerical approximations [89] to speed up the calculations, which may otherwise in some cases be prohibitively time-consuming. Over the years, many advanced methods have been demonstrated simulating effects such as anisotropic light propagation [90], light polarization [91, 92], and fluorescence [93]. The simulation speed has been increased using CPU [94] and GPU [85, 95, 96] parallelization and polyhedral meshing of the geometry [90, 97]." [98]

2.6 Optical Phantoms

Besides the simulative perspective, also the laboratory-experimental domain is highly relevant in optics. In this context, objects that mimic tissues are termed phantoms. Their availability is essential when developing diagnostic imaging systems: During design and establishment of novel imaging techniques, they are used for principle functionality tests [99], and later on for calibrating optical devices and performing reference measurements [100].

The prerequisite for the fabrication of phantoms is a thorough "understanding of the key physical and biochemical characteristics of tissue that influence its interaction with light" [99]. In this regard, besides certain application-specific properties (e.g. matching sound velocity or elasticity in case of photoacoustics), in particular the optical properties of the phantom must match those of the tissue to be mimicked. As already introduced in section 2.5, these are μ_a, μ_s, g and n. Typically, absorbers (adjustment of μ_a) and scatterers (adjustment of μ_s and g) are added to a transparent host material - which determines n - during the manufacturing process [99, 101, 102].

In general, there is a variety of host materials available. Usually, the easiest option is to prepare (liquid) phantoms based on water ($n \approx 1.34$). For flexible phantoms, hydrogels (gelatin, agar, polyacrylamide) can be used as matrices ($n \approx 1.35$). A main benefit of the materials mentioned so far is that they are biologically compatible; however, they have the disadvantage

of a relatively short usable lifespan of a few weeks to months, so that these phantoms are not stable. If stability of properties over time is required and biological compatibility is not necessary, polyurethane ($n \approx 1.50$), polyester or epoxy resin ($n \approx 1.54$) as well as room-temperature-vulcanizing (RTV) silicone ($n \approx 1.40$) can be used. Phantoms made of the latter material are flexible, the other materials solidify [99, 100, 103]. "There may be no great advantage of one material over another. For example, silicone more closely matches the mechanical properties of tissue and may be cast into arbitrary shapes, whereas epoxy, polyurethane, and polyesters are easier to machine after casting. Typically, the selection of a material is determined by the choice of absorbers and their stability in that medium." [100]

Various materials are available as absorbers. Quite frequently, ink is used due to its almost flat absorption spectrum over a wide wavelength range and its stability in all of the host materials mentioned. Blood or blood components, for example, can be used in water-based and gelatin/agar phantoms. Organic molecules, on the other hand, are not stable in resins and RTV silicones [99, 104].

For introducing scattering, the substances available are lipid microparticles (milk, oil, fat, intralipid), polymer microspheres (polyester, polystyrene, latex) and metal/metalloid oxide powders (aluminium oxide, titanium dioxide, silicon dioxide). As they are typically added in very low concentrations, their choice can usually be made independently of the host material; however,

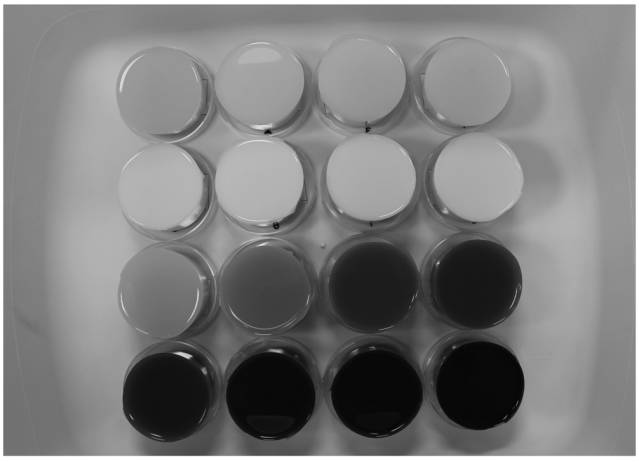

Figure 5: Exemplary illustration of 16 different PDMS phantoms. Each of them features different concentrations of scatterers (titanium dioxide) and absorbers (solution of nigrosin and ethanol). [102]

lipids are commonly only used in liquid phantoms. All of the additives listed are biocompatible, and with the exception of lipids, they are also all durable. The microspheres nearly perfectly follow Mie theory, allowing their scattering properties to be accurately predicted; however, since they are significantly more expensive than aluminium oxide and titanium dioxide, the latter offer a very good compromise with still good accuracy for the majority of applications [99, 100, 104].

Another key aspect in the fabrication of phantoms is the possibility of creating regions where the optical properties differ. These can be certain geometries (like multiple layers to mimic skin) or inclusions (e.g. to mimic tumours) [99]. This ability is mainly influenced by the host material: It is practically not possible to obtain a layered structure in liquid phantoms, and inclusions can only be introduced using external components. The degree of freedom increases for hydrogel phantoms, as these materials can be cut and moulded to allow for inhomogeneities. The maximum flexibility in design is offered by the resins and silicones; with these, the (liquid) raw material is poured into the mould and subsequently cures [100]. This allows to cast layers with different optical properties one after (and over) another, and inclusions can be created [102, 105]: For instance, in polydimethylsiloxane (PDMS), a commonly used silicone oil [106], channels with a diameter of 10 µm were designed using soft lithography techniques; intralipid was then pumped through these channels [107].

3 Hypotheses

Summarizing the findings described so far, there are relevant requirements for a system enabling an early and reliable detection of a microcirculation disorder: It must acquire an essential parameter in a non-invasive way and provide accurate, stable and continuous measurements as well as trend analyses without the need for sedation or fixation of the patient in order to constantly provide information about the patient's current condition [29].

As outlined in the state of the art section, DRI - unlike the other existing methods described - does not suffer from any inherent drawback in this context and is therefore to be regarded as the optimal method for addressing this objective. DRI is generally capable of deriving spatially resolved haemoglobin concentrations within turbid media and thus vasoconstriction/vasodilation - there is, however, still a need for research regarding the scalability of this technique to potentially also be useful in anatomically correct conditions. This is where the present doctoral thesis steps in by postulating that DRI combined with aspects borrowed from SERDS - which leads to a substantial increase in SNR in the context of Raman spectroscopy - could solve this problem and might leverage the potential of DRI similar to once that of Raman spectroscopy (compare section 2.3). The resulting algorithm, which was developed and described for the first time in the context of this doctoral thesis, shall henceforth be called Shifted Position-Diffuse Reflectance Imaging (SP-DRI).

Within the framework of this doctoral thesis, SP-DRI will be investigated as a technique for the purpose specified above. The monitored parameter of interest is the diameter (more precisely: its variation) of the capillaries. The overarching research questions that arise are thus:

- Is the developed and proposed SP-DRI algorithm capable of detecting the location of structures on the scale of human capillaries within turbid media?
- Is it possible to derive information on the diameter of the capillary structures on the basis of SP-DRI, thus providing an indication of vasoconstriction or vasodilation of the capillary bed?

After these questions on the fundamental functionality of the SP-DRI method, investigations on the performance of the approach have to follow. In order to allow detectability of such small structures within turbid media using SP-DRI and to maximize the gain in information, it is essential to achieve a high contrast between the skin and the microcirculatory vessels carrying blood and to ensure that the photons irradiated into the tissue pervade the observed

volume as comprehensively as possible. These two aspects are influenced by physics principles as well as by the specifications of the SP-DRI sensor. The middle row of the diagram given in figure 6 illustrates this.

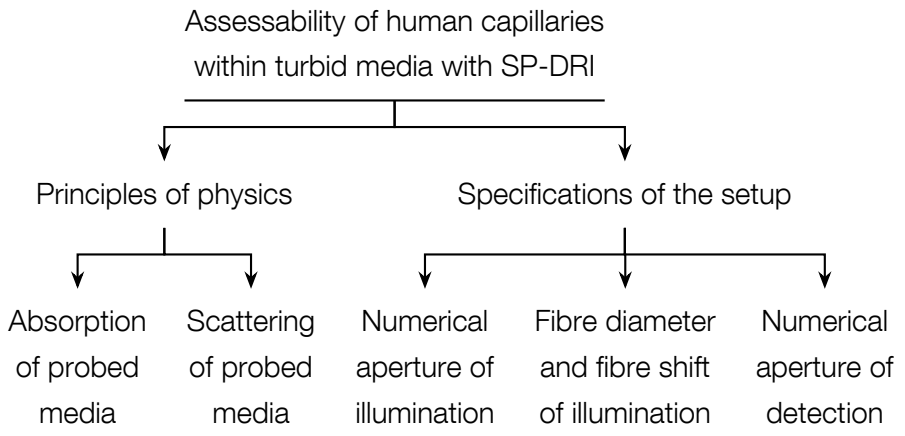

Figure 6: Diagram illustrating the framework of the main research question. The two key mechanisms that enable the detectability of human capillaries within turbid media with SP-DRI are given on the first level. Below that, the factors influencing those mechanisms are listed - they are of relevance for the present doctoral thesis.
Note: As the SP-DRI algorithm is developed from scratch in the context of this thesis, the influencing factors cannot be listed exhaustively. In fact, those determinants are investigated that are expected to be of highest importance based on the state of the art (medium, illumination wavelength) or the operating principle of the algorithm (illumination fibres, detection characteristics). At this early stage of research, factors such as the illumination intensity can readily be compensated for by adjusting the exposure of the detector and are therefore not considered in the context of this fundamental research.

These mechanisms, again, are influenced by specific factors (lower level of the diagram in figure 6). This implies the following sub-questions:

- Which illumination wavelength allows the best conclusions to be drawn in this context? This addresses absorption and scattering.
- Which values must be considered for the illumination parameters (core diameter, numerical aperture A_N and shift of the illumination fibre) to yield an optimal signal?
- What needs to be considered regarding the numerical aperture A_N when detecting the diffuse reflection?

This is connected to the following questions on performance that commonly have to be addressed for medical diagnostic equipment:

- What lateral resolution and imaging depth can be achieved with the SP-DRI algorithm?
- How robust is the prediction of the capillary diameters: Does it also work for varying optical properties of the skin and blood, respectively?

As this is fundamental research, these aspects will initially be addressed using a variety of MC simulations. This approach allows to develop algorithms in a well-defined environment and to investigate the influence of certain parameters separately. In the further course, a transition to optical phantoms will follow; this requires elaborations to be made:

- Which design is needed for an optical phantom to allow the aforementioned conditions to be investigated?
- What material can be embedded to imitate such fine capillary structures?
- What (and what quantities of) absorbers and scatterers must be added to obtain adequate optical properties?

In order to be able to measure the diffuse reflection experimentally, a suitable optical setup is necessary. Again, this leads to research questions that need to be answered, including in particular:

- What is the basic design of an SP-DRI sensor?
- This setup should be cost-effective and robust; which optical components are suitable for this purpose?
- What are the requirements for the data evaluation algorithm and how can it be implemented?

The specified hypotheses are to be addressed in the course of this doctoral thesis. The following chapter provides an insight into the material and methods used for this purpose.

4 Material and Methods

4.1 Shifted Position-Diffuse Reflectance Imaging

For reconstructing the vasculature pattern from the diffuse reflectance data, a novel imaging technique was developed in this doctoral thesis. It was labelled SP-DRI. This algorithm constitutes the key element of the present doctoral thesis and will be applied in MC simulations as well as in laboratory experiments.

The algorithmic procedure of SP-DRI is inspired by SERDS, a technique applied in the context of Raman spectroscopy (compare the explanations in section 2.3). Specifically, this means that the approach of SERDS "(with the exception that in SERDS the two data sets are subtracted, while in SP-DRI a division is performed - the SP-DRI results oscillate around the value 1) is now being transferred to DRI by slightly shifting the excitation position. Thus, the signal variation does not occur in the wavelength range as in SERDS, but as a spatial shift: From a spatial point of view, the background noise remains almost unchanged, while the position of the signal is slightly offset." [P3]

The practical implementation of SP-DRI will be explained step by step in the following. As previously described for DRI in section 2.3, an illumination of the sample as well as a detection of the photons emerging from the sample are also necessary with SP-DRI for the generation of the diffuse reflectance raw data. In doing so, the starting point of SP-DRI are two diffuse reflectance data

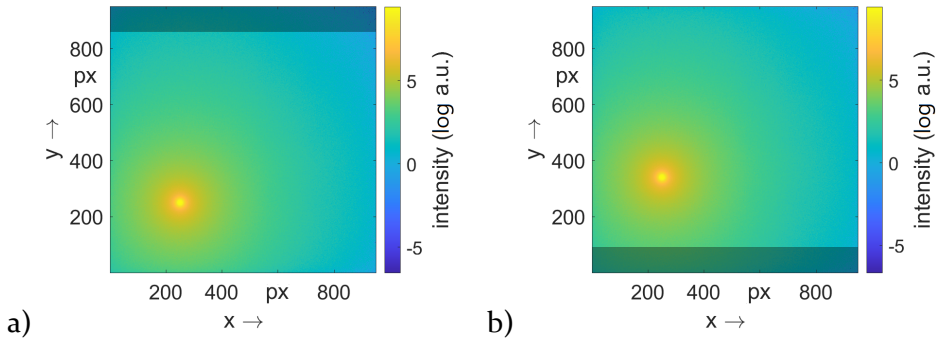

Figure 7: Exemplary illustration of the SP-DRI method. This method is based on two diffuse reflectance raw data sets with slightly shifted position (here: y position) of the illumination in (a) data set 1 compared to (b) data set 2. The areas that are subsequently trimmed (see running text for explanation) are indicated by the dark bars.

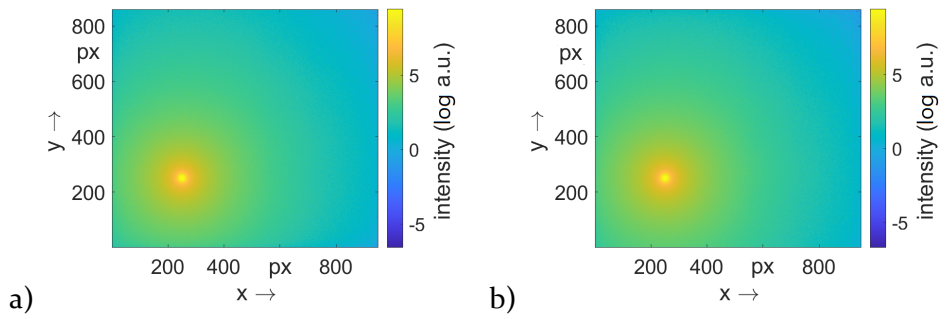

Figure 8: Continuation of the exemplary illustration of the SP-DRI method. After trimming the two matrices that were already introduced in figure 7, the data sets appear as shown here.

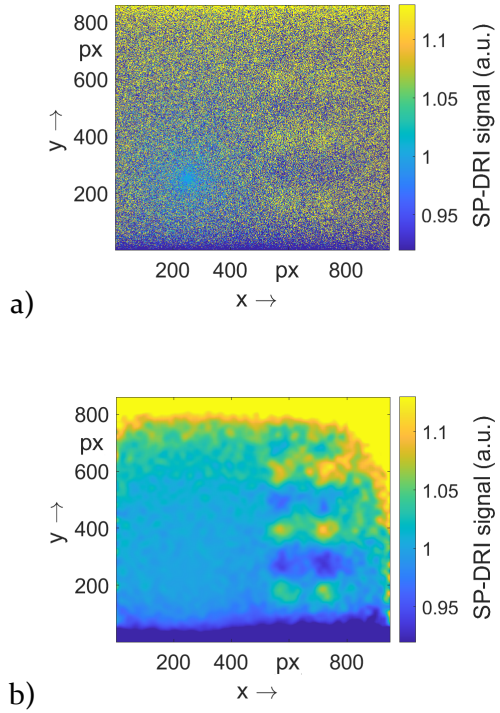

Figure 9: Continuation of the exemplary illustration of the SP-DRI method. (a) One of the trimmed data sets shown in figure 8 is divided pixelwise by the other one. The resulting data set is quite noisy, although some patterns can already be discerned. (b) Finally, a filtering with a 2-D Gaussian smoothing kernel (here: $\sigma = 10$ px) is applied to expose the structure.

sets (matrix 1 and matrix 2) that are configured such that the position of the illumination light source in both matrices is slightly shifted relative to each other in x or y direction at otherwise identical simulation or experimental parameters [P3]. The detection is carried out two-dimensionally and with high resolution on the same side of the sample where also the illumination is implemented. Exemplary matrices 1 and 2 are shown in figure 7.

To enable the elimination of undesired features (especially the influence of the illumination, but also noise) in the final SP-DRI signal, data sets with equal relative positions of the light source have to be generated. For that, the original data sets have to be trimmed by the size of the particular illumination shift. With this, "now the relative positions of the light source in both matrices are equal with respect to their x and y coordinates. This leads to a relative shift of the capillary structures to each other." [P3] For the exemplary matrices already introduced, the scenario presented in figure 8 results (the areas to be trimmed are highlighted in figure 7).

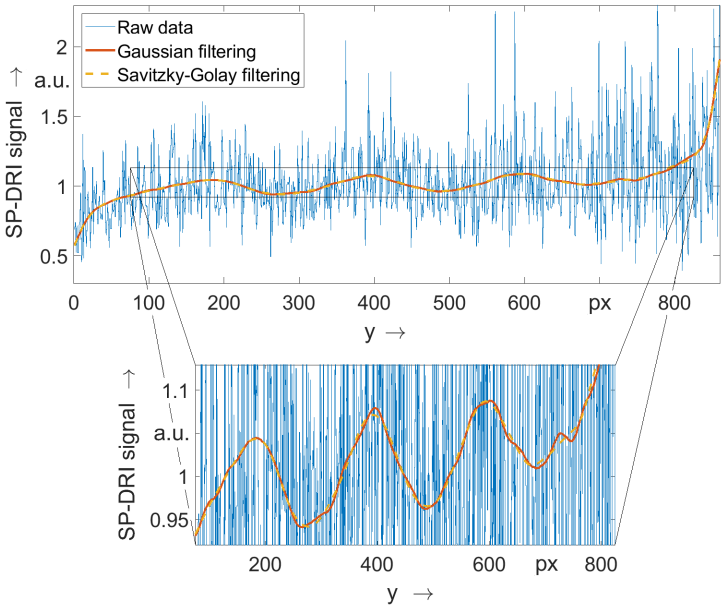

Figure 10: Cross-sections along the y axis at $x = 570$ px through the data shown in figure 9 to further illustrate the SP-DRI method. The Savitzky-Golay filtered curve is referred to as the SP-DRI signal (orange dashed line). To visualise the effect of that filtering, the cross-sections through the unfiltered SP-DRI signal (i.e. through the matrix given in figure 9a) and the SP-DRI signal after the Gaussian filtering (i.e. through the matrix given in figure 9b) are displayed here as well. They have, however, no relevance for the SP-DRI algorithm.

To reveal the capillary structure and to generate the final SP-DRI data set, "one intensity matrix is divided pixelwise by the other one." [P3] This is followed by a post-processing with appropriate filters. Both is illustrated in figure 9.

In order to obtain what will henceforth be referred to as the SP-DRI signal curve, a cross-sectional plane through the filtered SP-DRI matrix in the region of the capillaries has to be taken and subsequently a Savitzky-Golay filter is applied to that curve; figure 10 illustrates these steps. The interpretation of this curve is as follows: A capillary loop is always located between a local maximum and the subsequent local minimum of this curve. Thus, the exemplary SP-DRI curve indicates the presence of three capillary loops. Section 5.1 provides a detailed discussion of why this interpretation applies.

"The SP-DRI algorithm is extremely fast and takes only a few milliseconds to compute an image. [...] Mathematically, this approach is equivalent to a computational edge filter, which is, due to the induced relative offset of the capillary structures to each other, sensitive to intensity changes generated by this capillary structure." [P3]

To show the potential of the SP-DRI signal in comparison to an analysis of the pure raw data signal, the previously mentioned cross-section was - for illustrative purposes only - also applied to the raw data signal. This can be found in figure 11. Also this matter is covered by the discussion in section 5.1.

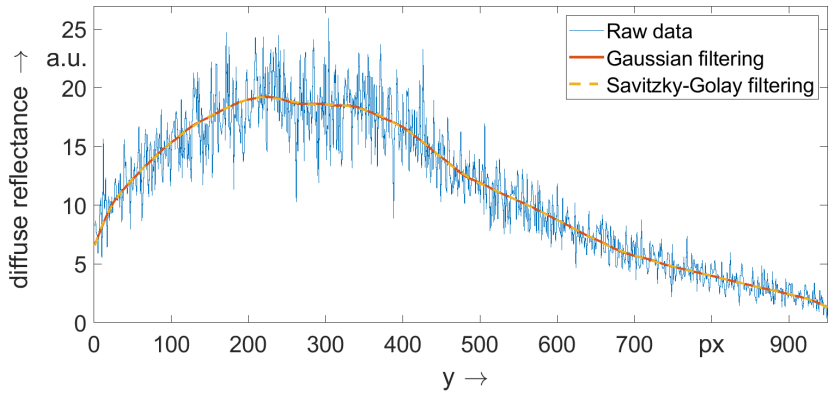

Figure 11: Cross sections along the y axis at $x = 570$ px through the first of the two raw data sets forming the basis of the SP-DRI method (figure 7a) and the respective filtering already introduced in the context of the SP-DRI signal. The filtering of the raw data was done for comparison purposes only, it is actually not applied in the context of SP-DRI (with SP-DRI, the filters are applied at the end of the process, i.e. after the division, as explained above). Note: In comparison to figure 7, the data shown here is not on a logarithmic scale.

4.2 Monte Carlo simulations

4.2.1 Basic setup

To address the different research questions (compare chapter 3), some of the MC simulation parameters had to be adjusted in each study in order to meet the specific requirements. Other settings, however, remained unchanged to ensure comparability of the results across the various simulation runs. Below, a general overview of the simulation parameters is given, while any of their variations will be described in the specified sections that follow.

All MC simulations were performed using MCXLAB (version V2020) [85] on computers with MATLAB R2019a. Various graphics cards were available for computation: Two Nvidia Titan RTX (24GB of memory each), two Nvidia GeForce RTX 3090 (24GB of memory each) and two Nvidia Tesla P100 (16GB of memory each) [P1–P3].

4.2.1.1 Simulation volume, tissue model and vasculature

The simulation volumes used in the studies were $950 \times 950 \times 2000$ voxels in size. The length of one voxel was set to be 1 µm.

To create a realistic tissue model, seven tissue layers were considered in the MC simulations. The stratum corneum was assumed to be the outermost skin layer, followed by an epidermal layer. The subsequent dermis consisted of four layers and was flanked by subcutaneous tissue. Moreover, it was taken into account that haemoglobin is not evenly distributed in the tissue or in tissue layers, but concentrated in blood vessels, more precisely in capillary loops and the SVP. Haemoglobin could thus only be found in some of the tissue layers to be anatomically precise [P3].

The dimensions were anatomically correct and can be found in the illustrations given as overview in figure 12. The diameter (cylinders) of the SVP was 30 µm and the default diameter of the capillary loops was 10 µm. To address some specific research questions, the latter could be varied [P3]. Compare section 2.4 for an outline of the conditions in humans.

4.2.1.2 Illumination

The illumination was implemented at the $z = 0$ boundary of the simulation volume as uniform cone beam in $+z$ direction. This beam had a defined diameter and half-angle, constituting the illumination with an optical fibre with a specific core diameter $\emptyset_{\text{Core}}$ and numerical aperture A_N [P3]. It is part of this doctoral thesis to determine the optimal values for these parameters

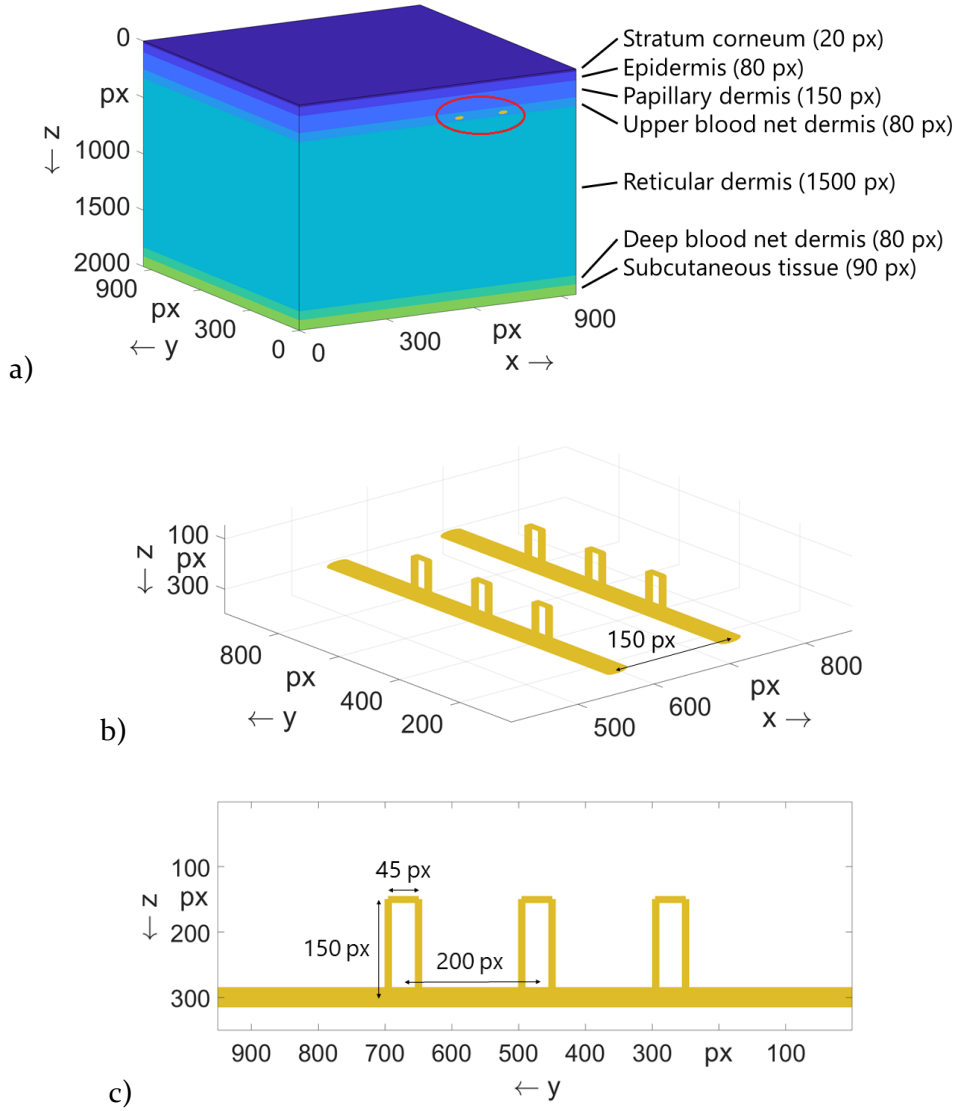

Figure 12: a) Basic MC simulation volume (950×950×2000 voxels; 1 px≙1 µm) with the seven skin layers and the vasculature (SVP) side-gated in the x-z plane (red oval). The illumination and the detection of the photon packets are realized at z=0. The layer of subcutaneous tissue is trimmed at $z = 2000\ px$; its actual thickness would be 6000 px. b) Vasculature placed within the simulation volume, consisting of the capillary loops and the SVP. c) Detailed illustration of one of the vasculature branches with its dimensions. The dimensioning starts at the centres of the structures. Figure description adopted from my previously published articles [P1–P3].

(see section 5.4). The illumination wavelength was adjusted by appropriately setting the optical properties of the elements.

"The four key parameters for characterizing and modelling the optical properties of tissue are the absorption coefficient μ_a, the scattering coefficient μ_s, the anisotropy factor g and the refractive index n. In order to create a realistic skin model, the single skin layers were also differentiated with regard to these optical parameters; the same applied to oxyhemoglobin. In doing so, reference was made to numerical values and findings from corresponding literature sources. Table 3 contains the details and names the literature sources." [P3]

The simulations in this doctoral thesis are mainly based on the wavelength $\lambda = 424$ nm; in one setup, also $\lambda = 540$ nm is used for comparison purposes (see also section 4.2.2.7). In doing so, the respective wavelengths are chosen to meet the region of the two strongest local maxima of the absorption curve of blood in the visible wavelength range (as the curves of oxy- and deoxyhaemoglobin are quite similar in these regions, it was not differentiated between both in this case; compare figure 4) [109]. The selected illumination wavelengths should thus best allow to detect extremely small blood vessels: The highest possible contrast may be achieved between the microvasculature filled with blood and the surrounding tissue [P3].

Table 3: Optical properties of the skin layers and the microvasculature considered in the MC simulations [P3, 68, 108–111].

Element	424 nm		540 nm			
	μ_a $[\frac{1}{\text{mm}}]$	μ_s $[\frac{1}{\text{mm}}]$	μ_a $[\frac{1}{\text{mm}}]$	μ_s $[\frac{1}{\text{mm}}]$	g [-]	n [-]
Stratum corneum	1.46	50.00	1.00	50.00	0.90	1.53
Epidermis	3.19	13.96	1.81	7.84	0.85	1.34
Papillary dermis	0.80	13.36	0.45	11.09	0.80	1.40
Upper blood net dermis	1.14	13.36	0.65	11.09	0.90	1.39
Reticular dermis	0.68	13.36	0.39	11.09	0.76	1.40
Deep blood net dermis	1.37	13.36	0.78	11.09	0.95	1.39
Subcutaneous tissue	0.64	7.00	0.36	7.00	0.80	1.44
Microvasculature	203.17	8.00	28.75	8.00	0.96	1.36

4.2.1.3 Detection

The incident photon packets were also detected at the $z = 0$ boundary. Per detected packet, its direction and coordinate of incidence at that boundary as well as the cumulative path lengths in each medium of its trajectory were stored. With the exception of the surface at $z = 0$, all boundaries of the simulated volume were absorbent in order to avoid undesired back reflection and to best represent realistic conditions [69]. The $z = 0$ boundary, in contrast, took into account Fresnel reflection [P3].

As described above, the raw data of the simulation provides information on how many photon packets were registered at each position of the $z = 0$ boundary, along with a couple of other parameters. Of interest, however, is the diffuse reflectance in terms of an intensity distribution on the $z = 0$ boundary. This information needs to be obtained during post-processing: As the photon packets are attenuated along their trajectories, their weight when returning to the $z = 0$ boundary is calculated using Beer's law [P3]. With the initial weight of each photon packet being 1, the following equation results for the intensity I of a photon packet hitting the detector:

$$I = \prod_{i=1}^{m} \exp(-\mu_{a,i} \cdot z_i), \tag{1}$$

where m is the number of media (skin layers and haemoglobin), z_i the cumulative path length of the photon packet in each medium and $\mu_{a,i}$ the absorption coefficient of the respective medium.

The fact that diffuse reflectance is mostly captured using an objective or a fibre bundle accepting light only up to a certain angle of incidence was also taken into account in post-processing. As mentioned earlier, the direction under which each detected photon packet is hitting the $z = 0$ boundary (i.e. the detector plane) is stored (referred to as $\vec{v}$ in the following). Thus, different detector properties in terms of photon acceptance can be considered by evaluating

$$\arccos\left(\frac{\vec{v} \circ \vec{w}}{|\vec{v}| \cdot |\vec{w}|}\right) \leq \arcsin(A_N) \tag{2}$$

for each photon packet and excluding those packets that do not satisfy this condition; $\vec{w} = \begin{pmatrix} 0 \\ 0 \\ -1 \end{pmatrix}$. It is part of this doctoral thesis to find the optimal

value for the numerical aperture A_N of the setup used for detection (see section 5.3).

To increase the simulation speed, a photon packet was terminated when its weight was less than 1% of its initial weight. To maintain the conservation of energy, the Russian roulette approach was used (see section 2.5 for explanation). For each simulation run, 10^{10} photon packets were launched [P3].

4.2.2 Specific simulation parameters

4.2.2.1 Influence of the A_N of the detection

To investigate the influence of the numerical aperture A_N of the detection fibres (or the objective used for detection) on the detectability of the capillary loops by means of SP-DRI, different values had to be set for this respective parameter. To cover this research question comprehensively, values ranging from 0.05 to 1 were chosen for A_N at increments of 0.05 - thus, the parameter space was not needed to be constrained (which is also the reason why this research question is dealt with first). The corresponding results are presented in section 5.3.

4.2.2.2 Influence of the illumination parameters

The three key parameters that were investigated in the context of the illumination are the numerical aperture A_N and the core diameter $\emptyset_{\text{Core}}$ of the illumination fibre as well as its lateral shift inherent to the SP-DRI process (see section 4.1). Table 4 gives an overview of the values chosen for the above parameters.

Table 4: Overview of the specific numerical values used to address the influence of the key illumination parameters on the SP-DRI signal. Note: 1 px corresponds to 1 µm.

Parameter	Unit	Value
$\emptyset_{\text{Core}}$ of illumination fibre	[µm]	20, 35, 50
A_N illumination fibre	[-]	0.25, 0.35, 0.45, 0.55
Shift of illumination fibre (x|y)	[px]	(250|250) → (250|300), (250|250) → (250|320), (250|250) → (250|340), (250|250) → (250|360), (250|250) → (250|380)

The narrowing of the parameter space may be justified as follows: Preliminary investigations showed that illumination shifts around 100 µm lead to elevated SP-DRI modulations for anatomically correctly sized capillary diameters. In a later physical SP-DRI sensor, this shift can be achieved effectively by placing two optical fibres next to each other and illuminating them serially. Thus, the limitations of both other parameters are construction-related: The cladding diameter of the optical fibres used cannot exceed the illumination shift value as otherwise two neighbouring fibres would overlap, which is technically not possible.

To only simulate fibre sizes that can later on also be realised constructionally - enabling a future constructional implementation of SP-DRI is of major importance for the SP-DRI project -, research was carried out on the market: The relevant suppliers of optical components offer fibres with core diameters of up to 50 µm in this range, and the numerical apertures are correspondingly small. Within the resulting parameter spaces, discrete values were chosen for the simulations.

The analysis was performed for all possible combinations of the discrete values defined for the three parameters. Thus, 72 ($= 3 \cdot 4 \cdot 6$) simulation runs had to be carried out. The corresponding results are presented in section 5.4.

4.2.2.3 Specificity of SP-DRI

To examine the specificity of SP-DRI, the vasculature pattern within the MC simulation volume was altered and it was evaluated whether this variation is reflected in the SP-DRI signal. For this purpose, two different setups were established that differ from the default configuration (compare figure 12) as follows:

- Setup 1: The vasculature branch at $x = 700\ px$ was removed so that only one branch consisting of the SVP and three capillary loops was present.
- Setup 2: For both vasculature branches, the capillary loop at $y = 650\ px$ was removed so that each of the two branches was composed of only one SVP with two capillary loops.

The results are presented in section 5.5.

4.2.2.4 Ability for two-point discrimination

The vasculature pattern was also modified for the investigation of the ability for two-point discrimination (in terms of sensitivity) of the SP-DRI method. The question to be addressed is whether capillary loops present in the simulation volume will be reflected as such in the SP-DRI signal. Therefore, the lateral positions of the two vasculature branches (each consisting of one

SVP with three capillary loops) were randomly determined by the simulation script within the following constraints (compare the anatomical dimensions outlined in section 2.4; all dimensions refer to the centres of the respective cylinders):

- Both SVP are aligned along the y axis. $350\ px \leq x \leq 450\ px$ applies to the x coordinate of the first SVP. The second SVP has a distance Δx of $150\ px \leq \Delta x \leq 400\ px$ to the first one.
- The capillary loops are each located on their respective SVP (this determines their x coordinates). $200\ px \leq y \leq 300\ px$ applies to the y coordinate of the onset of the first capillary loop of such a vasculature branch. The onset of the second capillary loop of each branch has a distance Δy of $105\ px \leq \Delta y \leq 180\ px$ to the offset of the respective first one (intercapillary distance), likewise the third one to the second one.

The depth of the structures remained unchanged from the default setup. The related results can be found in section 5.6.

4.2.2.5 Imaging depth and lateral resolution of SP-DRI

"To determine the imaging depth of SP-DRI, the incorporated microvasculature is incrementally placed deeper into the skin starting from the default configuration." [P4] Starting at $z = 150\ px$ (compare figure 12), the upper margin of the vasculature is lowered to $z = 230\ px$. In doing so, it is examined on each occasion whether the capillary loops can still be identified by means of SP-DRI. This maximum value was obtained from preliminary trials; no signal was detectable deeper within the volume.

"In an analogous manner, the intercapillary distance Δy (distance between the lateral offset of one and the onset of the next capillary loop) in y direction is reduced stepwise to determine the lateral resolution." [P4] This parameter is gradually decreased from $\Delta y = 155\ px$ to $\Delta y = 65\ px$ and it is assessed whether the single capillary loops of a vasculature branch can still be distinguished by SP-DRI. Again, this minimal value was obtained from preliminary trials; for smaller values, no differentiation was possible at all.

The corresponding results are presented in section 5.7.

4.2.2.6 Determination of the capillary diameter

To investigate if it is generally possible to detect differences in the diameter of the capillary loops on the basis of SP-DRI measurements, different values had to be chosen for this parameter. As already introduced, the diameter of human capillaries can be taken as $\emptyset_{cap} = 10\ \mu m$ in the physiological state (compare section 2.4). Accordingly, "diameters ranging from $\emptyset_{cap} = 4\ \mu m$ to

$\emptyset_{cap} = 14\,\mu m$ (in increments of 2 µm) were regarded as reasonable deviations from the norm [43, 112] and simulated accordingly." [P1] "Per simulation run, the diameter was kept the same, so the diameters were changed across the individual simulation runs." [P2] The corresponding results are presented in section 5.8.

4.2.2.7 Influence of the illumination wavelength

As already introduced before, the illumination wavelengths used in this doctoral thesis are in line with the two strongest local maxima of the absorption curve of blood in the visible wavelength range (compare to figure 4). All simulations except those introduced in this section are based on $\lambda = 424\,nm$, which is in the range of the global maximum of the absorption curve. To evaluate the assumption that this setup is providing the highest contrast, a comparison with simulations at $\lambda = 540\,nm$ is made as this wavelength is in the range of the second highest value of the absorption curve.

Again, six capillary diameters were assessed as described in the previous section. Therefore, the results of this section can be compared to those of the previous one to determine the influence of the illumination wavelength. This analysis can be found in section 5.9.

4.2.2.8 Prediction of the regression parameters

Around the central wavelength of $\lambda = 424\,nm$, "the optical properties were randomly varied following a Gaussian distribution. The standard deviation of μ_a and μ_s was set to $\sigma = 30\%$ of the values at $\lambda = 424\,nm$ while it was set to $\sigma = 3\%$ for g and n (Matlab command: `normrnd`). Thus, the simulated optical properties fluctuate over a relatively wide spectral range to reflect the range of possible optical properties values reported in the literature for different skin types and by different research groups [68].

The random Gaussian distribution was applied to each element of the optical properties separately to obtain the final set of optical properties for the simulation (i.e. each element had its unique deviation instead of one deviation per data set). In a post-processing step, μ_s and g were combined as μ_s' to reduce the complexity of the system." [P2]

4.3 Quantification of the SP-DRI signal

To make reliable statements on changes in the SP-DRI signal, it is necessary to quantify its modulation. Looking at the exemplary signal curve given in figure 10 and knowing that "the capillary structure is located (...) between a local maximum and the subsequent local minimum of the SP-DRI signal" [P1],

there are in particular two parameters useful for describing this signal: One is the amplitude of the modulation and the other is its period. In the following, two possible modulation parameters derived from this will be presented.

4.3.1 Modulation parameter A_{norm}

The modulation parameter A_{norm} is based on the simpler of the two principles presented in this section, it solely targets the peak-to-peak amplitude of the modulation. Thus, it is based on the values of an SP-DRI signal function at a local maximum and the subsequent local minimum.

Since the SP-DRI signal curve does not oscillate around a defined reference, it is necessary to normalize the peak-to-peak amplitude at its mean to allow for comparison of different signals. Following these considerations, the definition of A_{norm} is given by

$$A_{\mathrm{norm}} = \frac{f_{\text{SP-DRI}}(a) - f_{\text{SP-DRI}}(b)}{\frac{f_{\text{SP-DRI}}(a)+f_{\text{SP-DRI}}(b)}{2}} = 2 \cdot \frac{f_{\text{SP-DRI}}(a) - f_{\text{SP-DRI}}(b)}{f_{\text{SP-DRI}}(a) + f_{\text{SP-DRI}}(b)} \qquad (3)$$

with a being the position of a local maximum and b that of the subsequent local minimum of the SP-DRI signal curve. $f_{\text{SP-DRI}}(a)$ and $f_{\text{SP-DRI}}(b)$ are the values of the SP-DRI signal curve at positions a and b, respectively; compare also figure 13 [P1].

4.3.2 Modulation parameter K and K_{norm}

In the case of less idealized waveforms, the assumptions made in the context of A_{norm} may fall short - leading to a situation where the modulation parameter actually covers too little of the information present in the modulation. Therefore, another modulation parameter, K, needs to be established. The idea is the following: Between a local maximum and its subsequent local minimum, the SP-DRI signal curve encloses a specific area which depends on the individual shape of that curve [P1].

From this, the parameter K results in

$$K = f_{\text{SP-DRI}}(a) \cdot (b - a) - m \cdot \sum_{i=a}^{b} f_{\text{SP-DRI}}(i) \qquad (4)$$

with the variables being defined as in equation 3 above [P1] and m being the step width. There are i steps of width m between the positions a and b. An illustration of this definition of K can be found in figure 13 with further explanation in the caption.

Also in the case of K, an appropriate normalization is necessary to ensure the comparability of different signal curves. In addition to the already discussed adjustment to the mean of the peak-to-peak amplitude (third member in equation 5), a further factor must be taken into account here: "The distance between the respective local maximum and local minimum (distance between a and b) [second member in equation 5]. Finally, this value is multiplied by 100 [fourth member in equation 5] for better readability. This normalisation ensures that the K values of all curves can be compared with each other in a meaningful way." [P1] This results in a modulation parameter K_{norm} of the form

$$K_{\text{norm}} = K \cdot \frac{1}{(b-a)} \cdot \frac{2}{f_{\text{SP-DRI}}(a) + f_{\text{SP-DRI}}(b)} \cdot 100. \tag{5}$$

4.3.3 Determination of local extrema

With the help of the Matlab command `islocalmax`, the local maxima were found; the distance between two maxima as well as the number of maxima to be found had to be defined in advance. "The same applies to the minima, for which the command `islocalmin` was used. Due to this automated classification there is no subjective influence when determining the extrema." [P1]

In the case that the y position of maximum n was larger than that of minimum n, `NaN` (not a number) was set for A_{norm} or K_{norm}, respectively [P1].

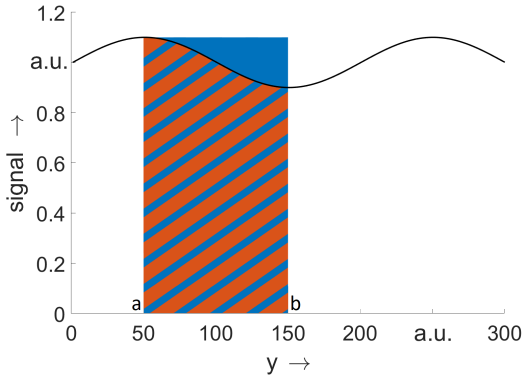

Figure 13: Schematic illustration of the calculation of the modulation parameter K using a sine curve as an example. To calculate the parameter, the red area is subtracted from the blue area. Along the abscissa, both areas extend from a local maximum to the subsequent local minimum. The partial overlapping of both areas is indicated by the hatching. [P1]

4.4 Quantification of changes in the capillary diameter

In the previous section, parameters were introduced that allow the quantification of the SP-DRI signal. In accordance with the hypotheses given in chapter 3, it is part of this doctoral thesis to investigate whether and how these parameters are influenced by changes in the capillary diameters. This possible relationship needs to be quantified, and the present section provides the methodological framework for doing so.

In the best case, the relationship between the capillary diameter $\emptyset_{cap}$ (explanatory/independent variable) and both SP-DRI parameters (A_{norm} and K_{norm}; response/dependent variable) is of linear nature. A linear regression can then be fitted to the data to describe the connection. A data set consisting of multiple data points can thus be reduced to only two regression parameters: intercept (β_0) and slope (β_1) of the regression line. This yields a linear regression model of the form

$$Y = \beta_0 + \beta_1 \cdot \emptyset_{cap}, \tag{6}$$

where Y is a surrogate for one of the modulation parameters A_{norm} or K_{norm} [P1]. Regarding a visualization of this step, reference is made to the results presented in section 5.8 (in particular figure 30).

The goodness of fit of such models is commonly expressed by the coefficient of determination R^2. "The R^2 is usually presented as the quantity that estimates the percentage of variance of the response variable explained by its (linear) relationship with the explanatory variables." [113] While $R^2 = 0$ refers to an unsuitable model, $R^2 = 1$ indicates a perfect model fit.

A downside of R^2 is that it increases with more independent variables being included into the model; to obey the principle of parsimony, the adjusted coefficient of determination $\bar{R}^2$ compensates for this by adding a term to R^2 that takes into account both the number of observations and independent variables. In general, $\bar{R}^2 < R^2$ applies; theoretically, $\bar{R}^2$ can also take on negative values [114].

4.5 Influence of the optical properties on the regression parameters

Assuming a linear relationship as described in the previous section, a quantitative assessment of the capillary diameter can be made after determining A_{norm} and K_{norm}, respectively, if the regression parameters β_0 and β_1 are known (see equation 6). Unfortunately, the latter is only the case in the simulative domain, but not in real-life measurements. Consequently, it is

crucial to develop a procedure that allows the prediction of the capillary diameter without knowledge of the regression parameters β_0 and β_1 [P2]. This is the purpose of the present section (in the following, exemplified for the parameter K_{norm}).

Except for a few modifications, the following part of this section is a reprint of my previously published article and taken from [P2].

According to the relationship [P1]

$$\emptyset_{\mathrm{cap}} = \frac{K_{\mathrm{norm}} - \beta_0}{\beta_1}, \tag{7}$$

reliable information on the capillary diameter of a person (across different individuals) can only be obtained if it is possible to either determine β_0 and β_1 (for a particular person) or to keep both parameters constant (equation 7 is obtained by rewriting equation 6). For this reason, it is necessary to study the relationship between the optical properties of the human skin and these two regression parameters in more detail to possibly allow for their prediction. For this purpose, the optical properties are randomly varied as described in section 4.2.2.8 and their influence on β_0 and β_1 is investigated. The latter is done by a random forest (RF) approach.

RF is an ensemble learning technique which can be used for regression. During training, a multitude of decision trees is generated which allows to specify the importance of variables in a regression and to predict the regression response based on a given input. In this thesis, these calculations were performed on a computer with MATLAB R2021b. The two parameters β_0 and β_1 were analysed separately from each other as responses of the RF. The procedure is illustrated as flowchart in figure 14 and described in detail in the following.

Initially, to determine the importance of the prediction parameters, all 24 optical properties values (μ_a, μ_s' and n for each of the seven skin layers and for haemoglobin) were included as predictors into a RF regression ensemble model with β_0 or β_1, respectively, as response. This was done in Matlab via `fitrensemble`. The ensemble aggregation method for this investigation was set to *Bag* and it was defined that all predictors should be included into the decision trees. This procedure allowed a valid estimation of the importance of each predictor (out-of-bag permuted predictor importance).

In case the outcome of the preceding step is not sufficient, the importance of the predictors could furthermore be examined with a neighbourhood

component analysis for regression. Also this algorithm is typically used to select features as part of data preprocessing. The predictor and response variables were identical to those used in the previous step. This was done in Matlab via `fsrnca`.

Based on the previous findings, only the most important predictor(s) was/were included in the further RF regression ensemble model. To find hyperparameters that minimize the five-fold cross-validation loss, the automated optimization of the RF hyperparameters was enabled within `fitrensemble`. Thus, the algorithm sought the optimal values for the ensemble aggregation method (*Bag* or *LSBoost*), the number of ensemble learning cycles, the learning rate for shrinkage and the number of observations per leaf. The hyperparameters found in this way were later on used during training of the individual RF models (to guarantee a stable prediction, the number of ensemble learning cycles was set to 500, which is significantly higher than the suggested optimal value).

In a next step, the influence of the most important predictor(s) was further investigated. The aim was to assess whether it is possible to find an analytical expression for their influence on the respective response; this would help to better understand any functional interrelationship and to find reasons for its presence. Furthermore, an analytical function like this can help to overcome or at least reduce a possible overfitting inherent in the RF approach.

For this purpose, within the boundaries of the value range of each predictor (more precisely: in the interval between 20% and 80% of this range, to exclude outliers from the analysis) 200 equidistant values were generated and the RF response was queried. Afterwards, an analytical expression was fitted

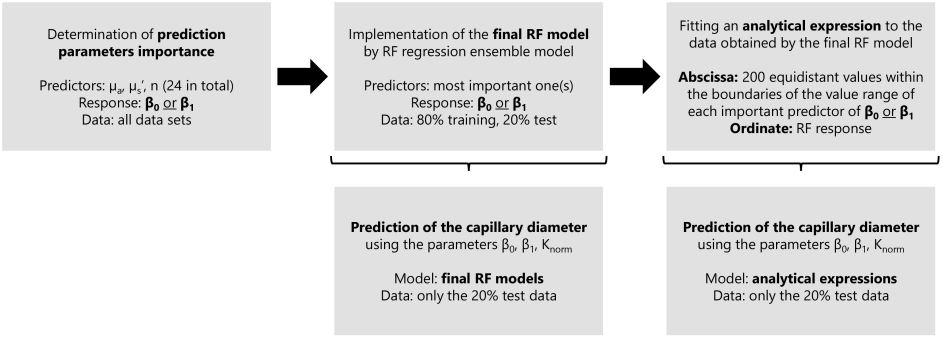

Figure 14: Flowchart of the RF approach and the further analysis. Details on all the steps can be found in the running text. [P2]

to the data; it didn't stem from theory, but was intended to describe the effect as accurately as possible.

Lastly, the possibility of predicting the capillary diameter according to equation (7) using the parameters K_{norm}, β_0 and β_1 was investigated, whereby the two latter parameters should be predicted based on the methods introduced in the previous steps (RF and analytical expression). This analysis is performed on the basis of 20% of the data only (test data) while using the rest of the data for training the RF model. Thus, for each set of test data, six capillary diameters can be estimated based on the six K_{norm} values (one per capillary diameter) and the prediction of β_0 and β_1 based on the optical properties. Again, this analysis is performed 30 times with the data being randomly assigned to the training and test set, the results were averaged afterwards.

To be able to compare the performance against non-predicted values, β_0 and β_1 were calculated for an ideal simulation (i.e. without varying the optical properties so that they corresponded to $\lambda = 424$ nm) and assumed as fixed values for calculating the diameters.

The performance of this approach was evaluated by the coefficient of variation (CV), a standardized measure of dispersion of, amongst others, frequency distributions. It is defined as the proportion of standard deviation and mean value and is useful when comparing data sets with different units or means.

4.6 Experimental approach

The aim of the experimental domain is to validate the results obtained from the MC simulations. In the present doctoral thesis, this was realized at two levels of complexity: an initial proof-of-concept approach and a more dedicated setup based on this. This two-step workflow is described in section 4.6.1 for the optics development and in section 4.6.2 for the optical phantoms used.

4.6.1 Optics development

4.6.1.1 Proof-of-concept setup

As mentioned above, the following laboratory experiment has to be regarded as a proof-of-concept approach. The setup comprises two key modules: an illumination unit and a detection unit. The general layout can be seen in the sketch and photograph presented in figure 15a and b, respectively [P3].

The illumination "was realized by means of a glass fiber ($\emptyset_{\text{Core}} = 50\,\mu\text{m}$) with the light of a mercury-vapor lamp coupled into it. To prevent the image information from being blurred, the spectral range of the light source was narrowed by means of a long pass ($\lambda_{\text{Cut-On}} = 500\,\text{nm}$) and a short pass filter ($\lambda_{\text{Cut-Off}} = 650\,\text{nm}$) so that the illumination spectrum was finally dominated by the strong intensity peak of the mercury-vapor lamp at $\lambda \approx 540\,\text{nm}$ and the weaker peak close by at $\lambda \approx 570\,\text{nm}$.

The glass fiber could be moved parallel to the phantom surface with micrometre precision by means of a motorized translational stage. Perpendicular to the phantom surface, the glass fiber was positioned in such a way that its tip was" [P3] in contact with the phantom as this minimizes specular reflection.

The detection of the diffuse reflection was implemented as "a microscope setup consisting of an infinity corrected objective (Mitutoyo, Plan Apo, $f = 40\,\text{mm}$, $A_{\text{N}} = 0.14$) and a plano-convex lens ($f = 150\,\text{mm}$). With this, the phantom surface (...) was imaged onto a monochrome CMOS camera (Flir, BFS-U3-122S6M-C) with a magnification factor of $M = 3.75$.

For data generation, images were taken with the exposure time of the camera set to 300 ms and the color depth set to 12 bit. All ambient light sources were turned off." [P3] According to the principle of SP-DRI (compare section 4.1), two images with laterally shifted illumination are required: "With the

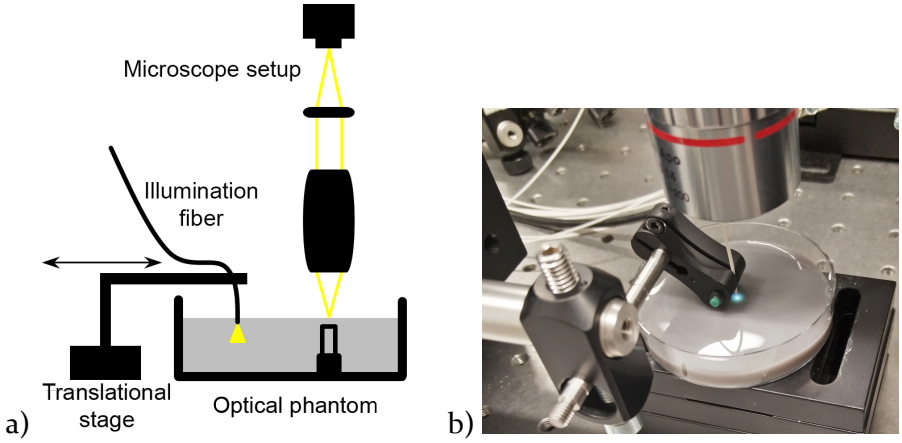

Figure 15: a) Schematic of the experimental setup consisting of an optical phantom with a cantilever incorporated to imitate a capillary loop, a traversable illumination by means of a glass fibre and a microscope setup to image the diffuse reflection from the phantom surface on a camera chip. By way of illustration, the cantilever is turned by 90 degree in the sketch. b) Photograph of the setup. [P3]

motorized translational stage, during data generation the lateral position of the illumination fiber relative to the surface of the optical phantom could be changed to collect all images necessary for the reconstruction of the vasculature structure." [P3] In doing so, the fibre was shifted by $\Delta x = 55$ µm towards the structure embedded in the phantom. Within this phantom study, the data obtained by the SP-DRI procedure was post-processed by a 2-D Gaussian filtering ($\sigma = 5\ px$) [P3].

4.6.1.2 Dedicated SP-DRI sensor

Except for a few modifications, this section is a reprint of my previously published article and taken from [P5].

According to the SP-DRI principle, the sensor consists of an illumination unit and a detection unit. Both are integrated into an additively manufactured housing. A general view of the system can be found in figure 16a.

The detection unit takes up the most space in the overall system. It is a traditional microscope configuration consisting of an infinity-corrected objective (5x, Mitutoyo, Japan) and a tube lens (f=150 mm) for imaging on a monochrome camera chip (Blackfly S BFS-U3-122S6M-C, FLIR Systems, USA) recording at a colour depth of 16 bit. With the components mentioned, the magnification of the system is 3.75. The detection unit is installed in the interior of the sensor housing, the components are illustrated in figure 16b.

Regarding the illumination unit, a key aspect of SP-DRI is the required illumination shift. Constructionally, this can be implemented using optical fibres. In the case of the present study, fibres with a core diameter of 50 µm were used (FG050UGA, Thorlabs, Germany). In total, eight fibres were needed; at their distal ends, they were shortened to an appropriate length, stripped at their ends and then cleaved. They were then assembled into two blocks of four fibres each in order to subsequently bring them as close as possible to the detection image area of the sensor (see figure 17d).

In each block, the glass fibres were arranged in a line in a fixed spacing of 160 µm next to each other. For this purpose, the characteristic layer lines of FDM prints were used and an auxiliary construction was additively manufactured. The layer thickness was set to 160 µm accordingly [S1]. Four fibres were glued into four adjacent grooves of such a block using two-component epoxy adhesive; a photograph of this can be found in figure 17c. Both blocks were then polished from the front side to achieve an optimal coupling into the medium under investigation later on.

Light from light-emitting diodes (LEDs) with a wavelength of 430 nm was coupled into the proximal tips of the glass fibres. Each fibre is connected to an individual LED so that it can be controlled by which fibre the object under investigation is irradiated at a certain point in time. Per LED, the coupling was effected using a ball lens made from BK7 with a diameter of 6 mm, and the alignment was such that the LED body was in direct contact with the ball lens and the latter in direct contact with the fibre. The three elements were placed on axis. A suitable socket to enable this layout was manufactured in-house. This is depicted in figure 17b. Only three of the four available fibres per fibre block were connected to LEDs, the remaining fibre was left as backup.

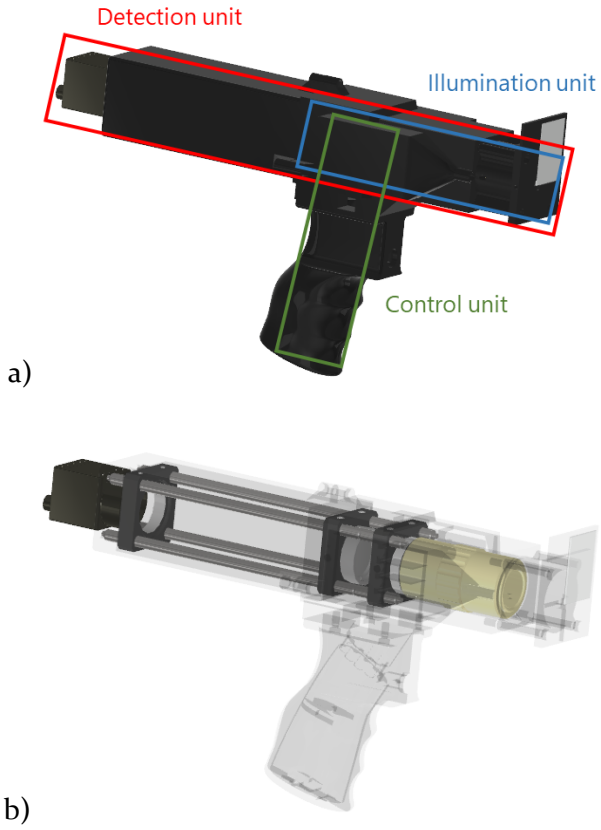

Figure 16: (a) CAD illustration of the overall system consisting of an illumination unit and a detection unit and the control of the LEDs via the Arduino Nano. The pistol grip allows for an ergonomic handling of the sensor during measurements. (b) By rendering the housing transparent, the optical components of the detection unit become visible. [P5]

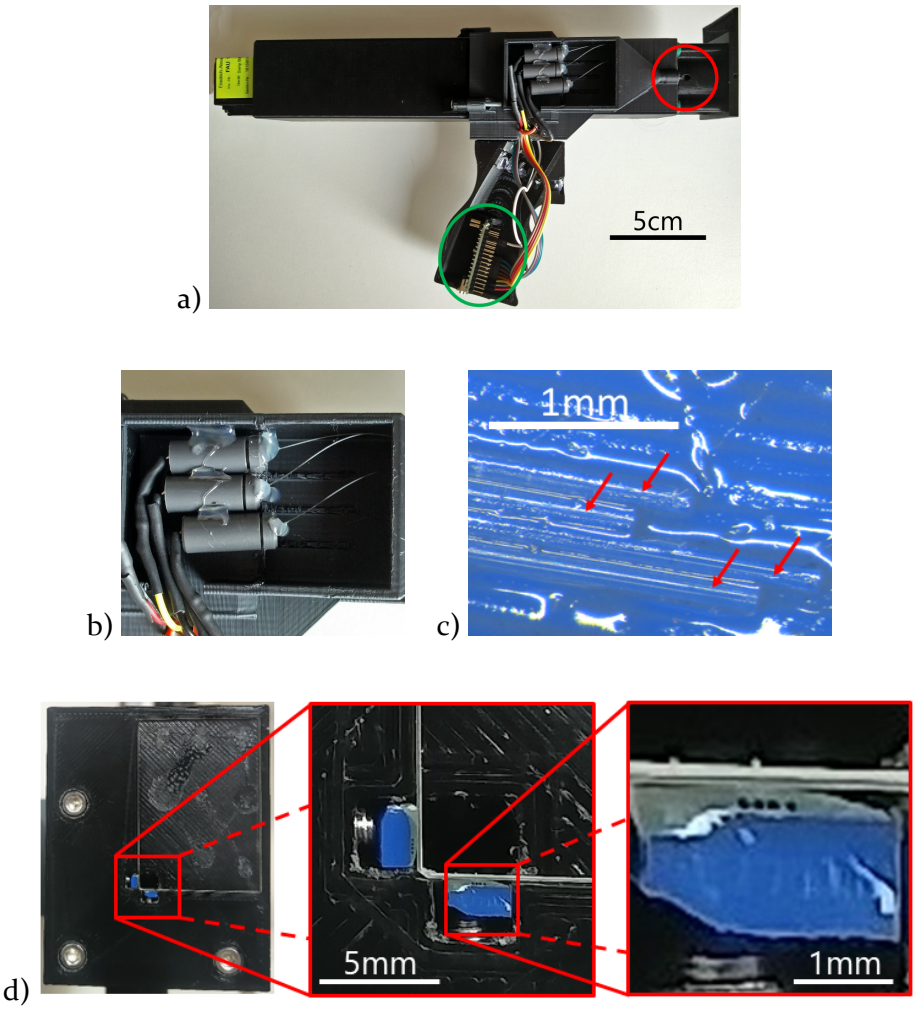

Figure 17: (a) Photograph of the side view of the sensor. The cover in the area of the LED light coupling is opened, as is the cover of the Arduino Nano (green circle). The optical fibres are guided into the head of the sensor (red circle). The coupling of the remaining three fibres is located on the opposite side of the sensor. (b) Detailed view of the LED light coupling. The house-made sockets can be seen, each of which contains an LED and a ball lens and from which the optical fibres lead out. (c) FDM auxiliary construction to hold the distal fibre ends (view parallel to fibres). The fibres are glued into the grooves with two-component epoxy adhesive. The block is afterwards polished from the front as described in the running text. The image shows four optical fibres (marked by red arrows), but only three of them were in use. (d) Front of the sensor with the cover glass. The first zoomed-in section of the image displays the aperture through which the detection optics are focused on the sample under investigation, as well as adjacent to that the two illumination fibre blocks. The second zoomed-in section shows the end of a fibre block, the four glued-in and polished fibres are clearly visible. [P5]

The power supply as well as the control of the individual LEDs is done by means of an Arduino Nano. Its position can be seen in figure 17a.

The housing was designed using CAD software and then additively manufactured with an FDM printer. This enabled optimal adaptation to and integration of the functional components introduced above. Special characteristics of the housing are as follows: 1) A plane-parallel glass plate was integrated into the front of the sensor so that the sensor could be placed on the object under investigation in a defined manner. That side of the glass plate facing towards the sample coincides with the working plane of the microscope objective described in the context of the detection unit (the alteration of the optical path length due to the refractive index of the glass was taken into account accordingly) - in other words: The detection system focuses on the sample surface. On two sides of this glass plate and in the direct vicinity of the detection aperture, the two illumination fibre blocks were mounted (see figures 17d and 18a). 2) For fine adjustment and focusing of the detection optics, the mounting of the glass plate is attached adjustably to the sensor main housing via O-rings. 3) To allow for comfortable handling of the sensor, an ergonomically designed grip is mounted on the sensor housing at its centre of gravity (grip based on [115]).

The coupling of the LED light into the optical fibres varies in quality in each of the single illumination strands. This becomes apparent when measuring the light intensity available at the sensor head. For quantification, the measuring device (PM100D with S130C, Thorlabs) was placed directly in front of the fibre blocks at the sensor head and the strands were switched on one after the other. Table 5 lists the measured values.

To compensate for these differences in the illumination intensity, the exposure time of the camera was adjusted accordingly. The aim was to achieve in the brightest region of each image (i.e. around the respective illumination fibre) pixels with pixel intensity values of approximately 95% of the maximum saturation. This calibration was carried out once for each of both phantoms (details on the phantoms to follow in the subsequent section). The resulting exposure times are given in table 5.

In order to define the positions of the LEDs along the edges of the imaging field of the SP-DRI sensor, the sensor was placed on a phantom and the LEDs were switched on serially. Cross-sectional planes were then generated at $y = 3000px$ (LEDs along the x axis) or $x = 4096px$ (LEDs along the y axis), respectively. Gaussian curves were then fitted to these curves to obtain the positions of the single LEDs. The procedure is demonstrated graphically in figure 18b and the resulting values are listed in table 5. As expected, the same values resulted also for the other phantom. Note: Although the light cones

exhibit an exponential decay, the Gaussian fit is sufficient to determine the LED positions; $R^2 > 0.96$ is true for all cases.

To obtain comparable results for the validation of the SP-DRI sensor, it was placed in an auxiliary mounting construction in the laboratory. In addition to a stable and invariable positioning, this auxiliary construction allows the optical phantom to be illuminated from below with white light. In this way, it is possible to ascertain prior to the actual SP-DRI measurements that there is in fact a thread structure - more precisely: a thread structure within the appropriate depth range as described in section 4.6.2.2 - within the optical phantom in the sensor's field of view. Furthermore, this transmitted light image can be compared with the SP-DRI reconstruction for validation purposes. For the actual SP-DRI measurements, this light source was not turned on.

For data collection, an LED was first switched on, then an image was taken with the exposure time defined in table 5 and stored to memory, and finally

Table 5: Technical and constructional data of the illumination used. The exposure time refers to the camera, not to the duration that the LEDs were switched on. The position of the LEDs is further illustrated in figure 18a. [P5]
Note: The high variance in the intensity values highlights the complexity of fibre handling and implies that a professionalisation of the fibre component production is advisable at a later stage to keep the coupling efficiency and thus the exposure times constant.

LED	Position regarding camera sensor	Intensity [µW]	Exposure [ms] for 10 µm phantom	Exposure [ms] for 20 µm phantom
#1	long side ($x = 1722px$)	12.0	115	200
#2	long side ($x = 1875px$)	5.1	270	480
#3	long side ($x = 2055px$)	0.7	1900	3450
#4	short side ($y = 2336px$)	12.4	180	270
#5	short side ($y = 1947px$)	1.6	1300	1900
#6	short side ($y = 1736px$)	5.7	380	540

the LED was switched off again. This procedure was carried out serially for all available LEDs and both optical phantoms.

The SP-DRI algorithm was applied to the data generated. Exemplarily, for each recording series the shift from LED #1 to LED #2 was analysed as well as the shift from LED #4 to LED #5. A 2-D Gaussian filter (σ: 5 px) was applied

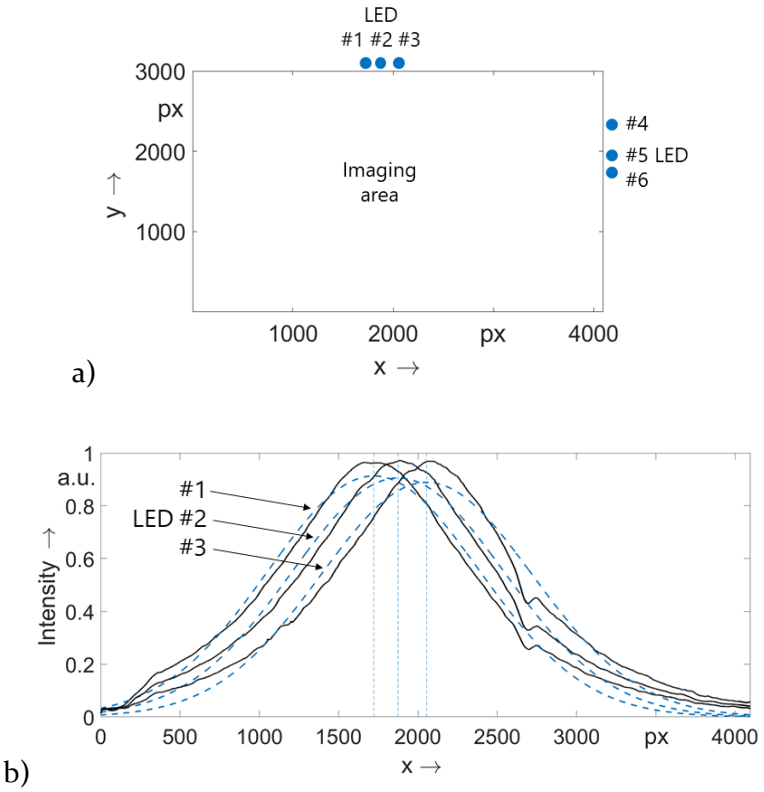

Figure 18: (a) Sketch to visualise the location of the imaging area of the SP-DRI sensor and the single LEDs (numerical values are given in table 5). The view taken here is from the direction of the camera (in contrast to figure 17d). To achieve a joint origin of both axes of the plot, the y-axis was flipped. This format was also chosen for the results section of this study. Note: Only six LEDs are shown because, as described, one LED per illumination block is kept as backup. (b) Exposure situation for the three LEDs running along the x axis for the phantom with a thread diameter of 10 µm. The single curves (black) were generated one after the other by placing the sensor on the phantom and turning on the respective LED. A cross-sectional plane at $y = 3000px$ through the recorded diffuse reflectance image was then taken. The Gaussian curves fitted to the raw data are shown as blue dashed lines ($R^2 > 0.96$ for all cases), the maxima of which were interpreted as the x positions of the LEDs. The procedure for the LEDs aligned along the y axis was identical. As expected, the same values resulted for the second phantom. Note: (b) is scaled to 1. [P5]

to the resulting division matrices. Cross-sectional planes through these data maps are additionally post-processed with a Savitzky-Golay filter (polynomial order: 5; frame length: 151 px). The results of this investigation can be found in section 5.11.

4.6.2 Optical phantoms

This section describes the design of the two types of optical phantoms used in the present doctoral thesis. For general details on optical phantoms, compare section 2.6.

4.6.2.1 Lipid-based phantom

This phantom is "composed of distilled water, lipid emulsion (Fresenius Kabi, Intralipid 20%) and black ink (Pelikan, Fount India). Their volumetric proportions were chosen such that the optical properties of the phantom are similar to those of skin in terms of μ_a, μ_s, g and n at $\lambda \approx 540$ nm, which was used for illumination. Since the phantom used in the experiments is a single-layered one, the target values for the optical properties were determined by averaging the respective values of the epidermis and the papillary dermis (compare table 3). According to literature references [116] and own spectrophotometric measurements (Shimadzu, UV-3600), this could be achieved with a mixture of 20 parts distilled water, 1 part lipid emulsion and 0.02 parts ink.

An uncoated tipless cantilever (Nanosensors, TL-CONT; length: 450 µm, width: 50 µm, thickness: 2 µm; material: silicon) from atomic force microscopy (AFM) was adopted as the structure inside the phantom. Using

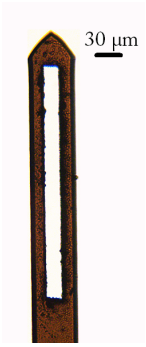

Figure 19: Transmitted light microscope image of the cantilever used in the optical phantom. To optimally mimic a capillary loop, material was removed from the cantilever over a large area by ultrashort pulse laser ablation. [P3]

ultrashort pulse laser ablation, the cantilever was processed to optimally mimic a capillary loop: It was possible to generate bars with a width of 13 µm, while the overall width of the cantilever and its arc shape are inherently consistent with the human anatomical dimensions." [P3] An image, taken with a microscope, of this modified cantilever is presented in figure 19; the layout of the phantom is displayed in figure 15a.

Note: "Although the cantilever is made of silicon and therefore reflective in contrast to the absorbing vasculature structures in the MC simulation models, this does not affect the proof of concept: In both cases, an opaque disturbance structure is introduced. The filling level of the phantom compound was chosen such that the phantom surface was 150 µm above the top of the cantilever - this corresponds to the conditions of the MC simulation domain and is anatomically correct." [P3]

4.6.2.2 PDMS-based phantoms

Except for a few modifications, this section is a reprint of my previously published article and taken from [P5].

The optical phantoms used were manufactured in-house. The matrix consists of two-component PDMS (RTV615, Momentive, USA). Black ink (Fount India, Pelikan, Switzerland) was used as absorber, while scattering was realised by adding TiO_2 with an average particle size of 200 nm (NO-0051-HP, Iolitec, Germany). The mass fractions were chosen to match the optical properties of the epidermis at 424 nm [S2]. For phantom preparation, both additives were initially mixed with the A component of the PDMS and then refined in an ultrasound bath. Subsequently, the PDMS B component was added and the mixture was degassed using a vacuum pump. After insertion of the microstructure (see paragraph below), the material was cured overnight in an oven at 60 degrees Celsius.

Surgical thread with a diameter of 10 µm (Dafilon 11/0, B. Braun, Germany) and 20 µm (Dafilon 10/0, B. Braun, Germany) was used to mimic human microvasculature. This suture material is made from polyamide 6.6, black coloured and hence optically absorbent. To mimic the capillary loop pattern, the thread was tightly wrapped around a cannula, fixed and stored overnight in an oven at 70 degrees Celsius. This allowed the thread to take on the loop pattern. Prior to introducing the thread into the readily prepared phantom matrix, it was pulled off the needle and then placed on top of the matrix. The optical phantom was then immediately brought to the oven. Due to gravity, the thread begins to submerge into the matrix, promptly being fixed in a position close below the phantom surface due to the onset of the curing

process. For the results presented in this article, with each of the two wires one final phantom was made (i.e. two final optical phantoms in total).

The depth of the thread structure within the optical phantom was estimated using a reflected light microscope. For this, it was first focused on the surface of the phantom and then, in a second step, on the thread inside the phantom. The resulting traverse path t was registered. Taking into account the refractive index of the phantom material n_2 as well as the numerical aperture A_N of the microscope objective, the depth of the structure $d_{structure}$ can be calculated as

$$d_{structure} = \frac{t}{(n_2 - \sqrt{n_2^2 - {A_N}^2})/(n_1 - \sqrt{n_1^2 - {A_N}^2})} \tag{8}$$

with $n_1 = 1$ being the refractive index of air [117–119].

The depth of the thread was measured several times for both phantoms, and in general it agreed very well with human anatomical conditions. Nevertheless, it cannot be completely avoided that the thread structure lies above or below this level in some areas. For the measurements in this doctoral thesis it was therefore ensured that - in accordance with the authors' preliminary research [P1–P3] - only those areas of the phantoms were investigated where the structures are within a depth of 150 µm to 300 µm. The results presented in section 5.11 relate to this accordingly.

5 Results and Discussion

This chapter of the present doctoral thesis reports the obtained research results and discusses them in the context of expectations as per the hypotheses and existing literature. For this purpose, the simulative domain (SD) as well as the experimental domain (ED) are resorted to. The procedure is to move from the general to the specific. In doing so, it is first of all necessary to evaluate the overall functionality of the SP-DRI method. This is done by simulations as well as in an experimental proof-of-concept setup.

After that, the optimal values for the illumination and detection parameters are identified in order to achieve a maximal SP-DRI signal. This is followed by an assessment of specificity, sensitivity (two-point discrimination), lateral resolution and imaging depth of SP-DRI. These basic characterizations are supplemented by investigations on the variability of the SP-DRI signal as a function of the diameter of the capillary loops - an important prerequisite for establishing a microcirculation sensor. In this regard, also variations in the optical properties of the simulated skin and their influence on this relationship were investigated, and the results thereof are finally given. For attaining an optimal understanding of the influencing factors within the scope of this fundamental research, all of this was done by means of simulations.

Lastly, these detailed simulative findings were used to physically construct an SP-DRI sensor. This sensor was tested on two different optical skin phantoms, the results on that will be presented towards the end of this chapter.

5.1 Functionality of SP-DRI (SD)

The evaluation of the functionality of the SP-DRI method mainly focuses on two aspects: First, it is essential to demonstrate that processing the diffuse reflectance data by means of SP-DRI provides added value compared to simply interpreting the raw data. Second, it needs to be investigated whether the SP-DRI signal reveals oscillations at those positions where capillary loops are indeed located according to the layout of the simulation volume.

Looking at the results in figure 20a and b, the first thing to notice is that the SP-DRI map exhibits apparent signal variations close to where the capillary loops are located in depth, while this is not the case for the raw data map; the latter is strongly dominated by the influence of the light source.

The consideration of the cross-sectional planes - taken at the positions where the diffuse reflectance data is expected to be affected by the presence of the capillary loops within the simulation volume - in figure 20c provides

further insights into this observed behaviour: The SP-DRI signal curves show a periodic pattern, with their local minima approximately being coincident

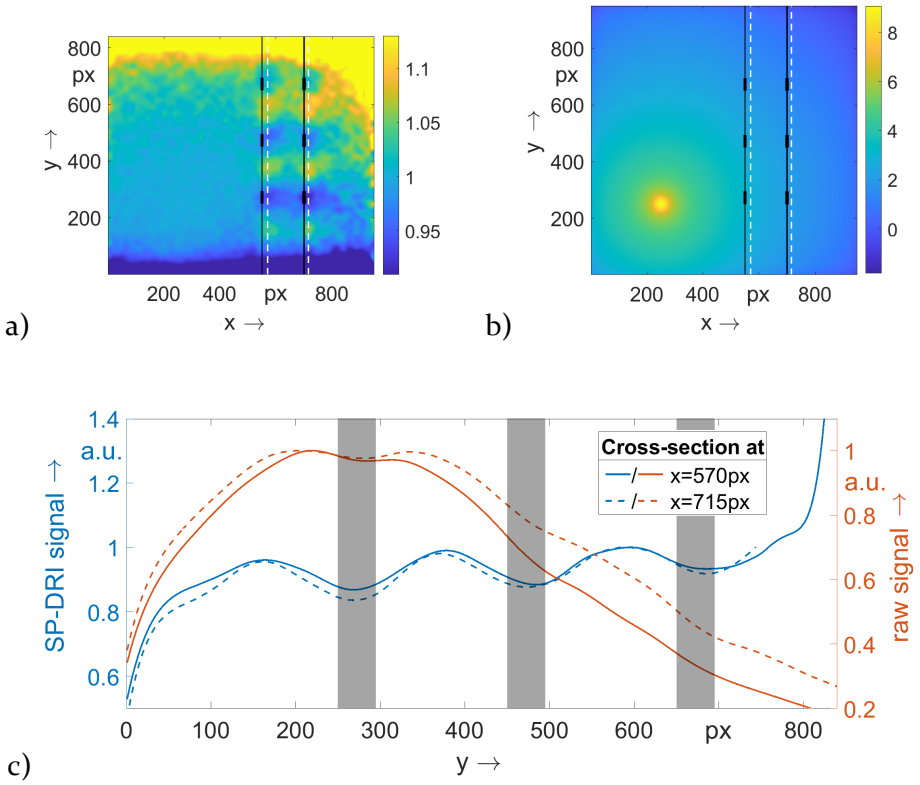

Figure 20: a) SP-DRI map for the default vasculature setup. The locations (projection to the surface) of the two vasculature branches are shown in black (the thin lines indicate the SVP, the broader sections thereon the capillary loops, compare image 12; as these lines are given for illustrative purposes only, their thickness does not match the scale). The white dashed lines indicate the positions of the cross-sectional planes used in c) to plot the signal curves. b) Logarithmised raw data map (matrix 1 of the two matrices underlying the SP-DRI map shown in a)) with the indicators as described earlier in a). c) Plot of the cross-sectional planes through the SP-DRI signal (left ordinate) and the raw data signal (right ordinate). The regions where the capillary loops extend along the y dimension of the simulation volume are shaded in grey, corresponding to the black broad markings in a) and b). To allow for a better comparison of the curves, each curve was normalized at its maximum (as the SP-DRI curves originate from 0 and trend towards infinity, more precisely: its maximum at $100\ px \leq y \leq 740\ px$); the range of values has thus been transformed compared to the maps in a) and b).
Note: Although the range of values differs for both ordinates of the plot, they both span 0.9 units to facilitate comparability. Due to the handling of infinity values by the Savitzky–Golay filter, the blue dashed curve terminates at $y = 744\ px$.

with the sections of the capillary loops along the *y* dimension (grey areas in figure 20c). Also the raw data curves exhibit alterations in the form of dips in these regions, but those are far less pronounced. It can thus be assumed that the positions of the capillary loops are indeed reflected in the SP-DRI signal curve. Therefore, the following applies to the SP-DRI method from now on: The area between a local maximum and the subsequent local minimum of an SP-DRI signal curve corresponds to one capillary loop.

Since SP-DRI is based on the division of two diffuse reflectance raw data sets (compare section 4.1), each of which - as discussed in the previous paragraph - exhibiting weak dips in intensity caused by the vasculature structure, it is in line with expectations that the SP-DRI signal is of periodic shape and that points of approximately the same phase correlate with the capillary loops. Following these considerations, it can be assumed that the specific appearance of such periodic SP-DRI curves depends on the specific parameters used with the SP-DRI method, in particular on the length of the illumination shift (as it also determines the extent to which the two raw data matrices with their respective intensity dips are shifted against each other) as well as on the illumination fibres and the detector used (as they determine the intensity proportions in both raw data matrices). The results of this are given in sections 5.3 and 5.4.

Summarizing the findings obtained so far, the results reported confirm the functionality of SP-DRI: The information content (in terms of the percentage modulation) is significantly increased compared to an evaluation of the raw data, and the SP-DRI signal can be related meaningfully to the configuration of the capillary loops. In this context, two aspects stand out: "First, the data of the SP-DRI normalization is not superimposed by the signal of the illumination fiber. Secondly, the signal contains only information of the capillary loops, but not of the slightly deeper superficial vascular plexus." [P3] This can be explained as follows: "Due to scattering and absorption by the capillaries, also the (structure-free) areas behind the capillaries are altered regarding their intensities, leading to a blur in this regions. With the SP-DRI normalization, this blur is present in both images required for this method so that it factually does not take effect. Since the superficial vascular plexus also emerges only blurred due to its depth, the same applies to it. As a result, only the capillary loops become visible with this normalization method." [P3]

5.2 Proof-of-concept setup (ED)

The general functionality of the SP-DRI method was also evaluated in a laboratory experiment. The main issue in this context was to determine whether perturbations in the dimension of human capillaries could also in

practice be detected by this technique - as already suggested by simulations in the previous section. The experimental approach described earlier in method section 4.6.1.1 was used to address this research question. The results obtained from this are given in figure 21 [P3].

Taking a look at these findings, "it is evident that the cantilever structure can be clearly identified as such in the x-y map and the cross-section through the perturbation along the x axis. Since this structure is of the order of a capillary loop, it is reasonable to assume that the latter can be detected with the SP-DRI method, in particular also because the matrix of the employed optical phantom adequately mimics the optical properties of skin.

The width of the structure appears in the diffuse reflection data in line with expectations: By taking into account the width of the cantilever, the magnification factor of the detection setup and the size of a camera pixel, this cantilever width" [P3] can be calculated to be 60 px. This is also the dimension that can be inferred from the measured data shown in figure 21a. "Furthermore, the distortion in the SP-DRI signal is consistent with the location of the cantilever relative to the camera image.

In this respect, with an AFM cantilever it has been successful to introduce a structure that is stable and practical to handle despite its very small dimensions. It was possible to transfer this already small structure into the shape of a capillary loop by laser processing, with the loop having anatomically correct proportions. This approach allowed to perform reproducible experiments as

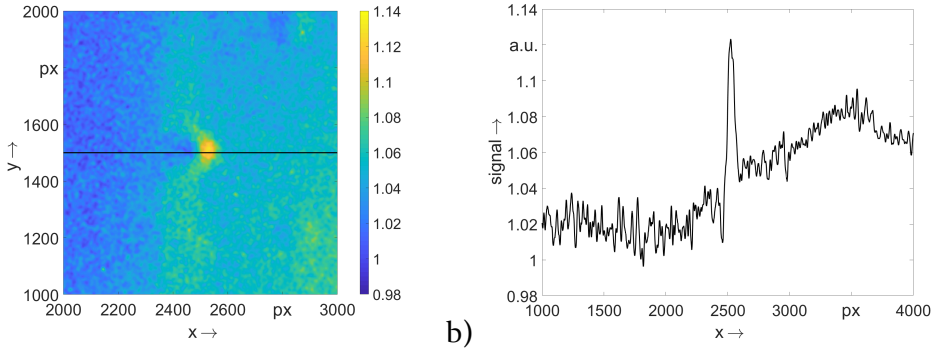

Figure 21: Results of the laboratory experiment for the proof of concept of the SP-DRI normalization method. a) Image of the result, where the position of the cantilever structure inside the optical phantom is clearly visible. The position of the illumination fibre is not shown here as it is outside of the range illustrated on the map. b) A cross-section through the image from a) at the position $y = 1500\ px$. [P3]

it would have been almost impossible with, for example, harvested porcine capillaries as they are neither stable nor robust.

Compared to the absorbing human capillary loop, this cantilever is highly reflective. This, however, does not alter the experiments at all: The reflecting silica increases the backscattering, resulting in a brighter area instead of a darker one at the surface. This effect will create a photon source instead of a sink relative to the substrate. Accordingly, in the simulation domain with its absorbing structures a (...) positive deflection in the SP-DRI signal is followed by a (...) negative one. In contrast, in the experimental domain with its reflecting structure a (...) negative deflection is followed by a (...) positive one. The two configurations thus produce comparable SP-DRI signals that only differ in the sequence of the peaks, while their amplitudes are virtually equal. In terms of a mathematical differentiation (which the SP-DRI method actually is), this behavior is in line with expectations. In summary, the cantilever as interfering structure serves as a valid proof of concept: SP-DRI is capable of detecting pertubations of the order of human capillaries - absorption and reflection, respectively, are indicated by the sign of the signal." [P3].

5.3 Influence of the A_N of the detection (SD)

This section deals with the influence of the A_N of the detection fibres or the objective used for detection on the amplitude of the SP-DRI signal. For reasons of consistency, the results shown in this section base on the optimal illumination parameter values arising from section 5.4; they could, however, also be reproduced with any other set of illumination parameters.

In addressing the search for the optimal value of this respective detection parameter, two contrasting effects must be taken into account: With increasing values for A_N, the amount of detected photons and thus the light intensity at the detector increases as more and more photons incident at larger angles are accepted. At the same time, however, this leads to a decrease in the mean amplitude of the SP-DRI signal: Photons incident at larger angles tend to originate from regions closer to the surface and thus, on average, are less affected by the capillary structures than the steeper photons originating from deeper layers (in the extreme case, the latter were absorbed by the capillary structure and as such contribute to the SP-DRI modulation). Thus, increasing the angle of acceptance results in an attenuation of the SP-DRI signal [P6]. Figure 22 illustrates this situation graphically.

Having a potential experimental setup in mind, the effect described at first can be compensated comparatively well by increasing the exposure time of the camera (at some point, of course, limited by blurring effects due to object

movements). Therefore, it is expedient to particularly consider the influence of the detection A_N on the mean SP-DRI amplitude.

In line with the selected capillary structure, for each value of A_N up to six capillary loops could be evaluated. Per capillary loop, the modulation parameter A_{norm} was calculated as defined in equation 3. For each detection A_N, the

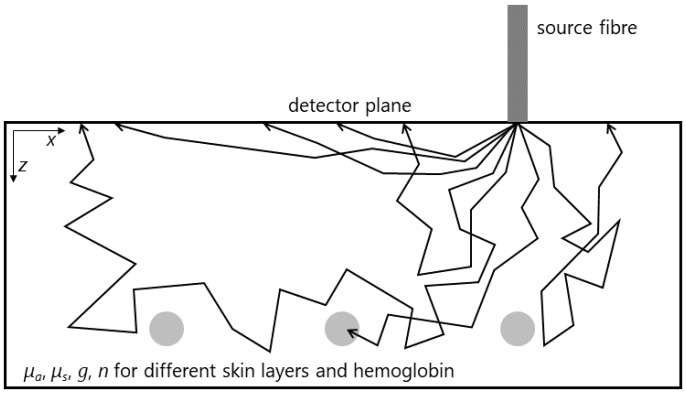

Figure 22: Exemplary photon paths through the medium under investigation. Larger exit angles usually belong to more superficial paths, while steeply emerging photons tend to have penetrated deeper layers of the volume. Blood vessels are drawn as grey circles to illustrate the context. The diagram is not to scale.

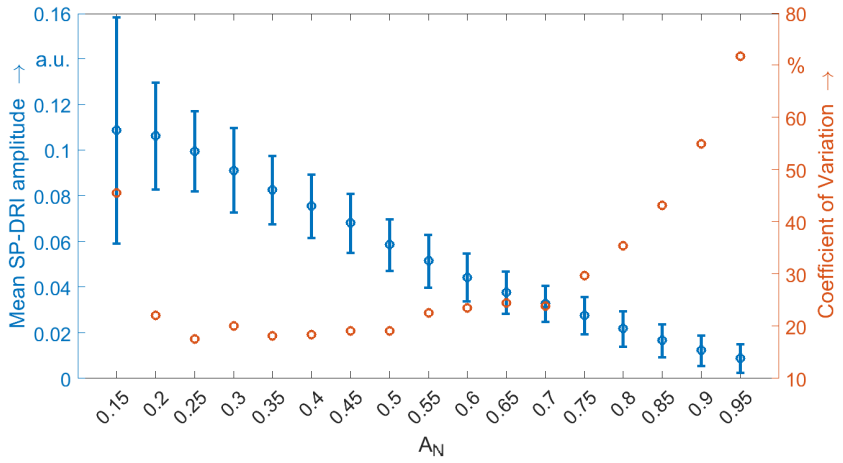

Figure 23: Illustration of the SP-DRI amplitude mean values and related standard deviations (left ordinate) as well as the CV resulting from these values (right ordinate) for different values of the numerical aperture A_N applied to the detection.

mean value and the standard deviation of all loops were then computed. Additionally, the CV was evaluated as the standard deviation can be interpreted only to a limited extent in the context of large differences in the mean values. These values are plotted in figure 23.

According to these results, a value of $A_N = 0.25$ can be considered as optimal: Still at a very high average signal modulation, a minimum of the CV is present; the latter is of importance as it means that the modulation amplitude does not depend on the (lateral) position of the capillary loops within the volume. Significantly lower values than the one mentioned lead to a situation where capillary loops too far away from the illumination cannot be detected. This effect is shown in figure 24a and 24b (it is also the reason for the high standard deviation and CV of the data set of $A_N = 0.15$, see figure 23). In figure 24d, on the other hand, the effect of blurring of the SP-DRI signal as a consequence of too high detection A_N values can be observed.

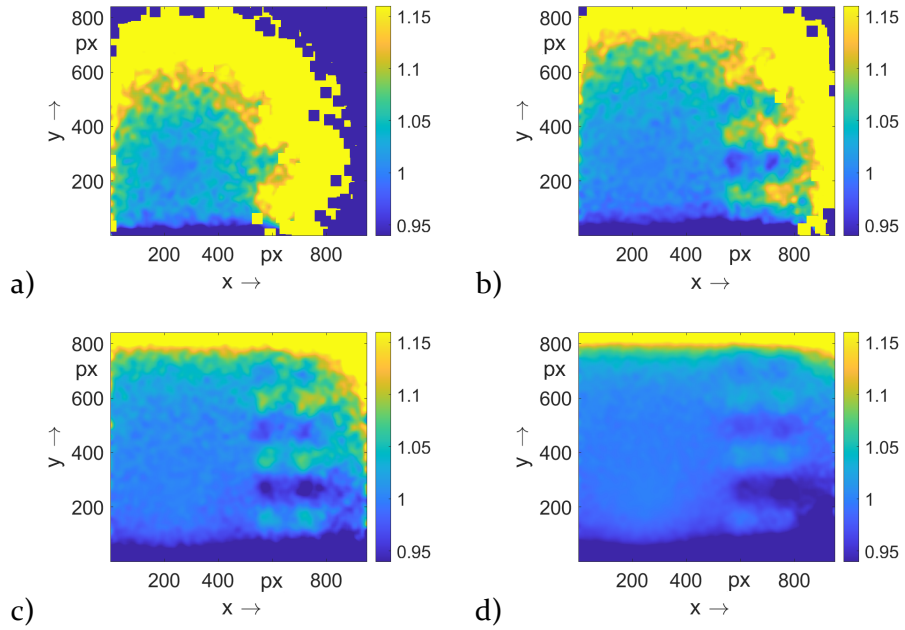

Figure 24: SP-DRI results for different values of the numerical aperture A_N applied to the detection: (a) $A_N = 0.10$, (b) $A_N = 0.15$, (c) $A_N = 0.25$, (d) $A_N = 0.60$. The blue and yellow areas (noticeable angular patterns) in the upper right regions of the images in (a) and (b) have values of 0 and ∞, respectively, as a consequence of the lack of photons in these areas in the input matrices of the SP-DRI algorithm (the position of the illumination is (250 px|250 px)).

5.4 Influence of the illumination parameters (SD)

This section investigates to what extent different parameters of the illumination influence the detectability of the capillary loops by SP-DRI. In this context, the three key parameters are A_N and $\emptyset_{\text{Core}}$ of the illumination fibre as well as its lateral shift inherent to the SP-DRI process. This analysis was performed for all possible combinations of the three parameters. In line with the previous results, $A_N = 0.25$ was considered for photon detection.

Again, for each illumination parameter combination six capillary loops could be evaluated. To determine the optimal parameter combination, the relative modulation difference was assessed by means of the modulation parameter A_{norm}.

As explained in section 5.3, a high average modulation amplitude along with a low standard deviation is desirable also in this context. In figure 25, the result is plotted showing the five parameter combinations leading to the

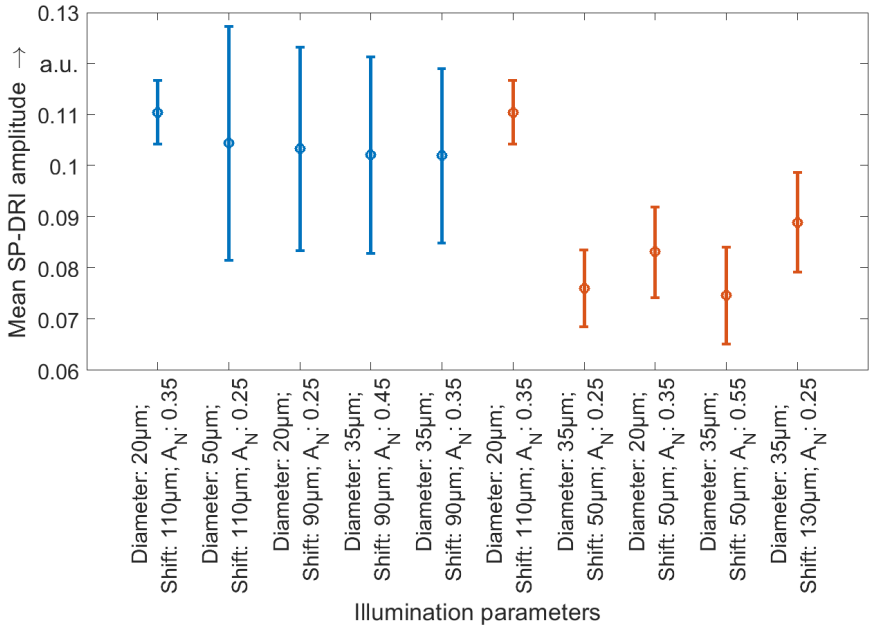

Figure 25: Illustration of SP-DRI amplitude mean values and related standard deviations for different combinations of the three illumination parameters (A_N and diameter of the illumination fibre, illumination fibre shift). For the plot, the five parameter combinations leading to the highest means (blue) and the five combinations leading to the lowest standard deviations (red) were selected.

highest means of the amplitudes and the five combinations yielding the lowest standard deviations. The mean values are not that divergent in this case, it is therefore not necessary to resort to the CV as metric.

Looking at the results, the first thing to note is that it is possible to draw conclusions about the capillary loops not only with one specific set of parameters: Many of the mean amplitudes are well above 0 and many of the standard deviations are also within a reasonable range. Nevertheless, one set of parameters clearly stands out to be optimal: The application of an illumination fibre of core diameter $\emptyset_{\text{Core}} = 20\,\mu\text{m}$ and $A_N = 0.35$ that is shifted by 110 µm yields both the highest mean SP-DRI amplitude and the lowest standard deviation for the simulation setup considered.

Summarizing the findings of this section, it can be stated that the detection of capillary loops in human skin using SP-DRI leads to the most beneficial results in terms of a high SP-DRI signal modulation when the illumination is based on the parameter set just mentioned. Consistent with the lowest standard deviation, this combination also exhibits the least standard error of the mean (SEM) as the number of observations is equal for each parameter combination. It can therefore be assumed that the basic population is best represented with the parameter set stated. It must, however, be borne in mind that this optimisation only applies to specific depths and distances of the capillaries. Individual deviations might therefore influence the success rate. Still, the results presented give an idea of the signal range that can be achieved with SP-DRI.

5.5 Specificity of SP-DRI (SD)

Specificity describes the ability of a diagnostic procedure to identify an absent feature as such. Transferred to SP-DRI, this implies that it is required to evaluate whether the method detects missing capillary loops as such (and does for example not report artefacts stemming from other tissue components). Thus, to address this research question, parts of the default vasculature were removed as described in section 4.2.2.3: In one case, an entire vasculature branch was removed from the simulation volume, and in the other case, one capillary loop was removed from each of the two vasculature branches enclosed. The related results can be found as SP-DRI maps and a signal plot in figure 26.

The first thing to note is that the presented signal maps allow to make a statement on the location of the capillary loops. Vice versa, also the absence of such loops can be judged. In the case of the removed third capillary loop, figure 26d shows - compared to the default setup - a missing peak at

$y \approx 600\ px$. In the case of the completely removed vasculature branch, the peaks in the SP-DRI signal are missing at all. The expected behaviour is thus revealed both times. As the simulated capillary distances represent anatomically correct conditions, it can be assumed that no *ghosts* will be created.

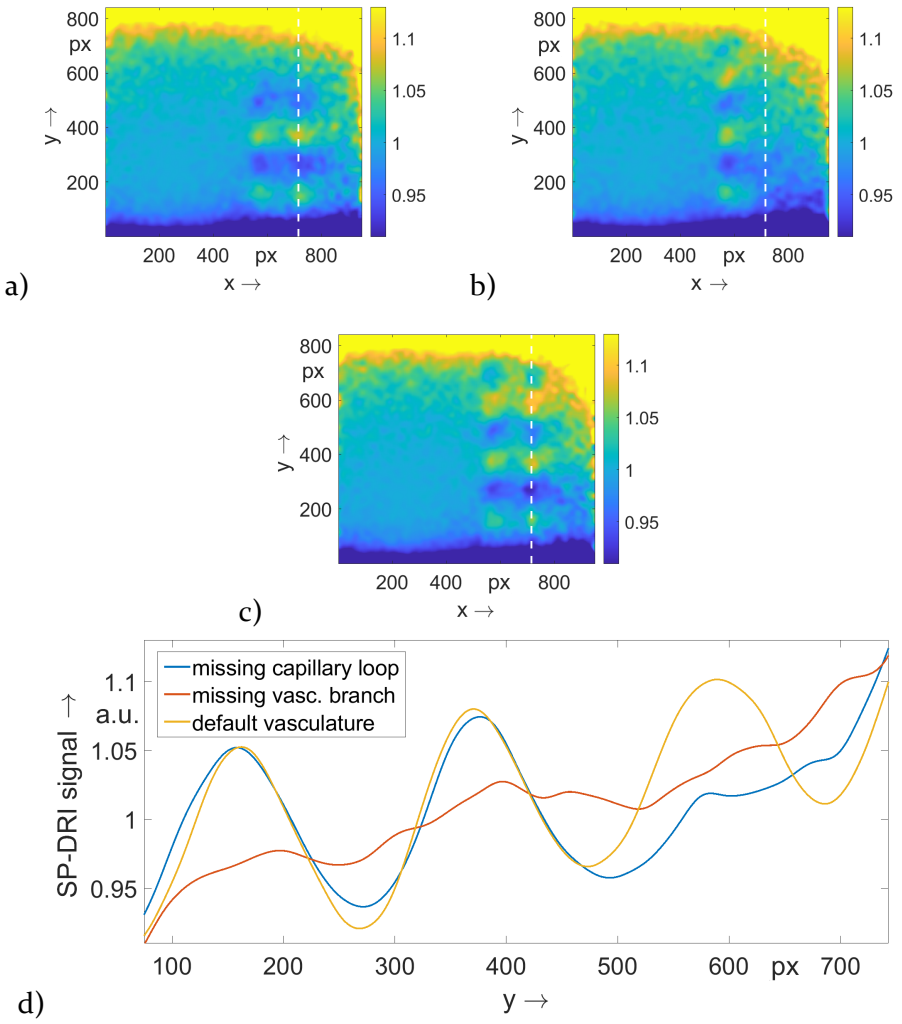

Figure 26: SP-DRI maps for a) a missing third capillary loop at each of both vasculature branches and b) a completely absent vasculature branch in comparison to c) the default vasculature setup. In all three graphs, the white dashed line at $x = 715\ px$ indicates the position of the cross-sectional plane that is used in d) to plot the SP-DRI signal curves.

The findings reported in this section indicate a high level of specificity of SP-DRI: "It was shown that the absence of a capillary loop is reflected as such by the SP-DRI technique. This may sound rather trivial, but points to an important property of SP-DRI (...): The slightly deeper superficial vascular plexus is not falsely detected as a capillary loop by the technique. It is therefore possible to detect exclusively the position of the capillary loops with the SP-DRI method." [P3] A detailed justification for this is given in the last paragraph of section 5.1.

Beyond that, the results presented permit a second conclusion: In the case of one missing vasculature branch, the still remaining second branch does not affect the SP-DRI signal at the position of the missing (first) branch. "It is important to note that regions between two adjacent vasculature branches can be identified as structureless. Since the spatial arrangement of the capillary loops relative to each other is in an anatomically correct scale in the simulation volume, this observation" [P3] provides some initial indication that the lateral resolution of SP-DRI may be sufficient for the detection of capillaries in human skin [P3]. This topic will be discussed in detail in section 5.7.

5.6 Ability for two-point discrimination (SD)

Sensitivity refers to the capability of a diagnostic procedure to identify the presence of a feature as such. For SP-DRI, this means that a capillary loop located in the volume under investigation can be detected by this method. The ability for two-point discrimination is directly connected to this concept: Are two capillary loops distinguishable when placed at an anatomically correct distance from each other?

To address this research question, the vasculature structure was randomly placed in the simulation volume as described in detail in section 4.2.2.4. For the simulation run discussed below, the following positions were generated randomly:

- vasculature branch 1: $x = 432\ px$; $y_1 = 233\ px$, $y_2 = 423\ px$, $y_3 = 631\ px$
- vasculature branch 2: $x = 738\ px$; $y_1 = 234\ px$, $y_2 = 423\ px$, $y_3 = 582\ px$

The corresponding results are illustrated as SP-DRI map and signal plot in figure 27. The map shown there strongly allows to deduce "that an easy and clear determination of the positions of the capillary loops is possible for the random vasculature configuration. This statement is also supported by the diagram containing the corresponding cross-sectional planes. It is important to note once more that the data doesn't contain information about the connective superficial vascular plexus that is located slightly deeper within the tissue volume. (...)

The evidence in this section therefore suggests a sufficient ability of two-point discrimination of the SP-DRI method: If a capillary loop is present, it can be identified and detected as such by the technique." [P3] SP-DRI is sensitive to capillary loops. Note: "The single capillary loops were placed in anatomically correct spacing to each other in the simulation volume. Under these conditions, the different capillary loops were clearly distinguishable in the SP-DRI signal. As only 25% to 50% of the human capillary loops are perfused with blood at any given time [65], this is a very conservative estimation (if only a fraction of all capillary loops is perfused at the same time, this numerically corresponds to a larger lateral spacing - therefore, the required lateral resolution of the DRI system could even be lower)." [P3]

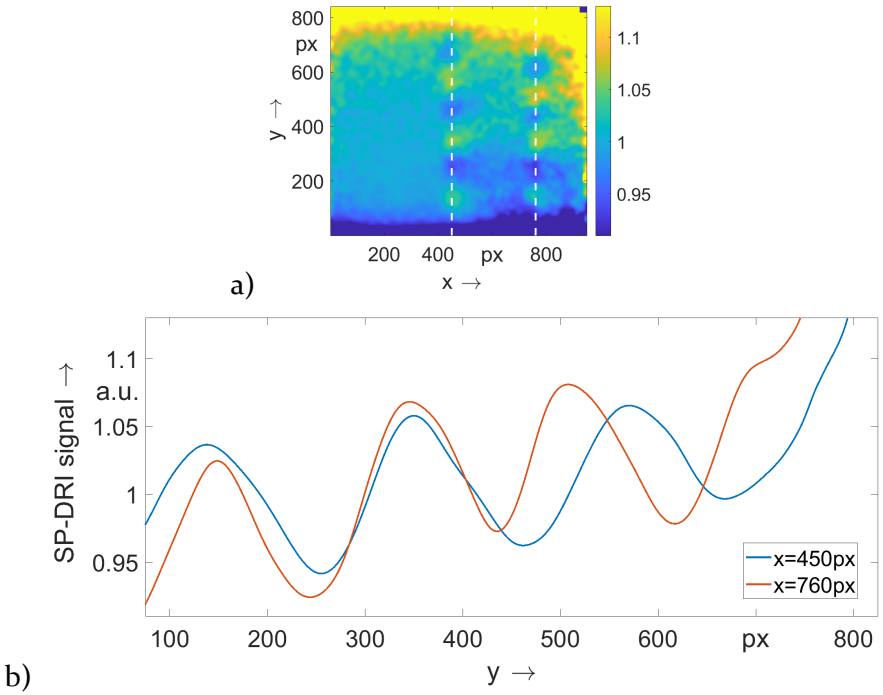

Figure 27: a) SP-DRI map for the random configuration of the vasculature elements within the simulation volume. The white dashed lines at $x = 460\ px$ and $x = 750\ px$ indicate the positions of the cross-sectional planes that are used in b) to plot the SP-DRI signal curves.

5.7 Lateral resolution and imaging depth (SD)

This section of the present doctoral thesis covers the results for the investigation of the lateral resolution and the imaging depth of SP-DRI. As described earlier as part of the methods chapter (see section 4.2.2.5), the vasculature was progressively placed deeper into the simulation volume (imaging depth) and the intercapillary distance was reduced (lateral resolution), respectively, for that reason. The results for this are shown in figure 28, using only the left of the two vasculature branches as an example; the results obtained for the second branch are almost equivalent.

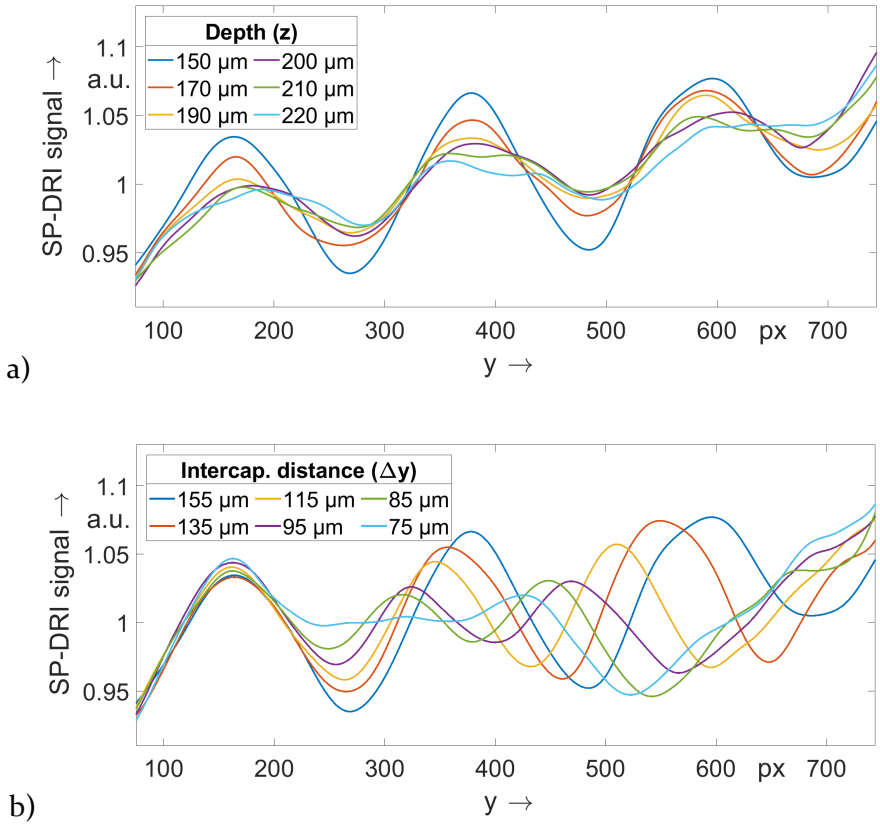

Figure 28: a) Plot of cross-sectional planes at $x = 570\ px$ through SP-DRI maps resulting from vasculature configurations with different depths within the simulation volume. The numerical values given refer to the upper margin of the capillary loops. b) In analogy to a), but for different intercapillary distances Δy (all at a depth of 150 µm).

Two phenomena are noticeable: "On the one hand, the amplitude of the graphs changes when varying the resolution parameters, and on the other hand, the position and number of local maxima and minima along the abscissa differ. Bearing in mind that a capillary loop is located (...) between a local maximum and the subsequent local minimum of the SP-DRI signal [P1, P3], these alterations are in accordance with expectations.

To determine the imaging depth, figure 28a can be consulted. The two capillary loops are clearly distinguishable for the initial depth value (...). With increasing depth of the capillary loops, the amplitude and thus the differentiability of the single structures gradually decrease." [P4] At a depth of 210 µm (all depth specifications made here refer to the upper margin of the capillary loops; this is different from a definition in literature, where the numerical values refer to the mean axial loop propagation [P4]), the amplitude of the SP-DRI signal has already dropped to a level where it is no longer feasible to accurately determine the position of all capillary loops; it is, in particular, difficult to do so for the capillary loop that is located furthest away from the illumination. The imaging depth of SP-DRI is therefore at least 200 µm, which is the previous step examined.

"In humans, the number of capillaries at a depth of 100 µm, 200 µm, 250 µm, 300 µm and 400 µm is 44, 18, 14, 8 and 5, respectively [65]. With its imaging depth (...), SP-DRI is thus technically capable of detecting most of the capillary loops." [P4] Note: In the previous sections, the detection and illumination parameters have been optimized for the default vasculature configuration; it is therefore reasonable to assume that the imaging depth could be further improved with a proper optimization of the parameters for deeper vasculature settings.

Evidence for the lateral resolution can be obtained by interpreting figure 28b. For the default depth of 150 µm, a separation of the three capillary loops by means of the SP-DRI signal is possible for nearly all intercapillary distances Δy plotted - only when reaching $\Delta y = 75$ µm, this is no longer the case. Accordingly, the lateral resolution can be defined as being not better than 85 µm. "According to literature, the intercapillary distance ranges from 96 µm to 166 µm (mean: 137 µm, SD: 13 µm) [72]. Again, these values are in a scale that SP-DRI with its lateral resolution is able to resolve." [P4]

It is important to note that the lateral resolution reduces with an increasing depth of the microvasculature; therefore, it is a depth-dependent parameter. [P4] At $z = 190$ µm, the lateral resolution has reduced to around 95 µm, and at $z = 200$ µm (maximum imaging depth), its value is about 105 µm. "Putting these values in the context of the just reported depths and spacings of human capillaries, they are still on a reasonable level." [P4]

5.8 Determination of the capillary diameter (SD)

In order to serve as a diagnostic technique for the assessment of microcirculation, SP-DRI must be capable of detecting changes in the latter in terms of a constriction or dilation, respectively. This section presents the relevant results in this context. As in the previous section, only the left of the two vasculature branches will be discussed in the following by way of example.

To give a general idea of the available data, figure 29 provides one cross-sectional plane through the corresponding SP-DRI maps for each simulated capillary diameter. It is apparent that the curves differ in their amplitudes depending on the capillary diameter. This is true for all three capillary loops present. Furthermore, the local extrema are determined successfully [P1]. Note: 10 data sets were available per diameter, see section 4.2.2.6; for figure 29, one of them was selected at random.

A quantitative characterization of the SP-DRI curves is possible based on the modulation parameters introduced in section 4.3. For K_{norm} (this time, including all of the 10 data sets per capillary diameter), this is shown graphically in figure 30: The means and standard deviations of the parameter values were plotted once separately for the three capillary loops considered and once without making this distinction. Considering the results given in figure 30,

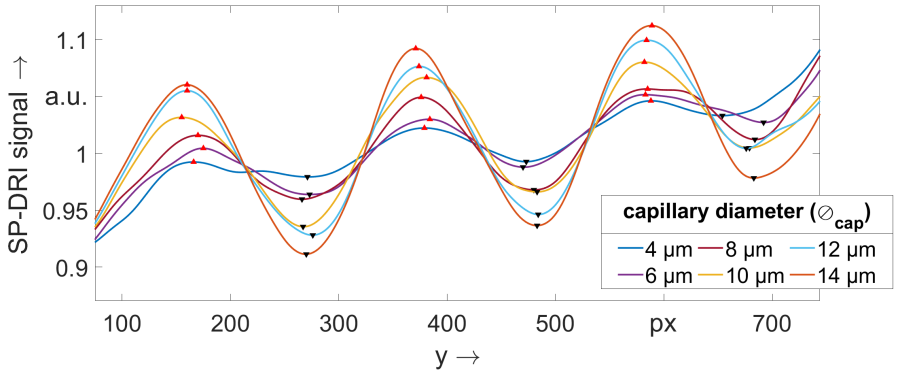

Figure 29: Plot of cross-sectional planes at $x = 570\ px$ through SP-DRI maps resulting from vasculature configurations with different diameters of the capillary loops. The positions of the local maxima that were automatically detected by the evaluation algorithm are illustrated as red upward-pointing triangles, while the positions of the local minima are marked as black downward-pointing triangles. As already described earlier, a pair of a local maximum and its subsequent local minimum of the SP-DRI signal curve can be associated with one capillary loop. Therefore, each of the six curves depicted indicates three capillary loops. Per capillary diameter increment, the figure shows one of the ten simulated data sets.

it is evident that K_{norm} increases in all cases when the capillary diameters widen [P1].

The data presented suggests a linear relationship. To support this statistically, a linear regression was performed; the fundamentals underlying this analysis have already been described in section 4.4: The influence of the independent variable (diameter of the capillary loops) on the dependent variable (modulation parameter K_{norm}) is explained taking into account the regression parameters β_0 and β_1. The numerical values of the latter, which result for the given data, are provided in table 6 [P1]. In addition, the values of the adjusted coefficient of determination $\bar{R}^2$ can be found there, greatly supporting the assumption made and confirming "that there is an almost perfectly linear relationship between the diameter of the capillary loop and the normalised modulation parameter K_{norm}" [P1] in all cases.

Concluding on the basis of the results shown in this section, it can be stated that variations in the capillary diameter of only a few micrometers are reflected in the SP-DRI signal: "K_{norm} as a metric for the amplitude of the SP-DRI signal clearly varies depending on the diameter of the capillary structure within the tissue. As shown, this relationship is almost perfectly linear in the investigated parameter range from $\emptyset_{\text{cap}} = 4\,\mu\text{m}$ to $\emptyset_{\text{cap}} = 14\,\mu\text{m}$. The calculated adjusted coefficients of determination $\bar{R}^2$ confirm that. Consequently, it can be stated that K_{norm} increases proportionally with increasing capillary diameter.

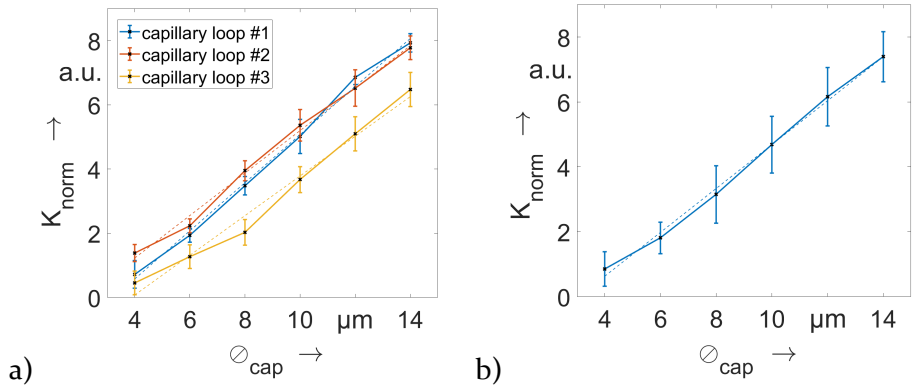

Figure 30: Means and standard errors of the K_{norm} values for different diameters of the incorporated capillary loops. In a), the three positions of the capillary loops are considered separately (thus, $n = 10$ per loop), and b) shows the overall result ($n = 30$). The respective linear regression curves are indicated by dashed lines; the related statistical parameters can be found in table 6.

Table 6: Results of the linear regressions conducted.

Condition	β_0	β_1	$\bar{R}^2$
capillary loop #1	-2.4104	0.7483	0.9951
capillary loop #2	-1.4100	0.6609	0.9934
capillary loop #3	-2.3887	0.6174	0.9777
overall	-2.0697	0.6756	0.9951

This finding implicates (...): The normalised modulation parameter K_{norm} found in this study seems to be a meaningful and definite index for quantifying the SP-DRI signal. Changes in the signal are reflected in parameter alterations, where the latter may well be interpreted in their direction and magnitude. The SP-DRI technique in combination with the normalised modulation parameter K_{norm} is able to effectively quantify capillary diameter changes. Differences in the capillary diameter (at least within the 2-micron increments studied) can be clearly visualised using SP-DRI.

In the present study, the same MC simulation was performed 10 times for each capillary diameter increment (...), with the seed being determined randomly each time to ensure unique simulation results. The presented metrics can thus be interpreted as intra-person variability: The measuring probe is firmly fastened to the subject such that any movements do not influence the measurement. Thus, within this subject the same capillary loops are monitored over a period of time, and changes in the diameters of that capillaries are detected. By always examining the same spot, it is not a fluctuation of the optical properties that significantly influences the SP-DRI signal, but noise. Exactly this noise is present in the data due to the repeated execution of the MC simulation. Consequently, the data presented reflects the important clinical situation of (long-term) patient monitoring." [P1]

As already mentioned, the position of the capillary loops was once considered in the linear regressions and once not. Considering this, "it is noticeable that the slopes have nearly identical values, while the intercept differs. This means that two emerging effects can be clearly separated: The previously discussed influence of the diameter of the capillary loops is reflected only in the slope of the regression curve (the diameter behaviour is the same in all (...) cases, leading to comparable slopes), whereas the distance between the illumination and the position of the capillary loop determines the intercept." [P1]

Even in the case that the distance mentioned above (commonly known as SDS) is not considered, it is possible to estimate the diameter of the capillary loops on the basis of K_{norm} - this is supported by the results shown. If, however, the SDS (and hence the associated intercept) is known, even absolute diameter values can be attributed to the measured K_{norm} values (if the depth of the capillaries is known). Therefore, an absolute diameter quantification will also be feasible in situations with many capillary loops and thus SDS [P1].

5.9 Influence of the illumination wavelength (SD)

According to the hypotheses, the absorption and scattering properties of the probed medium affect the detectability of vasculature by SP-DRI. The results presented in this section are intended to confirm this by using an illumination wavelength $\lambda = 540\,\text{nm}$ instead of the illumination with $\lambda = 424\,\text{nm}$ that was used so far. As in the previous section, six different capillary diameters were investigated.

The results for this simulation run are illustrated in figure 31. For proper interpretation, this graph must be compared to the curves given in figure 29, where all parameters except for the illumination wavelength are identical. For all capillary diameters, it can be seen that the amplitudes of the SP-DRI signal curves are substantially reduced for the longer wavelength compared to the amplitudes that can be obtained when the shorter wavelength is applied. This relationship is also described in table 7 in terms of the modulation parameter K_{norm}; this value is approximately doubled for the shorter wavelength.

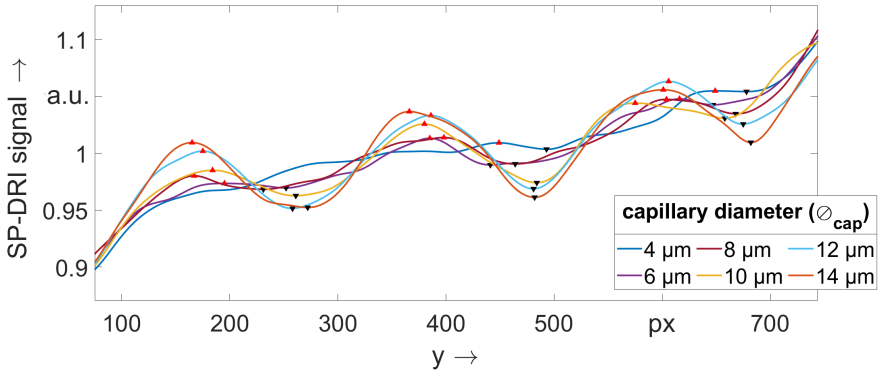

Figure 31: Plot of cross-sectional planes through SP-DRI maps at $x = 570\,px$ for an illumination wavelength of $\lambda = 540\,\text{nm}$. Except for the different illumination wavelength, this graph was generated by analogy with figure 29; therefore, it is referred to the caption of the latter for details on the present plot.

Table 7: K_{norm} values for the middle capillary loop of the standard vasculature configuration for each capillary diameter and illumination wavelength. The values of the first row of the table refer to the data plotted in figure 29, the values of the second row refer to the data plotted in figure 31. The declaration of an accuracy measure is omitted as each K_{norm} value refers to only one simulation run; nevertheless, a measurement error is inherent to a MC simulation as a stochastic process.

	K_{norm} [a.u.] for a capillary diameter of					
λ [nm]	4 µm	6 µm	8 µm	10 µm	12 µm	14 µm
424	1.4066	2.0782	4.3163	5.1838	6.6070	8.0306
540	0.2869	1.2311	1.2348	2.6998	3.0177	3.1416

The numerical values which have been applied for the optical properties in the two simulated cases can be found in table 3. Looking at these values, it is noteworthy that μ_a of the microvasculature differs by a factor of about 7, while the other values are comparatively similar or even identical. As this also applies to the scattering properties of the medium, it is justified to not re-optimize all simulation parameters (like the numerical value of A_N of the detection), but to adopt the optimized values resulting from the previous investigations based on $\lambda = 424$ nm also for the case of $\lambda = 540$ nm. The error introduced by this is considered to be negligible.

Since, as stated in the previous paragraph, the main difference between the two simulated illumination regimes is found in the absorption properties of the vasculature, it can be concluded that the loss in the achievable modulation in the case of $\lambda = 540$ nm is "due to the reduced contrast between hemoglobin and the surrounding tissue" [P3].

The two illumination wavelengths investigated are in the range of the two strongest local maxima of the absorption coefficient curve of haemoglobin in the visible wavelength range. Following this line of reasoning, a higher contrast can only be achieved with an illumination wavelength of $\lambda = 424$ nm, which is thus recommended for an optimal SP-DRI signal. "Although this is a wavelength range that is preferably avoided in the context of medical diagnostics due to the comparatively high energy of the photons, it must be pointed out that only low doses of incoherent light are required for DRI and that the diagnose system will only be applied for a short time. Therefore, it can be assumed that the threshold for the exposure of skin can be maintained [120] and that this does not impose a limitation on the applicability of the system; detailed calculations on this will have to follow as soon as a first properly dimensioned system for the *in vivo* application is available." [P3]

5.10 Prediction of the regression parameters (SD)

As described earlier, it is possible to quantitatively deduce the capillary diameter by determining K_{norm} and the regression parameters β_0 and β_1 (see equation 7). Here, β_0 and β_1 result from the regression line obtained when varying the capillary diameter (refer to section 4.4). This variation, however, can only be induced in the simulative domain, not in real-life measurements. It is, therefore, crucial to develop a procedure that allows the prediction of the capillary diameter without prior knowledge of the regression parameters β_0 and β_1 [P2]. This is the aim of the investigations presented in this section. The underlying simulation parameters are given in section 4.2.2.8, the complex methodological procedure is described in section 4.5.

In this section, the slope β_1 is analysed at first, followed by an analysis of the intercept β_0. Afterwards, it is investigated if it is possible to predict the capillary diameter on the basis of a prediction of β_0 and β_1.

Except for a few modifications, the following part of this section is a reprint of my previously published article and taken from [P2].

Regarding the slope parameter β_1: As explained in the framework of the methods, all 24 optical properties values (μ_a, μ_s' and n for each of the seven skin layers and for haemoglobin) were included into a RF model to determine the importance of the prediction parameters. The response was β_1. It was found that $R^2_{oob} = 0.7779$. The result on the importance of the predictors within this regression model is shown in figure 32a.

According to the results of the importance, the μ_s' values of the first two skin layers were included as predictors in the subsequent model for the slope. The 30 calculated models (compare section 4.5) use LSBoost as ensemble aggregation method with 500 ensemble learning cycles, a learning rate for shrinkage of 0.3540 and at least 1 observation per leaf. It was found that the mean $R^2_{train} = 1.0000$ and $R^2_{test} = 0.7874$.

It was possible to find an analytical expression for this relationship with a very high model fit ($R^2 = 0.8454$). An exponential function of the form

$$z = f(\mu'_{s_{l_1}}, \mu'_{s_{l_2}}) = 1.251 \cdot \exp(-0.3319 \cdot \mu'_{s_{l_1}}) + 1.046 \cdot \exp(-0.6513 \cdot \mu'_{s_{l_2}}) + 0.1389 \tag{9}$$

could be fitted to the data. An interaction term of the both predictors was introduced to the equation by way of trial, but it did not lead to an improvement in the model fit and was therefore withdrawn. Graphically, this is illustrated

in figure 32b. It was also investigated to what extent this analytical function fits the test data described above. This resulted in $R^2 = 0.7958$.

These findings can be regarded as follows: When investigating the influence of the optical parameters on the slope β_1 of the regression line, in particular μ_s' of the two top skin layers (stratum corneum and epidermis) turned out to be extremely influential. The high model fit, which results when these

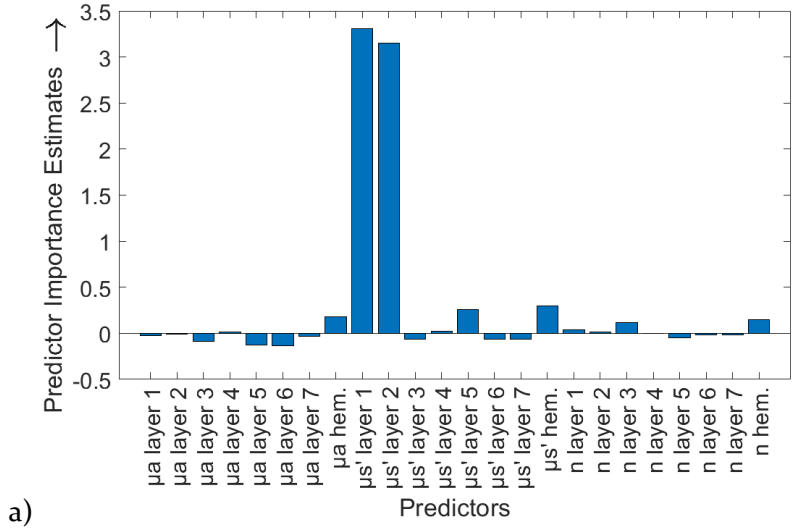

a)

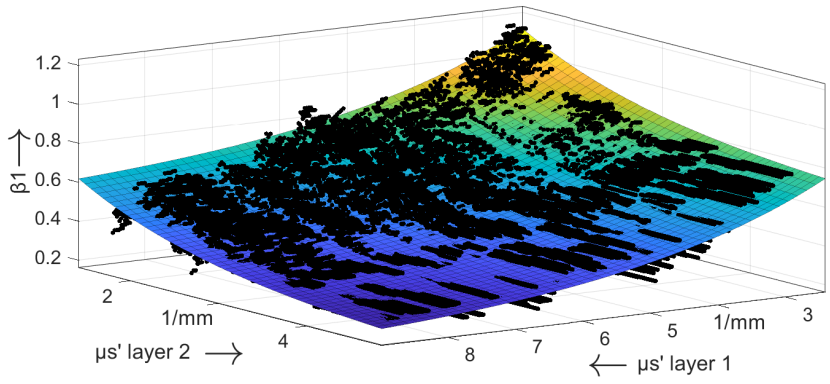

b)

Figure 32: (a) Out-of-bag permuted predictor importance of the 24 optical properties values when taken as prediction parameters for the response β_1 in a RF approach. (b) Graphical representation of data sets for μ_s' of the first two skin layers (dots) and the exponential function fitted thereto (plane). The equation is as follows: $z = 1.251 \cdot \exp(-0.3319 \cdot \mu_{s_{l1}}') + 1.046 \cdot \exp(-0.6513 \cdot \mu_{s_{l2}}') + 0.1389$. [P2]

parameters are used for the prediction of the response β_1, confirms this. The exponential relationship, which was demonstrated in the further analysis, allows an interpretation of this result: The stratum corneum is the outermost layer of the epidermis. This comparatively thin layer consists of dead corneocytes and functions as a barrier to protect underlying tissue [67]. In this manner, the stratum corneum exhibits high values for μ_s', especially when compared to the air surrounding the skin [68]. In comparison, the values for μ_s' of the epidermis are significantly lower; however, as the second outermost skin layer, the epidermis is still reached by a large proportion of photons, so that the influence of the epidermis can be explained in particular by its anatomical location.

From an optical point of view, these outermost skin layers thus serve as a boundary: On the one hand, photons emitted to the skin are reflected directly at or in these skin layers and thus do not or barely penetrate the skin. On the other hand, light that has been diffusely scattered in deeper skin layers and that is on its way back to the skin surface (i.e. to the detector) is reflected back into the skin mainly by the stratum corneum, but also by the epidermis. This relationship is exponential: With increasing values for μ_s' of the stratum corneum and the epidermis, the modulation of the SP-DRI signal and thus β_1 decrease. According to Beer's law, this behaviour is well in line with expectations.

For the mathematical investigation of the intercept parameter β_0, the procedure was similar to the one described before for the slope. The result on the importance of the predictors is not shown graphically due to its high similarity to figure 32a: The same two parameters proved to be the most important ones ($R^2_{oob} = 0.4391$). Accordingly, once more the μ_s' values of the first two skin layers have to be taken into account as predictors. With these two predictors, the automated optimization of the RF leads to 30 models (compare section 4.5) that use Bagging as ensemble aggregation method with 500 ensemble learning cycles and at least 3 observations per leaf. It was found that the mean $R^2_{train} = 0.6471$ and $R^2_{test} = 0.4421$.

Also in this case, the quest for an analytical expression had to take place in the three-dimensional space. With a model fit of $R^2 = 0.9117$, the equation

$$\begin{aligned} z = f(\mu_{s_{l1}}', \mu_{s_{l2}}') = &- 3.803 \cdot \exp(-0.4382 \cdot \mu_{s_{l1}}') \\ &- 2.356 \cdot \exp(-0.6406 \cdot \mu_{s_{l2}}') - 0.4093 \end{aligned} \tag{10}$$

describes the relationship. Again, the influence of both parameters is assumed to be exponential. A possible interaction term of the both predictors was considered, but again did not lead to an improvement in the model fit. It

was also investigated to what extent this analytical function fits the test data described above. This resulted in $R^2 = 0.4314$.

When predicting the intercept β_0, it is again μ_s' of stratum corneum and epidermis that seems to be most influential (the relationship is again exponential). In contrast to the prediction of β_1, a model fit (R^2_{test}) of only about 44% could be achieved. It seems to be difficult to fill the input parameter space in this particular multi-dimensional system in a meaningful way with data sets. Furthermore, it must be noted that a number of only 10^{10} photon packets were simulated per simulation run as described before. Compared to real measurements, the data is therefore subjected to a comparatively high level of noise. These two effects imply that a significantly better estimation of β_0 will be possible when further data sets are included or when measurements on the phantom or on tissues are performed.

As shown before, β_0 also depends on the distance between the illumination and the position of the capillary loop (and thus lastly also on the SDS as it determines the capillary observed). Since the presented model is to be understood as a proof of concept, the SDS has not been considered as a parameter so far. This is a to-do for the further development of the technique and will most likely result in an improvement of the model fit for β_0. In addition, the positions of the cross-sectional planes serving as the data basis for the K_{norm} algorithm are currently not yet adapted to the individual data sets, but they are always at $x = 570\ px$. An automated individual determination of the optimal positions would certainly result in a higher model fit of β_0 (and also β_1).

Note: The effect of varying optical properties is the most important effect that had to be studied. If SP-DRI would not work for different skin properties, there would be no practical application for this technology. Therefore, this was the first of the remaining outstanding questions to be assessed.

The observation that the stratum corneum together with the epidermis form an optical boundary layer that prevents photons from entering or leaving the tissue is a key finding that does not only affect SP-DRI, but is likely to impact many other optical measurement techniques that are applied directly to the surface of the skin. Pulse oximetry, for example, should be mentioned in this context. When developing future optical technologies, this fact also needs to be taken into account.

Based on these mathematical findings, it is now intended to predict the capillary diameter. As introduced in section 4.5, it is possible to predict the capillary diameter according to equation 7 using the parameters K_{norm}, β_0 and β_1 (note: as explained at the beginning of this section, a prior knowledge of

β_0 and β_1 is not possible in real-life measurements, hence predictions should be applied instead). There is, however, a certain prediction error inherent in this estimation. In the following, it is therefore investigated how large this error is if β_0 and β_1 are predicted based on the methods outlined above, namely RF and analytical model. For the methodological framework, please refer to (the last three paragraphs of) section 4.5.

A graphical representation of the results can be found in figure 33 in terms of boxplots. The numerical values in terms of means, medians and standard deviations as well as the CV over all data can be found in table 8.

Taking together all these findings, this study finally demonstrated that it is possible to predict the capillary diameter with a prediction error of about 14% (mean of the CV values given in table 8 for the analytical functions) based on SP-DRI and the K_{norm} value. This prediction performed best (taking into account the interquartile ranges and the outliers presented in the boxplots in figure 33 and the CV values given in table 8) when using the analytical functions that were fitted to the RF data with a high model fit, suggesting that there was a certain extent of overfitting with the RF approach - when fitting a function to this data predicted by RF, these kinds of local deviations will finally not be considered. Anyway, since the analytical approach is less computationally intensive, it is the preferable approach in the long run. A recourse to fixed values for β_0 and β_1, in contrast, was not expedient.

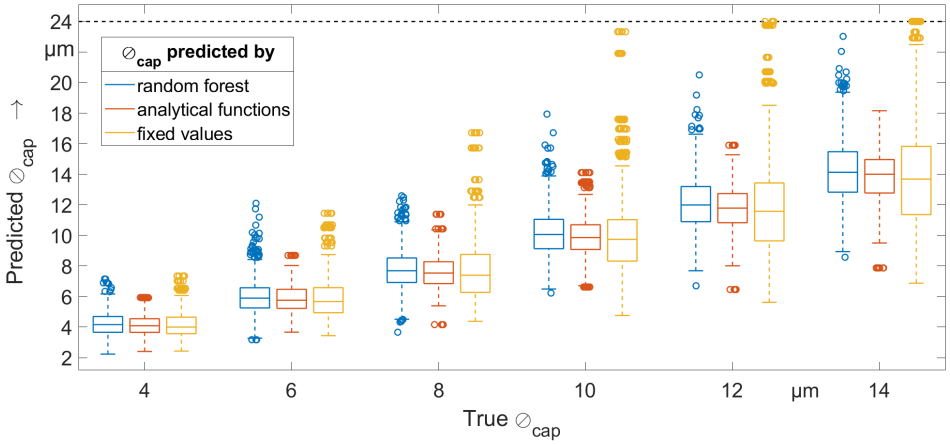

Figure 33: Graphical comparison of the predicted capillary diameters (y axis) and the simulated ground truth (x axis). Each boxplot shows the 25th and 75th percentiles as well as the median, and the whiskers' length is 1.5 times the interquartile range. For better visibility, the y axis is clipped at $y = 24$; predicted values outside this limit are displayed just on the limit. The numbers for the medians and standard deviations can also be found in table 8. [P2]

Table 8: Results from the prediction of the capillary diameters separated by the three prediction methods investigated. The mean and median values, standard deviations and coefficients of variation (CV) for all methods and capillary diameters are given. A graphical representation of this data can be found in figure 33. [P2]

β_0 and β_1 predicted by	indicator	true capillary diameter $\emptyset_{cap}$					
		4 µm	6 µm	8 µm	10 µm	12 µm	14 µm
RF	mean [µm]	4.1994	5.9730	7.7819	10.1648	12.0861	14.2164
	median [µm]	4.1610	5.8962	7.6886	10.0565	11.9937	14.1295
	SD [µm]	0.7432	1.1070	1.2600	1.5531	1.7469	2.0476
	CV [%]	17.70	18.53	16.19	15.28	14.45	14.40
analytical functions	mean [µm]	4.1135	5.8413	7.6192	9.9441	11.8261	13.8937
	median [µm]	4.0881	5.7570	7.5368	9.8589	11.7854	14.0022
	SD [µm]	0.6467	0.9277	1.1116	1.3585	1.5116	1.6697
	CV [%]	15.72	15.88	14.59	13.66	12.78	12.02
fixed values ($\lambda = 424$ nm)	mean [µm]	4.1389	5.8664	7.6770	10.0362	11.9414	14.0239
	median [µm]	4.0002	5.6755	7.3940	9.7414	11.5763	13.6836
	SD [µm]	0.8471	1.3854	1.9654	2.7246	3.3170	3.8964
	CV [%]	20.47	23.62	25.60	27.15	27.78	27.78

With this, and this is the important message from the present investigation, it is possible to measure not only relative changes in the capillary diameter (i.e. to translate a change ΔK_{norm} into a change $\Delta \emptyset_{\mathrm{cap}}$), but to perform an absolute quantification (i.e. assignment of an absolute capillary diameter d) if the depth of the capillaries is known. Thereby, the introduced prediction error is sufficiently small to allow a meaningful interpretation of the measured values. SP-DRI may then be used to reliably assess microcirculation and as an early alert system for the onset of associated diseases.

This raises the question: How can these findings be employed in practice? For the different sets of optical properties, the slopes β_1 and intercepts β_0 exhibit high standard deviations. This makes it nearly impossible (without the knowledge of the optical properties) to deduce the diameters of the capillaries from the measured K_{norm} values. The knowledge that these both responses are almost exclusively influenced by two parameters significantly improves this situation: If the influence of the stratum corneum and the epidermis can be estimated (or eliminated) when determining the parameters β_0 and β_1, their variation can be significantly reduced. For the stratum corneum, an elimination could be done, for example, by applying skin care cream or skin oil to the site of measurement or by locally scrubbing off this layer of dead cells. To estimate the influence of the epidermis, on the other hand, the tissue site could be illuminated at one spot and the extent of the resulting light cone could be used to automatically estimate μ_s' of the epidermis. Since SP-DRI inherently involves an illumination fibre and a camera chip, this step could be integrated into the method very easily.

In conclusion, it can thus be stated that the SP-DRI method works not only for discrete sets of optical properties, as shown so far, but also when the optical properties are altered randomly. This particularly includes also such cases which appear to be unfavourable at first sight: High scattering and absorption in the skin layers combined with low absorption of blood, to name one example. This conclusion underpins the potential of SP-DRI as it suggests that cross-individual operation is possible.

Note: To be able to investigate the influence of the different optical properties, the K_{norm} values for the various capillary diameters of a data set first had to be transformed into a pair of intercept β_0 and slope β_1 by means of a linear regression (preprocessing in the context of this study; for reasons of clarity, no further details on that are presented). In general, a very good model fit was found, resulting in excellent values for the coefficient of determination. This confirms that the linear relationship between the capillary diameter and K_{norm} which has already been described in section 5.8 is also present when the optical properties are randomly varied to a physiologically meaningful

extent. Thus, the importance of K_{norm} for the quantification of the SP-DRI signal could be proven once again.

5.11 Development of a dedicated SP-DRI sensor (ED)

In this section, the physical SP-DRI sensor - manufactured based on the key findings from the detailed simulative investigations presented so far - is evaluated. To assess - first of all - the resolution of this SP-DRI sensor, its modulation transfer function (MTF) was generated using a high resolution 1951 USAF resolution test chart. The resulting curve and the pertaining standard deviation (n=6) are shown in figure 34. As expected, the transmitted

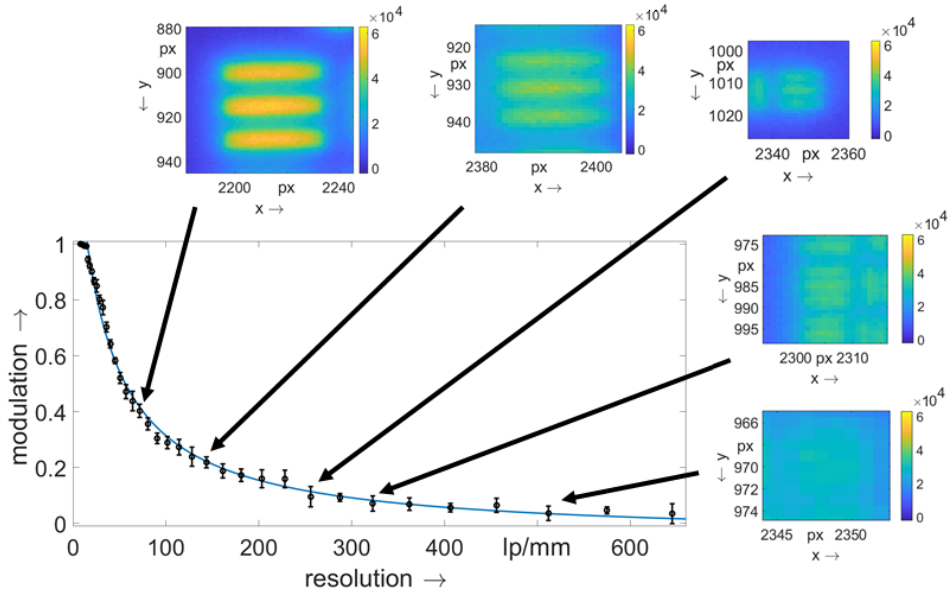

Figure 34: Modulation transfer function of the SP-DRI sensor with the standard deviation as error measure (n=6). To give an idea of the physical meaning of the numerical values, images of the high resolution 1951 USAF resolution test chart are provided as inlays at certain positions, namely at (from left to right) 71.8 lp/mm (6.96 µm line width), 143.7 lp/mm (3.48 µm line width), 256.0 lp/mm (1.95 µm line width), 322.5 lp/mm (1.55 µm line width) and 512.0 lp/mm (0.98 µm line width). The blue curve represents the rational function that was fitted to the measured data ($\bar{R}^2$=.9949). lp=line pair.

modulation m declines as the number of line pairs per mm d increases. With R^2=.9949, the rational function

$$m(d) = \frac{-0.05336d + 46.19}{d + 30.11} \tag{11}$$

describes this behaviour for $d \geq 14.25$ lp/mm (resolutions for which $d < 14.25$ lp/mm were not taken into account for the fit).

In general, no rigid cut-off value is defined as being the resolution of the system with regard to the MTF. There is, for instance, the concept of defining the first zero-crossing of the MTF curve as being the resolution of the system. In X-ray diagnostics, a drop in modulation to 2% is considered the cut-off resolution [121]. In the context of this dissertation, a more conservative value of 10% is to be applied. Following this, the SP-DRI sensor is capable of resolving a modulation of $d \approx 281.55$ lp/mm which corresponds to a line width of 1.78 µm. This value can be assumed to be the resolution of the SP-DRI sensor.

A resolution in this order of magnitude can be rated as excellent. With this, the SP-DRI sensor is able to provide a higher resolution than the comparative approaches mentioned in the state of the art section (compare section 2.3).

Except for a few modifications, the following part of this section is a reprint of my previously published article and taken from [P5].

At next, the results for the experimental investigations on the two optical PDMS phantoms are presented. The data for the phantom with a thread diameter of 10 µm will be described first; they are illustrated in figures 35 and 36. The reference image taken in transmitted light initially shows that there is indeed a thread structure in the imaging area covered by the SP-DRI sensor (figure 35a). The blurriness in the visualisation of the thread in the centre of this image indicates that the structure in this region is positioned deeper within the phantom than in the peripheral regions. Therefore, statements about variable structure depths can be made in the following.

Considering the exemplary diffuse reflectance raw data, the relatively strong light cone around the illumination LED is particularly notable (figure 35b). The thread structure is only partially perceivable. The two displayed cross-sectional planes along the x axis - one at a y position in the centre of the image and one at its periphery - illustrate this and prove that the thread texture is only weakly reflected in the diffuse reflectance raw data signal (figure 35c).

The SP-DRI algorithm was applied once along the x axis (illumination shift from LED #1 to LED #2; figure 36a) and once along the y axis (illumination shift from LED #4 to LED #5; figure 36b). As the thread in this example is fairly oriented along the y axis, the SP-DRI reconstruction with the shift perpendicular to this axis is particularly useful for detecting the thread structure. Once again, corresponding cross-sectional planes were prepared (at the same y positions as previously described for the raw data; figure 36c). From these, it can be deduced that the position of the thread structure can be clearly identified using SP-DRI: A significant deflection is evident in the SP-DRI signal, and its position is consistent with the position that is to be expected from the corresponding transmitted light reference image (shown in figure 35a).

For the optical phantom with a thread diameter of 20 µm, an analogous statement can be made. In this case, the thread appears in focus on the right-

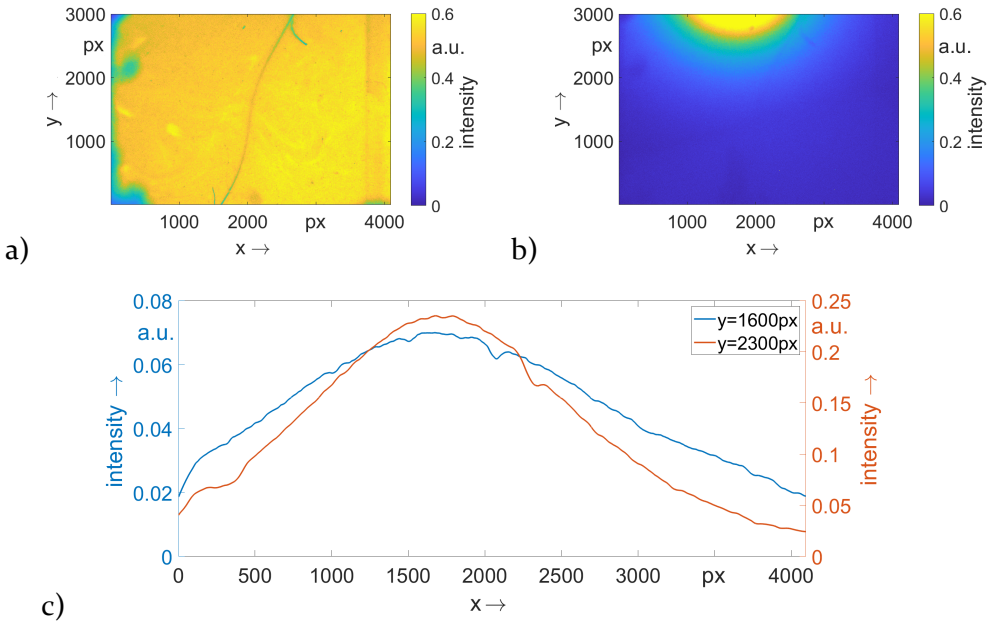

Figure 35: This figure shows the raw data results for the optical phantom for the configuration with a thread of 10 µm diameter. (a) Transmitted light image using a broadband light source; this image serves as reference for assessing the data reconstruction presented in the following sub-images. It can be seen that the thread runs vertically through the image, lying deeper in the centre of the image compared to the peripheral areas. (b) Exemplary diffuse reflectance raw data set when illuminating the optical phantom with LED #1. (c) Cross-sections along the x axis through the raw data map shown in (b) at the two y positions indicated by the legend. Note: The plots are scaled to 1. [P5]

hand side of the image, while its representation becomes considerably blurred in the centre and even more on the left-hand side of the image. The more pronounced blurring compared to the previous situation (compare figures 35a and 37a) indicates that the thread is already very deep within the phantom in the left part of the image. Again, the structure is only weakly visible in the raw data map (figure 37b) and in the corresponding cross-sectional planes (figure 37c), while the SP-DRI signal shows a clear deflection (figure 38c). Since the thread in this example is not primarily aligned along one image axis, but runs approximately diagonal thereto, both a matrix shift along the x axis (figure 38a) as well as a shift along the y axis (figure 38b) produce a clear signal.

Discussing these results, it can be stated first of all that the SP-DRI algorithm is functional in both phantom configurations: The position of the thread can be determined successfully both close to the phantom surface and deeper inside the phantom. SP-DRI is clearly superior to simply inspecting the raw data

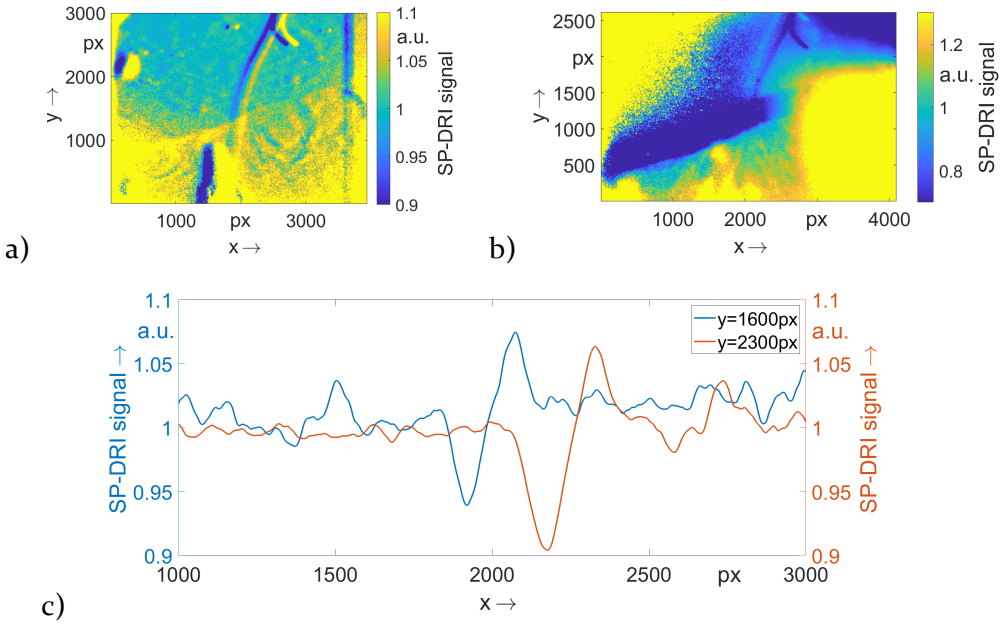

Figure 36: This figure shows the SP-DRI results for the optical phantom for the configuration with a thread of 10 µm diameter. (a) SP-DRI reconstruction based on the diffuse reflectance matrices for the illumination with LED #1 and LED #2 (the matrix shift is thus along the x axis). (b) SP-DRI reconstruction based on the diffuse reflectance matrices for the illumination with LED #4 and LED #5 (the matrix shift is thus along the y axis). (c) Cross-sections along the x axis through the SP-DRI map shown in (a) at the two y positions indicated by the legend. [P5]

images: Although slight changes in the diffuse reflectance curves may also be suspected in the case of the raw data, these changes are significantly weaker (in terms of percentages) than the SP-DRI signal deflections. In this respect, the experimental data confirm the findings about the general functionality of the algorithm which has been shown previously by MC simulations [P3]. This also highlights once again the superiority in the performance of SP-DRI over microvideoscopic approaches and techniques such as photoacoustic tomography, pulse oximetry or hyperspectral imaging, the disadvantages of which have already been described in detail in the state of the art chapter of this thesis. Other approaches based on diffuse reflection described in the literature also cannot match the performance of SP-DRI, in particular the lateral resolution achieved there is below that of SP-DRI; in some cases, imaging is possible only in transmission mode [55, 60, 62, 122].

Simulatively, it could also be shown that a larger capillary diameter results in a higher amplitude of the SP-DRI signal [P1]. To validate this finding experimentally, two different thread diameters were employed in the context of the present study. Looking at the cross-sectional planes through the SP-

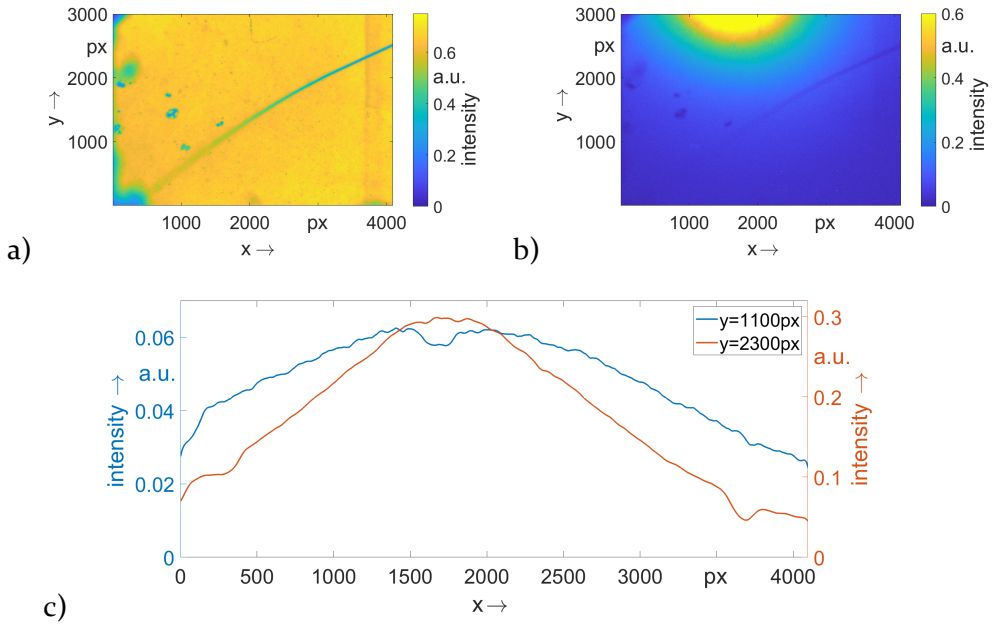

Figure 37: This figure shows the raw data results for the optical phantoms for the configuration with a thread of 20 µm diameter. As the single sub-illustrations are systematically corresponding to figure 35, their description can be looked up there accordingly. Note: The plots are scaled to 1. [P5]

DRI signal maps for the two regions where the thread is close to the phantom surface, it is evident that the signal generated by the 20 µm diameter threads is significantly stronger than that generated by the 10 µm diameter thread. Therefore, this simulative observation can be regarded as experimentally validated.

A comparison of the SP-DRI signals from the phantom regions where the thread is lying deeper also supports this conclusion: As already described before, it must be assumed that the thread with a diameter of 20 µm (in the examined image area) has sunk deeper into the phantom than the thread with a diameter of 10 µm. However, the corresponding SP-DRI curves show a quantitatively comparable deflection - as deeper structures also result in a lower amplitude [P4], the wire thickness must therefore have compensated for the wire depth, which is in line with expectations. Note: The future main application of SP-DRI will be the monitoring of alterations in the capillary diameter in long-term measurements. It is therefore uncritical that both capillary depth and diameter affect the SP-DRI signal.

In general, it can be stated that a functional SP-DRI sensor prototype was developed within the framework of the present study. The simulative in-

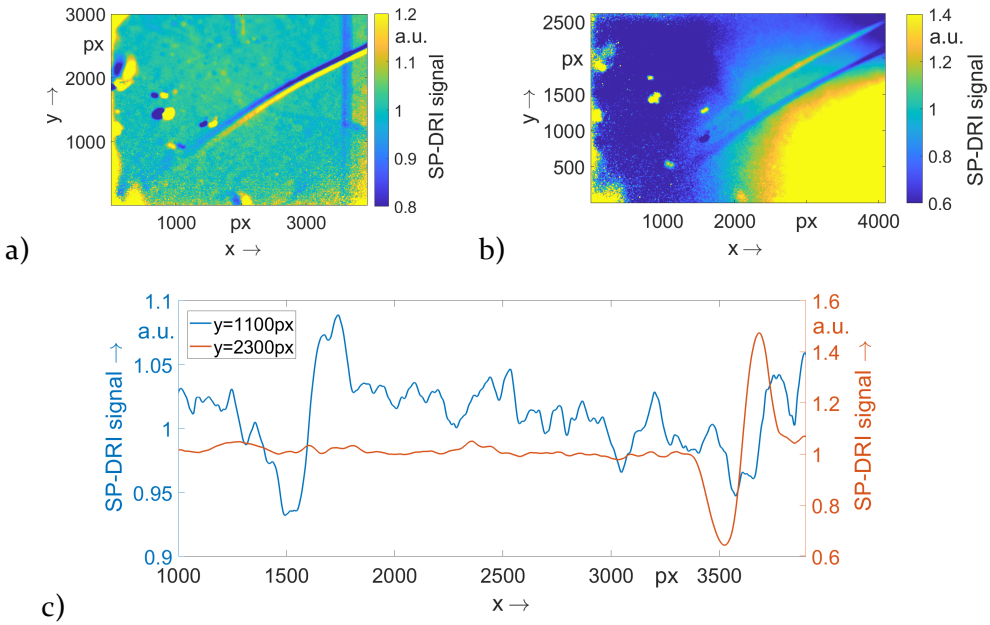

Figure 38: This figure shows the SP-DRI results for the optical phantoms for the configuration with a thread of 20 µm diameter. As the single sub-illustrations are systematically corresponding to figure 36, their description can be looked up there accordingly. [P5]

vestigations already mentioned formed the basis for the conceptual design of the sensor. Especially along the long side (x axis) of the imaging field, the linear arrangement of the LEDs as well as the adjustment of the image saturation worked well - it can be seen in figures 36a and 38a that the SP-DRI reconstruction is not superimposed by the intensity cone around the single LEDs. Along the short side (y axis), however, there is still room for improvement. Note: Although the raw data curves may exhibit a higher SNR than the SP-DRI data curves, the latter emphasise the thread structure far more effectively due to the excellent reduction of the background achievable with the SP-DRI algorithm.

The handling and assembly of the single optical fibres proved to be the most difficult part of the setup, and optimisations might still be possible. One simple option, for example, would be to procure and install pre-assembled fibre blocks. To miniaturise the setup, a fibre optic plate (FOP) could be used which is placed in direct contact with the camera chip on one side and the object under investigation on the other side. Unfortunately, this approach is accompanied by a reduction in lateral resolution.

It should be emphasised once again at this point that the presented measurements are initial validation results; in particular, the data processing steps were not yet automated. Nevertheless, SP-DRI was clearly functional. It is to be expected that more elaborate data processing techniques (including abandoning the assumption that the single LEDs are arranged perfectly collinear to the imaging field, i.e. rather taking into account both axes at a time when performing the matrix shift) would provide even better reconstruction results. The adjustment of the exposure could also be automated and the entire image area could be taken into account to enable a finer calibration. For the proof-of-concept sensor, however, attention was paid especially to the constructive aspect. Not least, the high lateral resolution achieved proves that the alignment of all components performed excellently.

In addition to further optimising the SP-DRI sensor, a next step is to apply the method *ex vivo*. The results of the present study are encouraging for a successful application of the presented diagnostic technique in this modality.

6 Summary and Outlook

"The progress of minimally and non-invasive medical techniques is driven not least by optical technologies with their inherent advantages [123]. One such method is diffuse reflectance imaging (DRI), which has already proven its suitability for medical imaging [80] - however, until now only relatively large structures have been imaged [124, 125]." [P3] The present doctoral thesis therefore aimed to investigate whether DRI can be scaled towards an observation of significantly smaller structures. In doing so, it could be demonstrated that human capillaries - typically having diameters of around 10 µm - are detectable when applying appropriate data processing routines to the diffuse reflection data. One such technique was developed and studied in detail in the course of this doctoral thesis: SP-DRI [P3].

"SP-DRI is quite easy to implement in practice: It only requires two illumination fibers (or one movable) placed directly next to each other, an alternating illumination of the tissue site and an approach for capturing the diffuse reflection - this can be done either directly with a microscope imaging approach or by extracting the diffuse reflection using detection fibers or by means of a CCD/CMOS chip (with suitably small pixels) placed directly on the surface of interest. If SP-DRI is implemented using the latter of the three approaches, a particular constructional strength of this method becomes apparent: The setup can be kept extremely small and no expensive optical components are required, not even lenses. This allows, on the one hand, a very cost-effective design and, on the other hand, no complex alignment of the setup is necessary." [P3]

Moreover: "Since the goal of SP-DRI is to detect spatial structures and (...) their alterations over the course of time (dilation or constriction) and not, as otherwise common in DRI, to extract optical properties from biological tissues, no time- and resource-intensive inverse algorithm is involved - data acquisition is thus possible in almost real time. (...) Due to the short exposure and calculation times, acquisition and processing are very robust against motion artifacts." [P3]

On account of the advantages mentioned so far, an extensive exploration and validation of SP-DRI has been carried out in the present doctoral thesis: The detectability of the vasculature structure was investigated both by MC simulations and in the experimental domain [P3]. In doing so, the main findings of this work can be summarised as follows:

- In general, the SP-DRI method was found to be highly promising: A well-defined visibility of the capillary structure could be achieved and the localization of the vasculature pattern matched the expected positions. The conducted basic functionality studies proved that SP-DRI provides an advantage over the plain raw data analysis and that it is specific and sensitive.
- SP-DRI has been shown to reliably derive information on the vasoconstriction and vasodilation of the microcirculatory vessels at anatomically realistic scales (a few micrometres). Promising results could be obtained, indicating not only that there is a correlation between the diameter of the capillary loops and the parameter used to quantify the SP-DRI signal, but also that this relationship is highly linear - allowing to deduce conclusions on the capillary diameter by processing the SP-DRI signal. [P1] It was thoroughly demonstrated that a variation in the optical properties of skin or haemoglobin does not constrain this feature [P2].
- With regard to the SP-DRI setup, it could be demonstrated that - as expected - the numerical aperture and the diameter of the illumination fibre as well as its shift influence the performance of the method. The same is true for the numerical aperture of the detection. As part of the present doctoral thesis, appropriate values for these parameters could be found in order to obtain an optimal SP-DRI signal.
- It could further be shown that the illumination wavelength used to generate the diffuse reflectance influences the magnitude of the SP-DRI signal. This is because the scattering and the absorption coefficient of the tissue under investigation are a function of this parameter. It was possible to identify an ideal illumination wavelength and to justify its choice from a physiological point of view.
- Also in practical laboratory experiments, the SP-DRI method was found to be functional. In a first setup, "the cantilever (from an AFM) used and modified in the sense of a capillary loop could be identified as such in the SP-DRI data, with the width and position of the structure represented in the data being in good agreement with the actual position within the optical phantom" [P3].
- In a second step, a physical SP-DRI sensor prototype was built and evaluated on even more realistic optical phantoms made from PDMS. To do so, again "phantoms with a sufficiently thin structure had to be made. Surgical thread with diameters of 10 µm and 20 µm was utilised for this purpose. Its black colour is highly absorbent, similar to haemoglobin at the selected illumination wavelength." [P5] This experiment further proved the previously simulated findings to be valid in a practical manner as well; besides, the built SP-DRI sensor prototype showed to be highly operational. The obtained resolution of 1.78 µm exceeds existing comparative approaches.

In conclusion, with SP-DRI a technique was developed to reliably obtain information from diffuse reflectance data "about the position of structures of the order of human capillaries within a turbid medium." [P3] "While it was pointed out in the introduction (...) that a crucial aspect of current clinical procedures for monitoring the state of the microcirculation is that these methods are invasive, leave scope for interpretation or only provide clues for making a diagnosis [10], this study was able to demonstrate that SP-DRI is an excellent approach to solving this issue: Reliable information can be obtained in real time with an easy to implement setup." [P1] SP-DRI "may be an important milestone on the way to early and conveniently diagnosing diseases associated with the constriction or dilation of the arterioles, venules or the capillary bed itself (microvascular dysfunctions, microangiopathies, microcirculation disorders). As already mentioned initially, this covers many diseases, among them diabetes mellitus, hypertension and autoimmune diseases [2]." [P1]

7 Zusammenfassung und Ausblick

Der Forschritt im Bereich minimal- und nicht-invasiver medizinischer Verfahren wird nicht zuletzt durch optische Technologien mit ihren immanenten Vorteilen getragen [123]. Eines dieser Verfahren ist die diffuse Reflexionsbildgebung (DRI), deren Eignung für die medizinische Bildgebung bereits nachgewiesen ist [80] - allerdings wurden bisher nur relativ große Strukturen bildlich erfasst [124, 125]. In der vorliegenden Dissertation sollte daher untersucht werden, ob eine Skalierung der DRI im Sinne einer Betrachtung deutlich kleinerer Strukturen möglich ist. Dabei konnte gezeigt werden, dass menschliche Kapillaren - mit Durchmessern von typischerweise 10 µm - detektierbar sind, wenn die Daten der diffusen Reflexion mithilfe geeigneter Datenverarbeitungsroutinen aufbereitet werden. Eine solche Technik wurde im Rahmen dieser Dissertation entwickelt und ausführlich untersucht: SP-DRI [P3].

SP-DRI ist in der Praxis sehr einfach zu implementieren: Es sind lediglich zwei unmittelbar nebeneinander angeordnete Beleuchtungsfasern (oder aber eine bewegliche Faser), eine serielle Beleuchtung der Gewebestelle und ein Ansatz zur Erfassung der diffusen Reflexion erforderlich - Letzterer kann analog zur Bildgebung bei einem Mikroskop durch Ableitung der diffusen Reflexion mittels Detektionsfasern oder durch direktes Auflegen eines CCD/CMOS-Chips (mit entsprechend kleinen Pixeln) auf die zu untersuchende Oberfläche realisiert werden. Wird SP-DRI auf der Basis des letztgenannten Konzepts implementiert, zeigt sich eine besondere konstruktive Stärke dieser Methode: Der Aufbau kann äußerst kompakt und ohne teure optische Komponenten ausgeführt werden, selbst Linsen werden dann nicht benötigt. Dies ermöglicht eine sehr kostengünstige Konstruktion, die keine aufwendige Justierung des Aufbaus voraussetzt.

Darüber hinaus: Da es das Ziel von SP-DRI ist, räumliche Strukturen und deren Veränderungen im zeitlichen Verlauf zu erfassen (Dilatation oder Konstriktion) und nicht, wie sonst in der DRI üblich, die optischen Eigenschaften biologischen Gewebes zu bestimmen, ist kein zeit- und ressourcenintensiver inverser Algorithmus erforderlich - die Datenerfassung ist somit nahezu in Echtzeit möglich. Aufgrund der kurzen Belichtungs- und Berechnungszeiten sind Aufnahme und Verarbeitung sehr robust hinsichtlich Bewegungsartefakten [P3].

Aufgrund der bisher dargestellten Vorteile wurde in der vorliegenden Dissertation eine umfassende Erforschung und Validierung von SP-DRI durchgeführt: Die Detektierbarkeit der Gefäßstruktur wurde sowohl durch MC-

Simulationen als auch experimentell untersucht [P3]. Dabei lassen sich die wesentlichen Erkenntnisse dieser Arbeit wie folgt zusammenfassen:

- Die SP-DRI-Methode erwies sich im Allgemeinen als sehr vielversprechend: Die kapillaren Strukturen konnten präzise sichtbar gemacht werden und die Lage der Gefäße entsprach den erwarteten Positionen. Grundlegende Funktionalitätsstudien zeigten, dass SP-DRI einen Vorteil gegenüber der reinen Rohdatenanalyse bietet und dass die Methode spezifisch und sensitiv ist.
- Es konnte dargelegt werden, dass mittels SP-DRI eine zuverlässige Ableitung von Informationen über die Vasokonstriktion bzw. Vasodilatation der Mikrozirkulationsgefäße in anatomisch realistischen Größenordnungen (wenige Mikrometer) möglich ist. Hier wurden vielversprechende Ergebnisse erzielt, die nicht nur darauf hindeuten, dass es eine Korrelation zwischen dem Durchmesser der Kapillarbögen und dem zur Quantifizierung des SP-DRI-Signals verwendeten Parameter gibt, sondern auch, dass diese Beziehung nahezu linear ist - was es ermöglicht, durch die Auswertung des SP-DRI-Signals Rückschlüsse auf den Kapillardurchmesser zu ziehen [P1]. Dass eine Variation der optischen Eigenschaften von Haut oder Hämoglobin diese Tatsache nicht einschränkt, wurde ausführlich aufgezeigt [P2].
- Im Hinblick auf den SP-DRI-Aufbau konnte - wie erwartet - nachgewiesen werden, dass die numerische Apertur und der Durchmesser der Beleuchtungsfaser sowie deren Verschiebung die Leistungsfähigkeit der Methode beeinflussen. Das Gleiche gilt für die numerische Apertur der Detektion. Im Rahmen der vorliegenden Dissertation wurden für diese Parameter geeignete Werte gefunden, um ein optimales SP-DRI-Signal zu erzielen.
- Ferner wurde dargelegt, dass die zur Erzeugung der diffusen Reflexion verwendete Beleuchtungswellenlänge die Stärke des SP-DRI-Signals beeinflusst. Dies liegt daran, dass der Streuungs- und der Absorptionskoeffizient des untersuchten Gewebes eine Funktion dieses Parameters sind. Es konnte eine ideale Beleuchtungswellenlänge ermittelt und deren Wahl unter physiologischen Gesichtspunkten begründet werden.
- Auch in den Laborexperimenten erwies sich die SP-DRI-Methode als funktionsfähig. In einem ersten Aufbau konnte die verwendete und im Sinne eines Kapillarbogens modifizierte Messnadel (*Cantilever* aus einem Rasterkraftmikroskop) in den SP-DRI-Daten als solche erkannt werden, wobei die Breite und die Position der detektierten Struktur gut mit der tatsächlichen Position innerhalb des optischen Phantoms übereinstimmten [P3].
- In einem zweiten Ansatz wurde ein physischer SP-DRI-Sensor-Prototyp gebaut und an nochmals verbesserten optischen Phantomen aus PDMS erprobt. Dazu mussten erneut Phantome mit einer ausreichend dünnen Struktur hergestellt werden. Zu diesem Zweck wurden chirurgische Fäden

mit Durchmessern von 10 µm und 20 µm verwendet. Deren schwarze Farbe ist stark absorbierend, vergleichbar mit Hämoglobin bei der gewählten Beleuchtungswellenlänge [P5]. Anhand dieses Experiments konnten die vorab simulierten Erkenntnisse auch praktisch bestätigt werden; außerdem erwies sich der entwickelte Prototyp des SP-DRI-Sensors als voll funktionsfähig. Die erzielte Auflösung von 1,78 µm übertrifft existierende vergleichbare Ansätze.

Zusammenfassend gilt somit, dass mit SP-DRI eine Technik entwickelt wurde, die es ermöglicht, aus den Daten der diffusen Reflexion auf verlässliche Weise Informationen über die Lage von Strukturen in der Größenordnung menschlicher Kapillaren in einem trüben Medium zu gewinnen [P3]. In der Einleitung wurde darauf hingewiesen, dass gegenwärtige klinische Verfahren zur Überwachung des Zustands der Mikrozirkulation den entscheidenden Nachteil haben, dass sie invasiv sind, Interpretationsspielraum zulassen oder lediglich Anhaltspunkte für eine Diagnose liefern [10]; die vorliegende Studie konnte nun zeigen, dass SP-DRI ein idealer Ansatz zur Lösung dieses Problems ist: Zuverlässige Informationen können in Echtzeit mit einer einfach zu implementierenden Apparatur gewonnen werden. SP-DRI kann ein wichtiger Meilenstein auf dem Weg zur frühzeitigen und einfachen Diagnose von Krankheiten sein, die mit der Konstriktion oder Dilatation von Arteriolen, Venolen oder dem Kapillarbett selbst einhergehen (mikrovaskuläre Dysfunktionen, Mikroangiopathien, Mikrozirkulationsstörungen). Wie eingangs erläutert, umfasst dies zahlreiche Krankheiten, darunter Diabetes mellitus, Bluthochdruck und Autoimmunerkrankungen [2, P1].

Bibliography

[1] Jacob, Matthias; Chappell, Daniel, and Becker, Bernhard F. "Regulation of blood flow and volume exchange across the microcirculation". *Critical care (London, England)* 20.1 (2016), p. 319.

[2] Gutterman, David D.; Chabowski, Dawid S.; Kadlec, Andrew O.; Durand, Matthew J.; Freed, Julie K.; Ait-Aissa, Karima, and Beyer, Andreas M. "The Human Microcirculation: Regulation of Flow and Beyond". *Circulation research* 118.1 (2016), pp. 157–172.

[3] Hainsworth, R. "Vascular capacitance: its control and importance". *Reviews of physiology, biochemistry and pharmacology* 105 (1986), pp. 101–173.

[4] Peters, J.; Mack, G. W., and Lister, G. "The importance of the peripheral circulation in critical illnesses". *Intensive care medicine* 27.9 (2001), pp. 1446–1458.

[5] Baskett, P. J. "ABC of major trauma. Management of hypovolaemic shock". *BMJ (Clinical research ed.)* 300.6737 (1990), pp. 1453–1457.

[6] Haljamäe, Hengo. "Microcirculation and hemorrhagic shock". *The American journal of emergency medicine* 2.1 (1984), pp. 100–107.

[7] Lima, Alexandre and Bakker, Jan. "Clinical assessment of peripheral circulation". *Current opinion in critical care* 21.3 (2015), pp. 226–231.

[8] Cervenka, Brian and Bewley, Arnaud F. "Free flap monitoring: a review of the recent literature". *Current opinion in otolaryngology & head and neck surgery* 23.5 (2015), pp. 393–398.

[9] Drucker, W. R.; Chadwick, C. D., and Gann, D. S. "Transcapillary refill in hemorrhage and shock". *Archives of surgery (Chicago, Ill. : 1960)* 116.10 (1981), pp. 1344–1353.

[10] Bajwa, Ednan K.; Malhotra, Atul, and Thompson, B. Taylor. "Methods of monitoring shock". *Seminars in respiratory and critical care medicine* 25.6 (2004), pp. 629–644.

[11] Backer, Daniel de; Ospina-Tascon, Gustavo; Salgado, Diamantino; Favory, Raphaël; Creteur, Jacques, and Vincent, Jean-Louis. "Monitoring the microcirculation in the critically ill patient: current methods and future approaches". *Intensive care medicine* 36.11 (2010), pp. 1813–1825.

[12] Herold, Gerd. *Innere Medizin 2014: Eine vorlesungsorientierte Darstellung; unter Berücksichtigung des Gegenstandskataloges für die Ärztliche Prüfung; mit ICD 10-Schlüssel im Text und Stichwortverzeichnis*. Köln: Selbstverl., 2014.

[13] Cohn, Stephen M.; Nathens, Avery B.; Moore, Frederick A.; Rhee, Peter; Puyana, Juan Carlos; Moore, Ernest E., and Beilman, Gregory J. "Tissue oxygen saturation predicts the development of organ dysfunction during traumatic shock resuscitation". *The Journal of trauma* 62.1 (2007), 44–54, discussion 54–5.

[14] Schießler, C.; Schaudig, S.; Harris, A. G., and Christ, F. ""Orthogonal polarization spectral imaging": Eine neue klinische Methode für das Monitoring der Mikrozirkulation". *Der Anaesthesist* 51.7 (2002), pp. 576–579.

[15] Nolte, D.; Zeintl, H.; Steinbauer, M.; Pickelmann, S., and Messmer, K. "Functional capillary density: an indicator of tissue perfusion?" *International journal of microcirculation, clinical and experimental* 15.5 (1995), pp. 244–249.

[16] Eriksson, Sam; Nilsson, Jan, and Sturesson, Christian. "Non-invasive imaging of microcirculation: a technology review". *Medical devices (Auckland, N.Z.)* 7 (2014), pp. 445–452.

[17] Roustit, Matthieu and Cracowski, Jean-Luc. "Assessment of endothelial and neurovascular function in human skin microcirculation". *Trends in pharmacological sciences* 34.7 (2013), pp. 373–384.

[18] Cracowski, Jean-Luc and Roustit, Matthieu. "Current Methods to Assess Human Cutaneous Blood Flow: An Updated Focus on Laser-Based-Techniques". *Microcirculation* 23.5 (2016), pp. 337–344.

[19] Ocak, Işık; Kara, Atila, and Ince, Can. "Monitoring microcirculation". *Best practice & research. Clinical anaesthesiology* 30.4 (2016), pp. 407–418.

[20] Roustit, Matthieu and Cracowski, Jean-Luc. "Non-invasive assessment of skin microvascular function in humans: an insight into methods". *Microcirculation* 19.1 (2012), pp. 47–64.

[21] Dubin, Arnaldo; Kanoore Edul, Vanina Siham; Caminos Eguillor, Juan Francisco, and Ferrara, Gonzalo. "Monitoring Microcirculation: Utility and Barriers - A Point-of-View Review". *Vascular health and risk management* 16 (2020), pp. 577–589.

[22] Altintas, Mehmet Ali; Altintas, A. A.; Guggenheim, M.; Steiert, A. E.; Aust, M. C.; Niederbichler, A. D.; Herold, C., and Vogt, P. M. "Insight in human skin microcirculation using in vivo reflectance-mode confocal laser scanning microscopy". *Journal of digital imaging* 23.4 (2010), pp. 475–481.

[23] Aykut, Guclu; Veenstra, Gerke; Scorcella, Claudia; Ince, Can, and Boerma, Christiaan. "Cytocam-IDF (incident dark field illumination) imaging for bedside monitoring of the microcirculation". *Intensive care medicine experimental* 3.1 (2015), p. 40.

[24] Briers, J. D. "Laser Doppler, speckle and related techniques for blood perfusion mapping and imaging". *Physiological measurement* 22.4 (2001), R35–66.

[25] Allen, John and Howell, Kevin. "Microvascular imaging: techniques and opportunities for clinical physiological measurements". *Physiological measurement* 35.7 (2014), R91–R141.

[26] Daly, Susan M. and Leahy, Martin J. "'Go with the flow ': a review of methods and advancements in blood flow imaging". *Journal of biophotonics* 6.3 (2013), pp. 217–255.

[27] , bowen li bowen; Tan, Shiyu; Dong, Jiuyang; Lian, Xiaocong; yongbing zhang yongbing; xiangyang ji xiangyang, and Veeraraghavan, Ashok. "Deep-3D Microscope: 3D volumetric microscopy of thick scattering samples using a wide-field microscope and machine learning". *Biomedical optics express* 13.1 (2021), pp. 284–299.

[28] Lima, Alexandre. "Current status of tissue monitoring in the management of shock". *Current opinion in critical care* 22.3 (2016), pp. 274–278.

[29] Moore, Frederick A.; McKinley, Bruce A., and Moore, Ernest E. "The next generation in shock resuscitation". *The Lancet* 363.9425 (2004), pp. 1988–1996.

[30] Creteur, Jacques. "Muscle StO2 in critically ill patients". *Current opinion in critical care* 14.3 (2008), pp. 361–366.

[31] Hu, Song and Wang, Lihong V. "Photoacoustic Tomography of Microcirculation". *Microcirculation Imaging*. Ed. by Leahy, Martin J. Weinheim, Germany: Wiley-VCH Verlag GmbH & Co. KGaA, 2012, pp. 259–278.

[32] Dalen, James E. "Is It Time to Pull the Pulmonary Artery Catheter?" *JAMA: The Journal of the American Medical Association* 276.11 (1996), p. 916.

[33] Jenkins, Amanda Suzanne. "Characterizing monitoring for the diagnosis and resuscitation of shock patients". Master's Thesis. Massachusetts: Massachusetts Institute of Technology, 2008. http://hdl.handle.net/1721.1/43810.

[34] Lima, Alexandre and Bakker, Jan. "Noninvasive monitoring of peripheral perfusion". *Intensive care medicine* 31.10 (2005), pp. 1316–1326.

[35] Otero, Ronny and Garcia, A. Joseph. "Clinical review: New technologies – venturing out of the intensive care unit". *Critical care (London, England)* 9.3 (2005), pp. 296–302.

[36] Boerma, E. Christiaan; Kuiper, Michael A.; Kingma, W. Peter; Egbers, Peter H.; Gerritsen, Rik T., and Ince, Can. "Disparity between skin perfusion and sublingual microcirculatory alterations in severe sepsis and septic shock: A prospective observational study". *Intensive care medicine* 34.7 (2008), pp. 1294–1298.

[37] DeMeulenaere, Susan. "Pulse Oximetry: Uses and Limitations". *The Journal for Nurse Practitioners* 3.5 (2007), pp. 312–317.

[38] Holmer, Amadeus; Marotz, Jörg; Wahl, Philip; Dau, Michael, and Kämmerer, Peer W. "Hyperspectral imaging in perfusion and wound diagnostics - methods and algorithms for the determination of tissue parameters". *Biomedical engineering* 63.5 (2018), pp. 547–556.

[39] Dietrich, M.; Marx, S.; Forst, M. von der; Bruckner, T.; Schmitt, F. C. F.; Fiedler, M. O.; Nickel, F.; Studier-Fischer, A.; Müller-Stich, B. P.; Hackert, T.; Brenner, T.; Weigand, M. A.; Uhle, F., and Schmidt, K. "Bedside hyperspectral imaging indicates a microcirculatory sepsis pattern - an observational study". *Microvascular research* 136 (2021), p. 104164.

[40] Lu, Guolan and Fei, Baowei. "Medical hyperspectral imaging: a review". *Journal of biomedical optics* 19.1 (2014), p. 10901.

[41] Backer, Daniel de; Donadello, Katia; Taccone, Fabio Silvio; Ospina-Tascon, Gustavo; Salgado, Diamantino, and Vincent, Jean-Louis. "Microcirculatory alterations: potential mechanisms and implications for therapy". *Annals of intensive care* 1.1 (2011), p. 27.

[42] Mazzoni, M. C.; Borgström, P.; Intaglietta, M., and Arfors, K. E. "Lumenal narrowing and endothelial cell swelling in skeletal muscle capillaries during hemorrhagic shock". *Circulatory shock* 29.1 (1989), pp. 27–39.

[43] Mazzoni, M. C.; Borgström, P.; Intaglietta, M., and Arfors, K. E. "Capillary narrowing in hemorrhagic shock is rectified by hyperosmotic saline-dextran reinfusion". *Circulatory shock* 31.4 (1990), pp. 407–418.

[44] Bosman, J.; Tangelder, G. J.; Oude Egbrink, M. G.; Reneman, R. S., and Slaaf, D. W. "Capillary diameter changes during low perfusion pressure and reactive hyperemia in rabbit skeletal muscle". *American Journal of Physiology-Legacy Content* 269.3 Pt 2 (1995), H1048–55.

[45] Slaaf, D. W.; Tangelder, G. J.; Teirlinck, H. C.; Oude Vrielink, H. H., and Reneman, R. S. "Flow cessation pressures in the rabbit tenuissimus muscle". *International journal of microcirculation, clinical and experimental* 5.1 (1986), pp. 3–9.

[46] Hall, Catherine N.; Reynell, Clare; Gesslein, Bodil; Hamilton, Nicola B.; Mishra, Anusha; Sutherland, Brad A.; O'Farrell, Fergus M.; Buchan, Alastair M.; Lauritzen, Martin, and Attwell, David. "Capillary pericytes regulate cerebral blood flow in health and disease". *Nature* 508.7494 (2014), pp. 55–60.

[47] Kusza, Krzysztof and Siemionow, Maria. "Is the knowledge on tissue microcirculation important for microsurgeon?" *Microsurgery* 31.7 (2011), pp. 572–579.

[48] Wilson, R. H. and Mycek, M-A. "Models of light propagation in human tissue applied to cancer diagnostics". *Technology in cancer research & treatment* 10.2 (2011), pp. 121–134.

[49] Rajaram, Narasimhan; Gopal, Ashwini; Zhang, Xiaojing, and Tunnell, James W. "Experimental validation of the effects of microvasculature pigment packaging on in vivo diffuse reflectance spectroscopy". *Lasers in surgery and medicine* 42.7 (2010), pp. 680–688.

[50] Lister, Tom; Wright, Philip A., and Chappell, Paul H. "Optical properties of human skin". *Journal of biomedical optics* 17.9 (2012), pp. 90901–1.

[51] Sorgato, Veronica; Berger, Michel; Emain, Charlotte; Vever-Bizet, Christine; Dinten, Jean-Marc; Bourg-Heckly, Geneviève, and Planat-Chrétien, Anne. "ACA-Pro: Calibration protocol for quantitative diffuse reflectance spectroscopy. Validation on contact and noncontact probe- and CCD-based systems". *Journal of biomedical optics* 21.6 (2016), p. 65003.

[52] Koenig, Anne; Grande, Sophie; Dahel, Karima; Planat-Chrétien, Anne; Poher, Vincent; Goujon, Catherine, and Dinten, Jean-Marc. "Diffuse reflectance spectroscopy: A clinical study of tuberculin skin tests reading". Ed. by Wax, Adam P. and Backman, Vadim. SPIE Proceedings. SPIE, 2013, 85920S.

[53] Kollias, Nikiforos and Stamatas, Georgios N. "Optical non-invasive approaches to diagnosis of skin diseases". *The journal of investigative dermatology. Symposium proceedings* 7.1 (2002), pp. 64–75.

[54] Zonios, George and Dimou, Aikaterini. "Modeling diffuse reflectance from semi-infinite turbid media: Application to the study of skin optical properties". *Optics Express* 14.19 (2006), p. 8661.

[55] Doornbos, Richard; Lang, Robert; Aalders, Maurice; Cross, Frank, and Sterenborg, Henricus. "The determination of in vivo human tissue optical properties and absolute chromophore concentrations using spatially resolved steady-state diffuse reflectance spectroscopy". *Physics in Medicine and Biology* 44.4 (1999), pp. 967–981.

[56] Bykov, Alexander V.; Priezzhev, Alexander V., and Myllyla, Risto. "Spatial resolved diffuse reflection as a tool for determination of size and embedding depth of blood vessels". *Diffuse Optical Imaging of Tissue*. Ed. by Pogue, Brian W. and Cubeddu, Rinaldo. SPIE Proceedings. SPIE, 2007, 66291P.

[57] Kanawade, Rajesh; Sayko, Gennadi; Schmidt, Michael, and Douplik, Alexandre. "In vivo monitoring of vessel density pattern in skin phantoms for the application of early sign of shock detection by using diffuse reflectance spectroscopy". Ed. by Mahadevan-Jansen, Anita; Vo-Dinh, Tuan, and Grundfest, Warren S. SPIE Proceedings. SPIE, 2011, p. 789009.

[58] Kanawade, Rajesh; Klämpfl, Florian; Riemann, Max; Knipfer, Christian; Tangermann-Gerk, Katja; Schmidt, Michael, and Stelzle, Florian. "Novel method for early signs of clinical shock detection by monitoring blood capillary/vessel spatial pattern". *Journal of biophotonics* 7.10 (2014), pp. 841–849.

[59] Kanawade, Rajesh. *In-vivo monitoring of epithelium vessel and capillary density for the application of detection of clinical shock and early signs of cancer development*. Vol. Bd. 239. Fertigungstechnik - Erlangen. Bamberg: Meisenbach, 2013.

[60] Schelkanova, Irina; Pandya, Aditya; Saiko, Guennadi; Nacy, Lidia; Babar, Hannan; Shah, Duoaud; Lilge, Lothar, and Douplik, Alexandre. "Spatially resolved, diffuse reflectance imaging for subsurface pattern visualization toward development of a lensless imaging platform: Phantom experiments". *Journal of biomedical optics* 21.1 (2016), p. 15004.

[61] Petitdidier, Nils; Koenig, Anne; Gerbelot, Rémi; Grateau, Henri; Gioux, Sylvain, and Jallon, Pierre. "Contact, high-resolution spatial diffuse reflectance imaging system for skin condition diagnosis". *Journal of biomedical optics* 23.11 (2018), pp. 1–9.

[62] Schelkanova, I.; Pandya, A.; Shah, D.; Lilge, L., and Douplik, A. "Diffuse reflectance measurements using lensless CMOS imaging chip". *Journal of Physics: Conference Series* 541 (2014), p. 012098.

[63] Gebrekidan, Medhanie Tesfay; Knipfer, Christian; Stelzle, Florian; Popp, Juergen; Will, Stefan, and Braeuer, Andreas. "A shifted-excitation Raman difference spectroscopy (SERDS) evaluation strategy for the efficient isolation of Raman spectra from extreme fluorescence interference". *Journal of Raman Spectroscopy* 47.2 (2016), pp. 198–209.

[64] Clamosa, Fama and Häggström, Mikael. *Wikimedia Commons: Epidermis delimited*. 2010. https://commons.wikimedia.org/wiki/File:Epidermis-delimited.JPG.

[65] Cevc, Gregor and Vierl, Ulrich. "Spatial distribution of cutaneous microvasculature and local drug clearance after drug application on the skin". *Journal of controlled release: official journal of the Controlled Release Society* 118.1 (2007), pp. 18–26.

[66] Bashkatov, Alexey; Genina, Elina; Kochubey, Vyacheslav, and Tuchin, Valery. "Optical properties of human skin, subcutaneous and mucous tissues in the wavelength range from 400 to 2000 nm". *Journal of Physics D: Applied Physics* 38.15 (2005), pp. 2543–2555.

[67] Elias, Peter M. "Stratum corneum defensive functions: an integrated view". *The Journal of investigative dermatology* 125.2 (2005), pp. 183–200.

[68] Bashkatov, Alexey N.; Genina, Elina A., and Tuchin, Valery V. "OPTICAL PROPERTIES OF SKIN, SUBCUTANEOUS, AND MUSCLE TISSUES: A REVIEW". *Journal of Innovative Optical Health Sciences* 04.01 (2011), pp. 9–38.

[69] Meglinski, Igor and Doronin, Alexander. "Monte Carlo Modeling of Photon Migration for the Needs of Biomedical Optics and Biophotonics". *Advanced Biophotonics*. Ed. by Wang, Ruikang K. and Tuchin, Valery. Vol. 20133183. Series in Optics and Optoelectronics. Taylor & Francis, 2013, pp. 1–72.

[70] Fritsch, Peter and Schwarz, Thomas. *Dermatologie Venerologie*. Berlin, Heidelberg: Springer Berlin Heidelberg, 2018.

[71] Braverman, Irwin M. "The Cutaneous Microcirculation: Ultrastructure and Microanatomical Organization". *Microcirculation* 4.3 (1997), pp. 329–340.

[72] Etehad Tavakol, Mahnaz; Fatemi, Alimohammad; Karbalaie, Abdolamir; Emrani, Zahra, and Erlandsson, Björn-Erik. "Nailfold Capillaroscopy in Rheumatic Diseases: Which Parameters Should Be Evaluated?" *BioMed research international* 2015 (2015), p. 974530.

[73] Prahl, Scott A. *Tabulated Molar Extinction Coefficient for Hemoglobin in Water*. 1998. https://omlc.org/spectra/hemoglobin/summary.html.

[74] Meinke, Martina; Müller, Gerhard; Helfmann, Jürgen, and Friebel, Moritz. "Optical properties of platelets and blood plasma and their influence on the optical behavior of whole blood in the visible to near infrared wavelength range". *Journal of biomedical optics* 12.1 (2007), p. 014024.

[75] Bosschaart, Nienke; Edelman, Gerda J.; Aalders, Maurice C. G.; van Leeuwen, Ton G., and Faber, Dirk J. "A literature review and novel theoretical approach on the optical properties of whole blood". *Lasers in medical science* 29.2 (2014), pp. 453–479.

[76] Prahl, Scott A. *Optical Absorption of Hemoglobin*. 1999. https://omlc.org/spectra/hemoglobin/.

[77] Niemz, Markolf H. *Laser-Tissue Interactions: Fundamentals and Applications*. Third, Enlarged Edition. Biological and Medical Physics, Biomedical Engineering. Berlin, Heidelberg: Springer-Verlag Berlin Heidelberg, 2007. http://dx.doi.org/10.1007/978-3-540-72192-5.

[78] Bydlon, Torre M.; Nachabé, Rami; Ramanujam, Nimmi; Sterenborg, Henricus J. C. M., and Hendriks, Benno H. W. "Chromophore based analyses of steady-state diffuse reflectance spectroscopy: Current status and perspectives for clinical adoption". *Journal of biophotonics* 8.1-2 (2015), pp. 9–24.

[79] Reif, Roberto; A'Amar, Ousama, and Bigio, Irving J. "Analytical model of light reflectance for extraction of the optical properties in small volumes of turbid media". *Applied Optics* 46.29 (2007), p. 7317.

[80] Utzinger, Urs and Richards-Kortum, Rebecca R. "Fiber optic probes for biomedical optical spectroscopy". *Journal of biomedical optics* 8.1 (2003), pp. 121–147.

[81] Zonios, George; Bassukas, Ioannis, and Dimou, Aikaterini. "Comparative evaluation of two simple diffuse reflectance models for biological tissue applications". *Applied Optics* 47.27 (2008), p. 4965.

[82] Periyasamy, Vijitha and Pramanik, Manojit. "Advances in Monte Carlo Simulation for Light Propagation in Tissue". *IEEE reviews in biomedical engineering* 10 (2017), pp. 122–135.

[83] Jacques, Steven L. "Monte Carlo Modeling of Light Transport in Tissue (Steady State and Time of Flight)". *Optical-Thermal Response of Laser-Irradiated Tissue*. Ed. by Welch, Ashley J. and van Gemert, Martin J.C. Dordrecht: Springer Netherlands, 2011, pp. 109–144.

[84] Wang, Lihong; Jacques, Steven L., and Zheng, Liqiong. "MCML—Monte Carlo modeling of light transport in multi-layered tissues". *Computer Methods and Programs in Biomedicine* 47.2 (1995), pp. 131–146.

[85] Fang, Qianqian and Boas, David A. "Monte Carlo simulation of photon migration in 3D turbid media accelerated by graphics processing units". *Optics express* 17.22 (2009), pp. 20178–20190.

[86] Jacques, Steven; Li, Ting, and Prahl, Scott. *mcxyz.c, a 3D Monte Carlo simulation of heterogeneous tissues*. 2019. https://omlc.org/software/mc/mcxyz/index.html.

[87] Boas, David; Culver, J.; Stott, J., and Dunn, A. "Three dimensional Monte Carlo code for photon migration through complex heterogeneous media including the adult human head". *Optics Express* 10.3 (2002), pp. 159–170.

[88] Kawrakow, I.; Fippel, M., and Friedrich, K. "3D electron dose calculation using a Voxel based Monte Carlo algorithm (VMC)". *Medical physics* 23.4 (1996), pp. 445–457.

[89] Wang, L. and Jacques, S. L. "Hybrid model of Monte Carlo simulation and diffusion theory for light reflectance by turbid media". *Journal of the Optical Society of America. A, Optics, image science, and vision* 10.8 (1993), pp. 1746–1752.

[90] Zoller, Christian Johannes; Hohmann, Ansgar; Foschum, Florian; Geiger, Simeon; Geiger, Martin; Ertl, Thomas Peter, and Kienle, Alwin. "Parallelized Monte Carlo software to efficiently simulate the light propagation in arbitrarily shaped objects and aligned scattering media". *Journal of biomedical optics* 23.6 (2018), pp. 1–12.

[91] Kattawar, G. W. and Plass, G. N. "Radiance and polarization of multiple scattered light from haze and clouds". *Applied optics* 7.8 (1968), pp. 1519–1527.

[92] Ramella-Roman, Jessica; Prahl, Scott, and Jacques, Steve. "Three Monte Carlo programs of polarized light transport into scattering media: part I". *Optics Express* 13.12 (2005), pp. 4420–4438.

[93] Welch, A. J.; Gardner, Craig; Richards-Kortum, Rebecca; Chan, Eric; Criswell, Glen; Pfefer, Josh, and Warren, Steve. "Propagation of fluorescent light". *Lasers in surgery and medicine* 21.2 (1997), pp. 166–178.

[94] Colasanti, Alberto; Guida, Giovanni; Kisslinger, Annamaria; Liuzzi, Raffaele; Quarto, Maria; Riccio, Patrizia; Roberti, Giuseppe, and Villani, Fulvia. "Multiple processor version of a Monte Carlo code for photon transport in turbid media". *Computer Physics Communications* 132.1-2 (2000), pp. 84–93.

[95] Alerstam, Erik; Svensson, Tomas, and Andersson-Engels, Stefan. "Parallel computing with graphics processing units for high-speed Monte Carlo simulation of photon migration". *Journal of biomedical optics* 13.6 (2008), p. 060504.

[96] Yang, Owen and Choi, Bernard. "Accelerated rescaling of single Monte Carlo simulation runs with the Graphics Processing Unit (GPU)". *Biomedical optics express* 4.11 (2013), pp. 2667–2672.

[97] Leino, Aleksi A.; Pulkkinen, Aki, and Tarvainen, Tanja. "ValoMC: a Monte Carlo software and MATLAB toolbox for simulating light transport in biological tissue". *OSA Continuum* 2.3 (2019), p. 957.

[98] Marti, Dominik; Aasbjerg, Rikke N.; Andersen, Peter E., and Hansen, Anders K. "MCmatlab: an open-source, user-friendly, MATLAB-integrated three-dimensional Monte Carlo light transport solver with heat diffusion and tissue damage". *Journal of biomedical optics* 23.12 (2018), pp. 1–6.

[99] Pogue, Brian W. and Patterson, Michael S. "Review of tissue simulating phantoms for optical spectroscopy, imaging and dosimetry". *Journal of biomedical optics* 11.4 (2006), p. 041102.

[100] Moffitt, Theodore; Chen, Yin-Chu, and Prahl, Scott A. "Preparation and characterization of polyurethane optical phantoms". *Journal of biomedical optics* 11.4 (2006), p. 041103.

[101] Keränen, Ville T.; Mäkynen, Anssi J.; Dayton, Amanda L., and Prahl, Scott A. "Polyurethane phantoms with homogeneous and nearly homogeneous optical properties". *Design and Performance Validation of Phantoms Used in Conjunction with Optical Measurement of Tissue II*. Ed. by Nordstrom, Robert J. SPIE Proceedings. SPIE, 2010, p. 75670D.

[102] Greening, Gage J.; Istfan, Raeef; Higgins, Laura M.; Balachandran, Kartik; Roblyer, Darren; Pierce, Mark C., and Muldoon, Timothy J. "Characterization of thin poly(dimethylsiloxane)-based tissue-simulating phantoms with tunable reduced scattering and absorption coefficients at visible and near-infrared wavelengths". *Journal of biomedical optics* 19.11 (2014), p. 115002.

[103] Ahmad, Muntaser S.; Suardi, Nursakinah; Shukri, Ahmad; Mohammad, Hjouj; Oglat, Ammar A.; Alarab, Azzam, and Makhamrah, Osama. "Chemical Characteristics, Motivation and Strategies in choice of Materials used as Liver Phantom: A Literature Review". *Journal of medical ultrasound* 28.1 (2020), pp. 7–16.

[104] Vardaki, Martha Z. and Kourkoumelis, Nikolaos. "Tissue Phantoms for Biomedical Applications in Raman Spectroscopy: A Review". *Biomedical engineering and computational biology* 11 (2020), p. 11795972209481oo.

[105] Chen, Chen; Ahmed, Midhat; Häfner, Tom; Klämpfl, Florian; Stelzle, Florian, and Schmidt, Michael. "Fabrication of a turbid optofluidic phantom device with tunable mua and mu's to simulate cutaneous vascular perfusion". *Scientific reports* 6 (2016), p. 30567.

[106] Wolf, Marc P.; Salieb-Beugelaar, Georgette B., and Hunziker, Patrick. "PDMS with designer functionalities—Properties, modifications strategies, and applications". *Progress in Polymer Science* 83 (2018), pp. 97–134.

[107] Parthasarathy, Ashwin B.; Shin, Weon Gyu; Zhang, X. J., and Dunn, A. K. "Laser speckle contrast imaging of flow in a microfluidic device". *Biomedical Applications of Light Scattering*. Ed. by Wax, Adam and Backman, Vadim. SPIE Proceedings. SPIE, 2007, p. 644604.

[108] Meglinski, Igor and Matcher, Stephen. "Quantitative assessment of skin layers absorption and skin reflectance spectra simulation in the visible and near-infrared spectral regions". *Optics Letters* 23.4 (2002), pp. 741–753.

[109] Jacques, Steven L. "Optical properties of biological tissues: a review". *Physics in Medicine and Biology* 58.11 (2013), R37–61.

[110] Wray, Susan; Cope, Mark; Delpy, David T.; Wyatt, John S., and Reynolds, E.Osmund R. "Characterization of the near infrared absorption spectra of cytochrome aa3 and haemoglobin for the non-invasive monitoring of cerebral oxygenation". *Biochimica et Biophysica Acta (BBA) - Bioenergetics* 933.1 (1988), pp. 184–192.

[111] Vuylsteke, Marc; van Dorpe, Jo; Roelens, Jan; Bo, Thomas de, and Mordon, Serge. "Endovenous laser treatment: a morphological study in an animal model". *Phlebology* 24.4 (2009), pp. 166–175.

[112] Mazzoni, M. C.; Warnke, K. C.; Arfors, K. E., and Skalak, T. C. "Capillary hemodynamics in hemorrhagic shock and reperfusion: In vivo and model analysis". *American Journal of Physiology-Legacy Content* 267.5 Pt 2 (1994), H1928–35.

[113] Renaud, Olivier and Victoria-Feser, Maria-Pia. "A robust coefficient of determination for regression". *Journal of Statistical Planning and Inference* 140.7 (2010), pp. 1852–1862.

[114] Srivastava, Anil K.; Srivastava, Virendra K., and Ullah, Aman. "The coefficient of determination and its adjusted version in linear regression models". *Econometric Reviews* 14.2 (1995), pp. 229–240.

[115] Camp, Steven. *Iron man AR-15 pistol grip*. 2021. https://grabcad.com/library/iron-man-ar-15-pistol-grip-1.

[116] Aernouts, Ben; van Beers, Robbe; Watté, Rodrigo; Lammertyn, Jeroen, and Saeys, Wouter. "Dependent scattering in Intralipid® phantoms in the 600-1850 nm range". *Optics Express* 22.5 (2014), pp. 6086–6098.

[117] Salter, P. S.; Baum, M.; Alexeev, I.; Schmidt, M., and Booth, M. J. "Exploring the depth range for three-dimensional laser machining with aberration correction". *Optics Express* 22.15 (2014), pp. 17644–17656.

[118] Cumming, Benjamin P.; Turner, Mark D.; Schröder-Turk, Gerd E.; Debbarma, Sukanta; Luther-Davies, Barry, and Gu, Min. "Adaptive optics enhanced direct laser writing of high refractive index gyroid photonic crystals in chalcogenide glass". *Optics Express* 22.1 (2014), pp. 689–698.

[119] Booth, M. J.; Neil, M.A.A., and Wilson, T. "Aberration correction for confocal imaging in refractive-index-mismatched media". *Journal of Microscopy* 192.2 (1998), pp. 90–98.

[120] Europäische Union. *Richtlinie 2006/25/EG*. 5.04.2006.

[121] Williams, Charles S. and Becklund, Orville A. *Introduction to the optical transfer function*. Bellingham, Wash.: SPIE Press, 2002.

[122] Wagner, Omer; Pandya, Aditya; Chemla, Yoav; Pinhas, Hadar; Schelkanova, Irina; Shahmoon, Asaf; Mandel, Yossi; Douplik, Alexandre, and Zalevsky, Zeev. "Non-labeled lensless micro-endoscopic approach for cellular imaging through highly scattering media". *Bioscience reports* 38.1 (2018).

[123] van Veen, Robert; Sterenborg, Henricus; Pifferi, Antonio; Torricelli, Alessandro; Chikoidze, Ekaterine, and Cubeddu, Rinaldo. "Determination of visible near-IR absorption coefficients of mammalian fat using time- and spatially resolved diffuse reflectance and transmission spectroscopy". *Journal of biomedical optics* 10.5 (2005), p. 054004.

[124] Zonios, George; Bykowski, Julie, and Kollias, Nikiforos. "Skin melanin, hemoglobin, and light scattering properties can be quantitatively assessed in vivo using diffuse reflectance spectroscopy". *The Journal of investigative dermatology* 117.6 (2001), pp. 1452–1457.

[125] Jonasson, Hanna; Fredriksson, Ingemar; Pettersson, Anders; Larsson, Marcus, and Strömberg, Tomas. "Oxygen saturation, red blood cell tissue fraction and speed resolved perfusion - A new optical method for microcirculatory assessment". *Microvascular research* 102 (2015), pp. 70–77.

Own publications referring to this work

[P1] Späth, Moritz; Hohmann, Martin; Rohde, Maximilian; Lengenfelder, Benjamin; Stelzle, Florian, and Klämpfl, Florian. "Determination of the diameter of simulated human capillaries using shifted position-diffuse reflectance imaging". *Journal of biophotonics* 14.4 (2021), e202000465.

[P2] Späth, Moritz; Rohde, Maximilian; Ni, Dongqin; Knieling, Ferdinand; Stelzle, Florian; Schmidt, Michael; Klämpfl, Florian, and Hohmann, Martin. "The influence of the optical properties on the determination of capillary diameters". *Scientific reports* 12.1 (2022), p. 270.

[P3] Späth, Moritz; Hohmann, Martin; Roider, Clemens; Lengenfelder, Benjamin; Stelzle, Florian; Wirtz, Stefan, and Klämpfl, Florian. "Towards shifted position-diffuse reflectance imaging of anatomically correctly scaled human microvasculature". *Scientific reports* 10.1 (2020), p. 17391.

[P4] Späth, Moritz; Hohmann, Martin; Stelzle, Florian, and Klämpfl, Florian. "Lateral resolution and imaging depth of shifted position-diffuse reflectance imaging". *Diffuse Optical Spectroscopy and Imaging VIII*. Ed. by Contini, Davide; Hoshi, Yoko, and O'Sullivan, Thomas D. SPIE, 2021, p. 67.

[P5] Späth, Moritz; Romboy, Alexander; Nzenwata, Ijeoma; Rohde, Maximilian; Ni, Dongqin; Ackermann, Lisa; Stelzle, Florian; Hohmann, Martin, and Klämpfl, Florian. "Experimental Validation of Shifted Position-Diffuse Reflectance Imaging (SP-DRI) on Optical Phantoms". *Sensors (Basel, Switzerland)* 22.24 (2022), p. 9880.

[P6] Späth, Moritz; Hohmann, Martin; Rohde, Maximilian, and Klämpfl, Florian. "Numerical Aperture for Photon Detection within Shifted Position-Diffuse Reflectance Imaging". *Frontiers in Optics + Laser Science 2021*. Washington, D.C.: OSA, 2021, JTu1A.114.

Students' theses referring to this work

[S1] Romboy, Alexander. "Gestaltung eines Sensorkopfs zur Messung der diffusen Reflexion". Master's thesis. Institute of Photonic Technologies, 2022.

[S2] Nzenwata, Ijeoma. "Fabrication of optical phantoms with fine capillary structures embedded". Project report. Institute of Photonic Technologies, 2022.

Reihenübersicht

Koordination der Reihe (Stand 2024):
Geschäftsstelle Maschinenbau, Dr.-Ing. Oliver Kreis, www.mb.fau.de/diss/

Im Rahmen der Reihe sind bisher die nachfolgenden Bände erschienen.

Band 1 – 52
Fertigungstechnik – Erlangen
ISSN 1431-6226
Carl Hanser Verlag, München

Band 53 – 307
Fertigungstechnik – Erlangen
ISSN 1431-6226
Meisenbach Verlag, Bamberg

ab Band 308
FAU Studien aus dem Maschinenbau
ISSN 2625-9974
FAU University Press, Erlangen

Die Zugehörigkeit zu den jeweiligen Lehrstühlen ist wie folgt gekennzeichnet:

Lehrstühle:

FAPS	Lehrstuhl für Fertigungsautomatisierung und Produktionssystematik
FMT	Lehrstuhl für Fertigungsmesstechnik
KTmfk	Lehrstuhl für Konstruktionstechnik
LFT	Lehrstuhl für Fertigungstechnologie
LGT	Lehrstuhl für Gießereitechnik
LPT	Lehrstuhl für Photonische Technologien
REP	Lehrstuhl für Ressourcen- und Energieeffiziente Produktionsmaschinen

Band 1: Andreas Hemberger
Innovationspotentiale in der rechnerintegrierten Produktion durch wissensbasierte Systeme
FAPS, 208 Seiten, 107 Bilder. 1988.
ISBN 3-446-15234-2.

Band 2: Detlef Classe
Beitrag zur Steigerung der Flexibilität automatisierter Montagesysteme durch Sensorintegration und erweiterte Steuerungskonzepte
FAPS, 194 Seiten, 70 Bilder. 1988.
ISBN 3-446-15529-5.

Band 3: Friedrich-Wilhelm Nolting
Projektierung von Montagesystemen
FAPS, 201 Seiten, 107 Bilder, 1 Tab. 1989.ISBN 3-446-15541-4.

Band 4: Karsten Schlüter
Nutzungsgradsteigerung von Montagesystemen durch den Einsatz der Simulationstechnik
FAPS, 177 Seiten, 97 Bilder. 1989.
ISBN 3-446-15542-2.

Band 5: Shir-Kuan Lin
Aufbau von Modellen zur Lageregelung von Industrierobotern
FAPS, 168 Seiten, 46 Bilder. 1989.
ISBN 3-446-15546-5.

Band 6: Rudolf Nuss
Untersuchungen zur Bearbeitungsqualität im Fertigungssystem Laserstrahlschneiden
LFT, 206 Seiten, 115 Bilder, 6 Tab. 1989. ISBN 3-446-15783-2.

Band 7: Wolfgang Scholz
Modell zur datenbankgestützten Planung automatisierter Montageanlagen
FAPS, 194 Seiten, 89 Bilder. 1989.
ISBN 3-446-15825-1.

Band 8: Hans-Jürgen Wißmeier
Beitrag zur Beurteilung des Bruchverhaltens von Hartmetall-Fließpreßmatrizen
LFT, 179 Seiten, 99 Bilder, 9 Tab. 1989. ISBN 3-446-15921-5.

Band 9: Rainer Eisele
Konzeption und Wirtschaftlichkeit von Planungssystemen in der Produktion
FAPS, 183 Seiten, 86 Bilder. 1990.
ISBN 3-446-16107-4.

Band 10: Rolf Pfeiffer
Technologisch orientierte Montageplanung am Beispiel der Schraubtechnik
FAPS, 216 Seiten, 102 Bilder, 16 Tab. 1990. ISBN 3-446-16161-9.

Band 11: Herbert Fischer
Verteilte Planungssysteme zur Flexibilitätssteigerung der rechnerintegrierten Teilefertigung
FAPS, 201 Seiten, 82 Bilder. 1990.
ISBN 3-446-16105-8.

Band 12: Gerhard Kleineidam
CAD/CAP: Rechnergestützte Montagefeinplanung
FAPS, 203 Seiten, 107 Bilder. 1990.
ISBN 3-446-16112-0.

Band 13: Frank Vollertsen
Pulvermetallurgische Verarbeitung eines übereutektoiden verschleißfesten Stahls
LFT, XIII u. 217 Seiten, 67 Bilder, 34 Tab. 1990.
ISBN 3-446-16133-3.

Band 14: Stephan Biermann
Untersuchungen zur Anlagen- und Prozeßdiagnostik für das Schneiden mit CO_2-Hochleistungslasern
LFT, VIII u. 170 Seiten, 93 Bilder, 4 Tab. 1991. ISBN 3-446-16269-0.

Band 15: Uwe Geißler
Material- und Datenfluß in einer flexiblen Blechbearbeitungszelle
LFT, 124 Seiten, 41 Bilder, 7 Tab. 1991. ISBN 3-446-16358-1.

Band 16: Frank Oswald Hake
Entwicklung eines rechnergestützten Diagnosesystems für automatisierte Montagezellen
FAPS, XIV u. 166 Seiten, 77 Bilder. 1991. ISBN 3-446-16428-6.

Band 17: Herbert Reichel
Optimierung der Werkzeugbereitstellung durch rechnergestützte Arbeitsfolgenbestimmung
FAPS, 198 Seiten, 73 Bilder, 2 Tab. 1991. ISBN 3-446-16453-7.

Band 18: Josef Scheller
Modellierung und Einsatz von Softwaresystemen für rechnergeführte Montagezellen
FAPS, 198 Seiten, 65 Bilder. 1991.
ISBN 3-446-16454-5.

Band 19: Arnold vom Ende
Untersuchungen zum Biegeumformen mit elastischer Matrize
LFT, 166 Seiten, 55 Bilder, 13 Tab. 1991. ISBN 3-446-16493-6.

Band 20: Joachim Schmid
Beitrag zum automatisierten Bearbeiten von Keramikguß mit Industrierobotern
FAPS, XIV u. 176 Seiten, 111 Bilder, 6 Tab. 1991.
ISBN 3-446-16560-6.

Band 21: Egon Sommer
Multiprozessorsteuerung für kooperierende Industrieroboter in Montagezellen
FAPS, 188 Seiten, 102 Bilder. 1991.
ISBN 3-446-17062-6.

Band 22: Georg Geyer
Entwicklung problemspezifischer Verfahrensketten in der Montage
FAPS, 192 Seiten, 112 Bilder. 1991.
ISBN 3-446-16552-5.

Band 23: Rainer Flohr
Beitrag zur optimalen Verbindungstechnik in der Oberflächenmontage (SMT)
FAPS, 186 Seiten, 79 Bilder. 1991.
ISBN 3-446-16568-1.

Band 24: Alfons Rief
Untersuchungen zur Verfahrensfolge Laserstrahlschneiden und -schweißen in der Rohkarosseriefertigung
LFT, VI u. 145 Seiten, 58 Bilder, 5 Tab. 1991. ISBN 3-446-16593-2.

Band 25: Christoph Thim
Rechnerunterstützte Optimierung von Materialflußstrukturen in der Elektronikmontage durch Simulation
FAPS, 188 Seiten, 74 Bilder. 1992.
ISBN 3-446-17118-5.

Band 26: Roland Müller
CO_2 -Laserstrahlschneiden von kurzglasverstärkten Verbundwerkstoffen
LFT, 141 Seiten, 107 Bilder, 4 Tab. 1992. ISBN 3-446-17104-5.

Band 27: Günther Schäfer
Integrierte Informationsverarbeitung bei der Montageplanung
FAPS, 195 Seiten, 76 Bilder. 1992.
ISBN 3-446-17117-7.

Band 28: Martin Hoffmann
Entwicklung einerCAD/CAM-Prozeßkette für die Herstellung von Blechbiegeteilen
LFT, 149 Seiten, 89 Bilder. 1992.
ISBN 3-446-17154-1.

Band 29: Peter Hoffmann
Verfahrensfolge Laserstrahlschneiden und –schweißen: Prozeßführung und Systemtechnik in der 3D-Laserstrahlbearbeitung von Blechformteilen
LFT, 186 Seiten, 92 Bilder, 10 Tab. 1992. ISBN 3-446-17153-3.

Band 30: Olaf Schrödel
Flexible Werkstattsteuerung mit objektorientierten Softwarestrukturen
FAPS, 180 Seiten, 84 Bilder. 1992.
ISBN 3-446-17242-4.

Band 31: Hubert Reinisch
Planungs- und Steuerungswerkzeuge zur impliziten Geräteprogrammierung in Roboterzellen
FAPS, XI u. 212 Seiten, 112 Bilder. 1992. ISBN 3-446-17380-3.

Band 32: Brigitte Bärnreuther
Ein Beitrag zur Bewertung des Kommunikationsverhaltens von Automatisierungsgeräten in flexiblen Produktionszellen
FAPS, XI u. 179 Seiten, 71 Bilder. 1992. ISBN 3-446-17451-6.

Band 33: Joachim Hutfless
Laserstrahlregelung und Optikdiagnostik in der Strahlführung einer CO_2-Hochleistungslaseranlage
LFT, 175 Seiten, 70 Bilder, 17 Tab. 1993. ISBN 3-446-17532-6.

Band 34: Uwe Günzel
Entwicklung und Einsatz eines Simula-tionsverfahrens für operative undstrategische Probleme der Produktionsplanung und -steuerung
FAPS, XIV u. 170 Seiten, 66 Bilder, 5 Tab. 1993. ISBN 3-446-17604-7.

Band 35: Bertram Ehmann
Operatives Fertigungscontrolling durch Optimierung auftragsbezogener Bearbeitungsabläufe in der Elektronikfertigung
FAPS, XV u. 167 Seiten, 114 Bilder. 1993. ISBN 3-446-17658-6.

Band 36: Harald Kolléra
Entwicklung eines benutzerorientierten Werkstattprogrammiersystems für das Laserstrahlschneiden
LFT, 129 Seiten, 66 Bilder, 1 Tab. 1993. ISBN 3-446-17719-1.

Band 37: Stephanie Abels
Modellierung und Optimierung von Montageanlagen in einem integrierten Simulationssystem
FAPS, 188 Seiten, 88 Bilder. 1993.
ISBN 3-446-17731-0.

Band 38: Robert Schmidt-Hebbel
Laserstrahlbohren durchflußbestimmender Durchgangslöcher
LFT, 145 Seiten, 63 Bilder, 11 Tab. 1993. ISBN 3-446-17778-7.

Band 39: Norbert Lutz
Oberflächenfeinbearbeitung keramischer Werkstoffe mit XeCl-Excimerlaserstrahlung
LFT, 187 Seiten, 98 Bilder, 29 Tab. 1994. ISBN 3-446-17970-4.

Band 40: Konrad Grampp
Rechnerunterstützung bei Test und Schulung an Steuerungssoftware von SMD-Bestücklinien
FAPS, 178 Seiten, 88 Bilder. 1995.
ISBN 3-446-18173-3.

Band 41: Martin Koch
Wissensbasierte Unterstützung derAngebotsbearbeitung in der Investitionsgüterindustrie
FAPS, 169 Seiten, 68 Bilder. 1995.
ISBN 3-446-18174-1.

Band 42: Armin Gropp
Anlagen- und Prozeßdiagnostik beim Schneiden mit einem gepulsten Nd:YAG-Laser
LFT, 160 Seiten, 88 Bilder, 7 Tab. 1995. ISBN 3-446-18241-1.

Band 43: Werner Heckel
Optische 3D-Konturerfassung und on-line Biegewinkelmessung mit dem Lichtschnittverfahren
LFT, 149 Seiten, 43 Bilder, 11 Tab. 1995. ISBN 3-446-18243-8.

Band 44: Armin Rothhaupt
Modulares Planungssystem zur Optimierung der Elektronikfertigung
FAPS, 180 Seiten, 101 Bilder. 1995.
ISBN 3-446-18307-8.

Band 45: Bernd Zöllner
Adaptive Diagnose in der Elektronikproduktion
FAPS, 195 Seiten, 74 Bilder, 3 Tab. 1995. ISBN 3-446-18308-6.

Band 46: Bodo Vormann
Beitrag zur automatisierten Handhabungsplanung komplexer Blechbiegeteile
LFT, 126 Seiten, 89 Bilder, 3 Tab. 1995. ISBN 3-446-18345-0.

Band 47: Peter Schnepf
Zielkostenorientierte Montageplanung
FAPS, 144 Seiten, 75 Bilder. 1995.
ISBN 3-446-18397-3.

Band 48: Rainer Klotzbücher
Konzept zur rechnerintegrierten Materialversorgung in flexiblen Fertigungssystemen
FAPS, 156 Seiten, 62 Bilder. 1995.
ISBN 3-446-18412-0.

Band 49: Wolfgang Greska
Wissensbasierte Analyse undKlassifizierung von Blechteilen
LFT, 144 Seiten, 96 Bilder. 1995.
ISBN 3-446-18462-7.

Band 50: Jörg Franke
Integrierte Entwicklung neuer Produkt- und Produktionstechnologien für räumliche spritzgegossene Schaltungsträger (3-D MID)
FAPS, 196 Seiten, 86 Bilder, 4 Tab. 1995. ISBN 3-446-18448-1.

Band 51: Franz-Josef Zeller
Sensorplanung und schnelle Sensorregelung für Industrieroboter
FAPS, 190 Seiten, 102 Bilder, 9 Tab. 1995. ISBN 3-446-18601-8.

Band 52: Michael Solvie
Zeitbehandlung und Multimedia-Unterstützung in Feldkommunikationssystemen
FAPS, 200 Seiten, 87 Bilder, 35 Tab. 1996. ISBN 3-446-18607-7.

Band 53: Robert Hopperdietzel
Reengineering in der Elektro- und Elektronikindustrie
FAPS, 180 Seiten, 109 Bilder, 1 Tab. 1996. ISBN 3-87525-070-2.

Band 54: Thomas Rebhahn
Beitrag zur Mikromaterialbearbeitung mit Excimerlasern - Systemkomponenten und Verfahrensoptimierungen
LFT, 148 Seiten, 61 Bilder, 10 Tab. 1996. ISBN 3-87525-075-3.

Band 55: Henning Hanebuth
Laserstrahlhartlöten mit Zweistrahltechnik
LFT, 157 Seiten, 58 Bilder, 11 Tab. 1996. ISBN 3-87525-074-5.

Band 56: Uwe Schönherr
Steuerung und Sensordatenintegration für flexible Fertigungszellen mitkooperierenden Robotern
FAPS, 188 Seiten, 116 Bilder, 3 Tab. 1996. ISBN 3-87525-076-1.

Band 57: Stefan Holzer
Berührungslose Formgebung mit-Laserstrahlung
LFT, 162 Seiten, 69 Bilder, 11 Tab. 1996. ISBN 3-87525-079-6.

Band 58: Markus Schultz
Fertigungsqualität beim 3D-Laserstrahlschweißen vonBlechformteilen
LFT, 165 Seiten, 88 Bilder, 9 Tab. 1997. ISBN 3-87525-080-X.

Band 59: Thomas Krebs
Integration elektromechanischer CA-Anwendungen über einem STEP-Produktmodell
FAPS, 198 Seiten, 58 Bilder, 8 Tab. 1997. ISBN 3-87525-081-8.

Band 60: Jürgen Sturm
Prozeßintegrierte Qualitätssicherung in der Elektronikproduktion
FAPS, 167 Seiten, 112 Bilder, 5 Tab. 1997. ISBN 3-87525-082-6.

Band 61: Andreas Brand
Prozesse und Systeme zur Bestückung räumlicher elektronischer Baugruppen (3D-MID)
FAPS, 182 Seiten, 100 Bilder. 1997. ISBN 3-87525-087-7.

Band 62: Michael Kauf
Regelung der Laserstrahlleistung und der Fokusparameter einer CO_2-Hochleistungslaseranlage
LFT, 140 Seiten, 70 Bilder, 5 Tab. 1997. ISBN 3-87525-083-4.

Band 63: Peter Steinwasser
Modulares Informationsmanagement in der integrierten Produkt- und Prozeßplanung
FAPS, 190 Seiten, 87 Bilder. 1997. ISBN 3-87525-084-2.

Band 64: Georg Liedl
Integriertes Automatisierungskonzept für den flexiblen Materialfluß in der Elektronikproduktion
FAPS, 196 Seiten, 96 Bilder, 3 Tab. 1997. ISBN 3-87525-086-9.

Band 65: Andreas Otto
Transiente Prozesse beim Laserstrahlschweißen
LFT, 132 Seiten, 62 Bilder, 1 Tab. 1997. ISBN 3-87525-089-3.

Band 66: Wolfgang Blöchl
Erweiterte Informationsbereitstellung an offenen CNC-Steuerungen zur Prozeß- und Programmoptimierung
FAPS, 168 Seiten, 96 Bilder. 1997. ISBN 3-87525-091-5.

Band 67: Klaus-Uwe Wolf
Verbesserte Prozeßführung und Prozeßplanung zur Leistungs- und Qualitätssteigerung beim Spulenwickeln
FAPS, 186 Seiten, 125 Bilder. 1997. ISBN 3-87525-092-3.

Band 68: Frank Backes
Technologieorientierte Bahnplanung für die 3D-Laserstrahlbearbeitung
LFT, 138 Seiten, 71 Bilder, 2 Tab. 1997. ISBN 3-87525-093-1.

Band 69: Jürgen Kraus
Laserstrahlumformen von Profilen
LFT, 137 Seiten, 72 Bilder, 8 Tab. 1997. ISBN 3-87525-094-X.

Band 70: Norbert Neubauer
Adaptive Strahlführungen für CO_2-Laseranlagen
LFT, 120 Seiten, 50 Bilder, 3 Tab. 1997. ISBN 3-87525-095-8.

Band 71: Michael Steber
Prozeßoptimierter Betrieb flexibler Schraubstationen in der automatisierten Montage
FAPS, 168 Seiten, 78 Bilder, 3 Tab. 1997. ISBN 3-87525-096-6.

Band 72: Markus Pfestorf
Funktionale 3D-Oberflächenkenngrößen in der Umformtechnik
LFT, 162 Seiten, 84 Bilder, 15 Tab. 1997. ISBN 3-87525-097-4.

Band 73: Volker Franke
Integrierte Planung und Konstruktion von Werkzeugen für die Biegebearbeitung
LFT, 143 Seiten, 81 Bilder. 1998. ISBN 3-87525-098-2.

Band 74: Herbert Scheller
Automatisierte Demontagesysteme und recyclinggerechte Produktgestaltung elektronischer Baugruppen
FAPS, 184 Seiten, 104 Bilder, 17 Tab. 1998. ISBN 3-87525-099-0.

Band 75: Arthur Meßner
Kaltmassivumformung metallischer Kleinstteile – Werkstoffverhalten, Wirkflächenreibung, Prozeßauslegung
LFT, 164 Seiten, 92 Bilder, 14 Tab. 1998. ISBN 3-87525-100-8.

Band 76: Mathias Glasmacher
Prozeß- und Systemtechnik zum Laserstrahl-Mikroschweißen
LFT, 184 Seiten, 104 Bilder, 12 Tab. 1998. ISBN 3-87525-101-6.

Band 77: Michael Schwind
Zerstörungsfreie Ermittlung mechanischer Eigenschaften von Feinblechen mit dem Wirbelstromverfahren
LFT, 124 Seiten, 68 Bilder, 8 Tab. 1998. ISBN 3-87525-102-4.

Band 78: Manfred Gerhard
Qualitätssteigerung in der Elektronikproduktion durch Optimierung der Prozeßführung beim Löten komplexer Baugruppen
FAPS, 179 Seiten, 113 Bilder, 7 Tab. 1998. ISBN 3-87525-103-2.

Band 79: Elke Rauh
Methodische Einbindung der Simulation in die betrieblichen Planungs- und Entscheidungsabläufe
FAPS, 192 Seiten, 114 Bilder, 4 Tab. 1998. ISBN 3-87525-104-0.

Band 80: Sorin Niederkorn
Meßeinrichtung zur Untersuchung der Wirkflächenreibung bei umformtechnischen Prozessen
LFT, 99 Seiten, 46 Bilder, 6 Tab. 1998. ISBN 3-87525-105-9.

Band 81: Stefan Schuberth
Regelung der Fokuslage beim Schweißen mit CO_2-Hochleistungslasern unter Einsatz von adaptiven Optiken
LFT, 140 Seiten, 64 Bilder, 3 Tab. 1998. ISBN 3-87525-106-7.

Band 82: Armando Walter Colombo
Development and Implementation of Hierarchical Control Structures of Flexible Production Systems Using High Level Petri Nets
FAPS, 216 Seiten, 86 Bilder. 1998. ISBN 3-87525-109-1.

Band 83: Otto Meedt
Effizienzsteigerung bei Demontage und Recycling durch flexible Demontagetechnologien und optimierte Produktgestaltung
FAPS, 186 Seiten, 103 Bilder. 1998. ISBN 3-87525-108-3.

Band 84: Knuth Götz
Modelle und effiziente Modellbildung zur Qualitätssicherung in der Elektronikproduktion
FAPS, 212 Seiten, 129 Bilder, 24 Tab. 1998. ISBN 3-87525-112-1.

Band 85: Ralf Luchs
Einsatzmöglichkeiten leitender Klebstoffe zur zuverlässigen Kontaktierung elektronischer Bauelemente in der SMT
FAPS, 176 Seiten, 126 Bilder, 30 Tab. 1998. ISBN 3-87525-113-7.

Band 86: Frank Pöhlau
Entscheidungsgrundlagen zur Einführung räumlicher spritzgegossener Schaltungsträger (3-D MID)
FAPS, 144 Seiten, 99 Bilder. 1999. ISBN 3-87525-114-8.

Band 87: Roland T. A. Kals
Fundamentals on the miniaturization of sheet metal working processes
LFT, 128 Seiten, 58 Bilder, 11 Tab. 1999. ISBN 3-87525-115-6.

Band 88: Gerhard Luhn
Implizites Wissen und technisches Handeln am Beispiel der Elektronikproduktion
FAPS, 252 Seiten, 61 Bilder, 1 Tab. 1999. ISBN 3-87525-116-4.

Band 89: Axel Sprenger
Adaptives Streckbiegen von Aluminium-Strangpreßprofilen
LFT, 114 Seiten, 63 Bilder, 4 Tab. 1999. ISBN 3-87525-117-2.

Band 90: Hans-Jörg Pucher
Untersuchungen zur Prozeßfolge Umformen, Bestücken und Laserstrahllöten von Mikrokontakten
LFT, 158 Seiten, 69 Bilder, 9 Tab. 1999. ISBN 3-87525-119-9.

Band 91: Horst Arnet
Profilbiegen mit kinematischer Gestalterzeugung
LFT, 128 Seiten, 67 Bilder, 7 Tab. 1999. ISBN 3-87525-120-2.

Band 92: Doris Schubart
Prozeßmodellierung und Technologieentwicklung beim Abtragen mit CO_2-Laserstrahlung
LFT, 133 Seiten, 57 Bilder, 13 Tab. 1999. ISBN 3-87525-122-9.

Band 93: Adrianus L. P. Coremans
Laserstrahlsintern von Metallpulver - Prozeßmodellierung, Systemtechnik, Eigenschaften laserstrahlgesinterter Metallkörper
LFT, 184 Seiten, 108 Bilder, 12 Tab. 1999. ISBN 3-87525-124-5.

Band 94: Hans-Martin Biehler
Optimierungskonzepte für Qualitätsdatenverarbeitung und Informationsbereitstellung in der Elektronikfertigung
FAPS, 194 Seiten, 105 Bilder. 1999. ISBN 3-87525-126-1.

Band 95: Wolfgang Becker
Oberflächenausbildung und tribologische Eigenschaften excimerlaserstrahlbearbeiteter Hochleistungskeramiken
LFT, 175 Seiten, 71 Bilder, 3 Tab. 1999. ISBN 3-87525-127-X.

Band 96: Philipp Hein
Innenhochdruck-Umformen von Blechpaaren: Modellierung, Prozeßauslegung und Prozeßführung
LFT, 129 Seiten, 57 Bilder, 7 Tab. 1999. ISBN 3-87525-128-8.

Band 97: Gunter Beitinger
Herstellungs- und Prüfverfahren für thermoplastische Schaltungsträger
FAPS, 169 Seiten, 92 Bilder, 20 Tab. 1999. ISBN 3-87525-129-6.

Band 98: Jürgen Knoblach
Beitrag zur rechnerunterstützten verursachungsgerechten Angebotskalkulation von Blechteilen mit Hilfe wissensbasierter Methoden
LFT, 155 Seiten, 53 Bilder, 26 Tab. 1999. ISBN 3-87525-130-X.

Band 99: Frank Breitenbach
Bildverarbeitungssystem zur Erfassung der Anschlußgeometrie elektronischer SMT-Bauelemente
LFT, 147 Seiten, 92 Bilder, 12 Tab. 2000. ISBN 3-87525-131-8.

Band 100: Bernd Falk
Simulationsbasierte Lebensdauervorhersage für Werkzeuge der Kaltmassivumformung
LFT, 134 Seiten, 44 Bilder, 15 Tab. 2000. ISBN 3-87525-136-9.

Band 101: Wolfgang Schlögl
Integriertes Simulationsdaten-Management für Maschinenentwicklung und Anlagenplanung
FAPS, 169 Seiten, 101 Bilder, 20 Tab. 2000. ISBN 3-87525-137-7.

Band 102: Christian Hinsel
Ermüdungsbruchversagen hartstoffbeschichteter Werkzeugstähle in der Kaltmassivumformung
LFT, 130 Seiten, 80 Bilder, 14 Tab. 2000. ISBN 3-87525-138-5.

Band 103: Stefan Bobbert
Simulationsgestützte Prozessauslegung für das Innenhochdruck-Umformen von Blechpaaren
LFT, 123 Seiten, 77 Bilder. 2000. ISBN 3-87525-145-8.

Band 104: Harald Rottbauer
Modulares Planungswerkzeug zum Produktionsmanagement in der Elektronikproduktion
FAPS, 166 Seiten, 106 Bilder. 2001.
ISBN 3-87525-139-3.

Band 105: Thomas Hennige
Flexible Formgebung von Blechen durch Laserstrahlumformen
LFT, 119 Seiten, 50 Bilder. 2001.
ISBN 3-87525-140-7.

Band 106: Thomas Menzel
Wissensbasierte Methoden für die rechnergestützte Charakterisierung und Bewertung innovativer Fertigungsprozesse
LFT, 152 Seiten, 71 Bilder. 2001.
ISBN 3-87525-142-3.

Band 107: Thomas Stöckel
Kommunikationstechnische Integration der Prozeßebene in Produktionssysteme durch Middleware-Frameworks
FAPS, 147 Seiten, 65 Bilder, 5 Tab.
2001. ISBN 3-87525-143-1.

Band 108: Frank Pitter
Verfügbarkeitssteigerung von Werkzeugmaschinen durch Einsatz mechatronischer Sensorlösungen
FAPS, 158 Seiten, 131 Bilder, 8 Tab.
2001. ISBN 3-87525-144-X.

Band 109: Markus Korneli
Integration lokaler CAP-Systeme in einen globalen Fertigungsdatenverbund
FAPS, 121 Seiten, 53 Bilder, 11 Tab.
2001. ISBN 3-87525-146-6.

Band 110: Burkhard Müller
Laserstrahljustieren mit Excimer-Lasern - Prozeßparameter und Modelle zur Aktorkonstruktion
LFT, 128 Seiten, 36 Bilder, 9 Tab.
2001. ISBN 3-87525-159-8.

Band 111: Jürgen Göhringer
Integrierte Telediagnose via Internet zum effizienten Service von Produktionssystemen
FAPS, 178 Seiten, 98 Bilder, 5 Tab.
2001. ISBN 3-87525-147-4.

Band 112: Robert Feuerstein
Qualitäts- und kosteneffiziente Integration neuer Bauelementetechnologien in die Flachbaugruppenfertigung
FAPS, 161 Seiten, 99 Bilder, 10 Tab.
2001. ISBN 3-87525-151-2.

Band 113: Marcus Reichenberger
Eigenschaften und Einsatzmöglichkeiten alternativer Elektroniklote in der Oberflächenmontage (SMT)
FAPS, 165 Seiten, 97 Bilder, 18 Tab.
2001. ISBN 3-87525-152-0.

Band 114: Alexander Huber
Justieren vormontierter Systeme mit dem Nd:YAG-Laser unter Einsatz von Aktoren
LFT, 122 Seiten, 58 Bilder, 5 Tab.
2001. ISBN 3-87525-153-9.

Band 115: Sami Krimi
Analyse und Optimierung von Montagesystemen in der Elektronikproduktion
FAPS, 155 Seiten, 88 Bilder, 3 Tab.
2001. ISBN 3-87525-157-1.

Band 116: Marion Merklein
Laserstrahlumformen von Aluminiumwerkstoffen - Beeinflussung der Mikrostruktur und der mechanischen Eigenschaften
LFT, 122 Seiten, 65 Bilder, 15 Tab.
2001. ISBN 3-87525-156-3.

Band 117: Thomas Collisi
Ein informationslogistisches Architekturkonzept zur Akquisition simulationsrelevanter Daten
FAPS, 181 Seiten, 105 Bilder, 7 Tab.
2002. ISBN 3-87525-164-4.

Band 118: Markus Koch
Rationalisierung und ergonomische Optimierung im Innenausbau durch den Einsatz moderner Automatisierungstechnik
FAPS, 176 Seiten, 98 Bilder, 9 Tab.
2002. ISBN 3-87525-165-2.

Band 119: Michael Schmidt
Prozeßregelung für das Laserstrahl-Punktschweißen in der Elektronikproduktion
LFT, 152 Seiten, 71 Bilder, 3 Tab.
2002. ISBN 3-87525-166-0.

Band 120: Nicolas Tiesler
Grundlegende Untersuchungen zum Fließpressen metallischer Kleinstteile
LFT, 126 Seiten, 78 Bilder, 12 Tab.
2002. ISBN 3-87525-175-X.

Band 121: Lars Pursche
Methoden zur technologieorientierten Programmierung für die 3D-Lasermikrobearbeitung
LFT, 111 Seiten, 39 Bilder, 0 Tab.
2002. ISBN 3-87525-183-0.

Band 122: Jan-Oliver Brassel
Prozeßkontrolle beim Laserstrahl-Mikroschweißen
LFT, 148 Seiten, 72 Bilder, 12 Tab.
2002. ISBN 3-87525-181-4.

Band 123: Mark Geisel
Prozeßkontrolle und -steuerung beim Laserstrahlschweißen mit den Methoden der nichtlinearen Dynamik
LFT, 135 Seiten, 46 Bilder, 2 Tab.
2002. ISBN 3-87525-180-6.

Band 124: Gerd Eßer
Laserstrahlunterstützte Erzeugung metallischer Leiterstrukturen auf Thermoplastsubstraten für die MID-Technik
LFT, 148 Seiten, 60 Bilder, 6 Tab.
2002. ISBN 3-87525-171-7.

Band 125: Marc Fleckenstein
Qualität laserstrahl-gefügter Mikroverbindungen elektronischer Kontakte
LFT, 159 Seiten, 77 Bilder, 7 Tab.
2002. ISBN 3-87525-170-9.

Band 126: Stefan Kaufmann
Grundlegende Untersuchungen zum Nd:YAG- Laserstrahlfügen von Silizium für Komponenten der Optoelektronik
LFT, 159 Seiten, 100 Bilder, 6 Tab.
2002. ISBN 3-87525-172-5.

Band 127: Thomas Fröhlich
Simultanes Löten von Anschlußkontakten elektronischer Bauelemente mit Diodenlaserstrahlung
LFT, 143 Seiten, 75 Bilder, 6 Tab.
2002. ISBN 3-87525-186-5.

Band 128: Achim Hofmann
Erweiterung der Formgebungsgrenzen beim Umformen von Aluminiumwerkstoffen durch den Einsatz prozessangepasster Platinen
LFT, 113 Seiten, 58 Bilder, 4 Tab. 2002. ISBN 3-87525-182-2.

Band 129: Ingo Kriebitzsch
3 - D MID Technologie in der Automobilelektronik
FAPS, 129 Seiten, 102 Bilder, 10 Tab. 2002. ISBN 3-87525-169-5.

Band 130: Thomas Pohl
Fertigungsqualität und Umformbarkeit laserstrahlgeschweißter Formplatinen aus Aluminiumlegierungen
LFT, 133 Seiten, 93 Bilder, 12 Tab. 2002. ISBN 3-87525-173-3.

Band 131: Matthias Wenk
Entwicklung eines konfigurierbaren Steuerungssystems für die flexible Sensorführung von Industrierobotern
FAPS, 167 Seiten, 85 Bilder, 1 Tab. 2002. ISBN 3-87525-174-1.

Band 132: Matthias Negendanck
Neue Sensorik und Aktorik für Bearbeitungsköpfe zum Laserstrahlschweißen
LFT, 116 Seiten, 60 Bilder, 14 Tab. 2002. ISBN 3-87525-184-9.

Band 133: Oliver Kreis
Integrierte Fertigung - Verfahrensintegration durch Innenhochdruck-Umformen, Trennen und Laserstrahlschweißen in einem Werkzeug sowie ihre tele- und multimediale Präsentation
LFT, 167 Seiten, 90 Bilder, 43 Tab. 2002. ISBN 3-87525-176-8.

Band 134: Stefan Trautner
Technische Umsetzung produktbezogener Instrumente der Umweltpolitik bei Elektro- und Elektronikgeräten
FAPS, 179 Seiten, 92 Bilder, 11 Tab. 2002. ISBN 3-87525-177-6.

Band 135: Roland Meier
Strategien für einen produktorientierten Einsatz räumlicher spritzgegossener Schaltungsträger (3-D MID)
FAPS, 155 Seiten, 88 Bilder, 14 Tab. 2002. ISBN 3-87525-178-4.

Band 136: Jürgen Wunderlich
Kostensimulation - Simulationsbasierte Wirtschaftlichkeitsregelung komplexer Produktionssysteme
FAPS, 202 Seiten, 119 Bilder, 17 Tab. 2002. ISBN 3-87525-179-2.

Band 137: Stefan Novotny
Innenhochdruck-Umformen von Blechen aus Aluminium- und Magnesiumlegierungen bei erhöhter Temperatur
LFT, 132 Seiten, 82 Bilder, 6 Tab. 2002. ISBN 3-87525-185-7.

Band 138: Andreas Licha
Flexible Montageautomatisierung zur Komplettmontage flächenhafter Produktstrukturen durch kooperierende Industrieroboter
FAPS, 158 Seiten, 87 Bilder, 8 Tab. 2003. ISBN 3-87525-189-X.

Band 139: Michael Eisenbarth
Beitrag zur Optimierung der Aufbau- und Verbindungstechnik für mechatronische Baugruppen
FAPS, 207 Seiten, 141 Bilder, 9 Tab. 2003. ISBN 3-87525-190-3.

Band 140: Frank Christoph
Durchgängige simulationsgestützte Planung von Fertigungseinrichtungen der Elektronikproduktion
FAPS, 187 Seiten, 107 Bilder, 9 Tab. 2003. ISBN 3-87525-191-1.

Band 141: Hinnerk Hagenah
Simulationsbasierte Bestimmung der zu erwartenden Maßhaltigkeit für das Blechbiegen
LFT, 131 Seiten, 36 Bilder, 26 Tab. 2003. ISBN 3-87525-192-X.

Band 142: Ralf Eckstein
Scherschneiden und Biegen metallischer Kleinstteile - Materialeinfluss und Materialverhalten
LFT, 148 Seiten, 71 Bilder, 19 Tab. 2003. ISBN 3-87525-193-8.

Band 143: Frank H. Meyer-Pittroff
Excimerlaserstrahlbiegen dünner metallischer Folien mit homogener Lichtlinie
LFT, 138 Seiten, 60 Bilder, 16 Tab. 2003. ISBN 3-87525-196-2.

Band 144: Andreas Kach
Rechnergestützte Anpassung von Laserstrahlschneidbahnen an Bauteilabweichungen
LFT, 139 Seiten, 69 Bilder, 11 Tab. 2004. ISBN 3-87525-197-0.

Band 145: Stefan Hierl
System- und Prozeßtechnik für das simultane Löten mit Diodenlaserstrahlung von elektronischen Bauelementen
LFT, 124 Seiten, 66 Bilder, 4 Tab. 2004. ISBN 3-87525-198-9.

Band 146: Thomas Neudecker
Tribologische Eigenschaften keramischer Blechumformwerkzeuge-Einfluss einer Oberflächenendbearbeitung mittels Excimerlaserstrahlung
LFT, 166 Seiten, 75 Bilder, 26 Tab. 2004. ISBN 3-87525-200-4.

Band 147: Ulrich Wenger
Prozessoptimierung in der Wickeltechnik durch innovative maschinenbauliche und regelungstechnische Ansätze
FAPS, 132 Seiten, 88 Bilder, 0 Tab. 2004. ISBN 3-87525-203-9.

Band 148: Stefan Slama
Effizienzsteigerung in der Montage durch marktorientierte Montagestrukturen und erweiterte Mitarbeiterkompetenz
FAPS, 188 Seiten, 125 Bilder, 0 Tab. 2004. ISBN 3-87525-204-7.

Band 149: Thomas Wurm
Laserstrahljustieren mittels Aktoren-Entwicklung von Konzepten und Methoden für die rechnerunterstützte Modellierung und Optimierung von komplexen Aktorsystemen in der Mikrotechnik
LFT, 122 Seiten, 51 Bilder, 9 Tab. 2004. ISBN 3-87525-206-3.

Band 150: Martino Celeghini
Wirkmedienbasierte Blechumformung: Grundlagenuntersuchungen zum Einfluss von Werkstoff und Bauteilgeometrie
LFT, 146 Seiten, 77 Bilder, 6 Tab.
2004. ISBN 3-87525-207-1.

Band 151: Ralph Hohenstein
Entwurf hochdynamischer Sensor- und Regelsysteme für die adaptiveLaserbearbeitung
LFT, 282 Seiten, 63 Bilder, 16 Tab.
2004. ISBN 3-87525-210-1.

Band 152: Angelika Hutterer
Entwicklung prozessüberwachender Regelkreise für flexible Formgebungsprozesse
LFT, 149 Seiten, 57 Bilder, 2 Tab.
2005. ISBN 3-87525-212-8.

Band 153: Emil Egerer
Massivumformen metallischer Kleinstteile bei erhöhter Prozesstemperatur
LFT, 158 Seiten, 87 Bilder, 10 Tab.
2005. ISBN 3-87525-213-6.

Band 154: Rüdiger Holzmann
Strategien zur nachhaltigen Optimierung von Qualität und Zuverlässigkeit in der Fertigung hochintegrierter Flachbaugruppen
FAPS, 186 Seiten, 99 Bilder, 19 Tab.
2005. ISBN 3-87525-217-9.

Band 155: Marco Nock
Biegeumformen mit Elastomerwerkzeugen Modellierung, Prozessauslegung und Abgrenzung des Verfahrens am Beispiel des Rohrbiegens
LFT, 164 Seiten, 85 Bilder, 13 Tab.
2005. ISBN 3-87525-218-7.

Band 156: Frank Niebling
Qualifizierung einer Prozesskette zum Laserstrahlsintern metallischer Bauteile
LFT, 148 Seiten, 89 Bilder, 3 Tab.
2005. ISBN 3-87525-219-5.

Band 157: Markus Meiler
Großserientauglichkeit trockenschmierstoffbeschichteter Aluminiumbleche im Presswerk Grundlegende Untersuchungen zur Tribologie, zum Umformverhalten und Bauteilversuche
LFT, 104 Seiten, 57 Bilder, 21 Tab.
2005. ISBN 3-87525-221-7.

Band 158: Agus Sutanto
Solution Approaches for Planning of Assembly Systems in Three-Dimensional Virtual Environments
FAPS, 169 Seiten, 98 Bilder, 3 Tab.
2005. ISBN 3-87525-220-9.

Band 159: Matthias Boiger
Hochleistungssysteme für die Fertigung elektronischer Baugruppen auf der Basis flexibler Schaltungsträger
FAPS, 175 Seiten, 111 Bilder, 8 Tab.
2005. ISBN 3-87525-222-5.

Band 160: Matthias Pitz
Laserunterstütztes Biegen höchstfester Mehrphasenstähle
LFT, 120 Seiten, 73 Bilder, 11 Tab.
2005. ISBN 3-87525-223-3.

Band 161: Meik Vahl
Beitrag zur gezielten Beeinflussung des Werkstoffflusses beim Innenhochdruck-Umformen von Blechen
LFT, 165 Seiten, 94 Bilder, 15 Tab.
2005. ISBN 3-87525-224-1.

Band 162: Peter K. Kraus
Plattformstrategien - Realisierung einer varianz- und kostenoptimierten Wertschöpfung
FAPS, 181 Seiten, 95 Bilder, 0 Tab.
2005. ISBN 3-87525-226-8.

Band 163: Adrienn Cser
Laserstrahlschmelzabtrag - Prozessanalyse und -modellierung
LFT, 146 Seiten, 79 Bilder, 3 Tab.
2005. ISBN 3-87525-227-6.

Band 164: Markus C. Hahn
Grundlegende Untersuchungen zur Herstellung von Leichtbauverbundstrukturen mit Aluminiumschaumkern
LFT, 143 Seiten, 60 Bilder, 16 Tab.
2005. ISBN 3-87525-228-4.

Band 165: Gordana Michos
Mechatronische Ansätze zur Optimierung von Vorschubachsen
FAPS, 146 Seiten, 87 Bilder, 17 Tab.
2005. ISBN 3-87525-230-6.

Band 166: Markus Stark
Auslegung und Fertigung hochpräziser Faser-Kollimator-Arrays
LFT, 158 Seiten, 115 Bilder, 11 Tab.
2005. ISBN 3-87525-231-4.

Band 167: Yurong Zhou
Kollaboratives Engineering Management in der integrierten virtuellen Entwicklung der Anlagen für die Elektronikproduktion
FAPS, 156 Seiten, 84 Bilder, 6 Tab.
2005. ISBN 3-87525-232-2.

Band 168: Werner Enser
Neue Formen permanenter und lösbarer elektrischer Kontaktierungen für mechatronische Baugruppen
FAPS, 190 Seiten, 112 Bilder, 5 Tab.
2005. ISBN 3-87525-233-0.

Band 169: Katrin Melzer
Integrierte Produktpolitik bei elektrischen und elektronischen Geräten zur Optimierung des Product-Life-Cycle
FAPS, 155 Seiten, 91 Bilder, 17 Tab.
2005. ISBN 3-87525-234-9.

Band 170: Alexander Putz
Grundlegende Untersuchungen zur Erfassung der realen Vorspannung von armierten Kaltfließpresswerkzeugen mittels Ultraschall
LFT, 137 Seiten, 71 Bilder, 15 Tab.
2006. ISBN 3-87525-237-3.

Band 171: Martin Prechtl
Automatisiertes Schichtverfahren für metallische Folien - System- und Prozesstechnik
LFT, 154 Seiten, 45 Bilder, 7 Tab.
2006. ISBN 3-87525-238-1.

Band 172: Markus Meidert
Beitrag zur deterministischen Lebensdauerabschätzung von Werkzeugen der Kaltmassivumformung
LFT, 131 Seiten, 78 Bilder, 9 Tab.
2006. ISBN 3-87525-239-X.

Band 173: Bernd Müller
Robuste, automatisierte Montagesysteme durch adaptive Prozessführung und montageübergreifende Fehlerprävention am Beispiel flächiger Leichtbauteile
FAPS, 147 Seiten, 77 Bilder, 0 Tab.
2006. ISBN 3-87525-240-3.

Band 174: Alexander Hofmann
Hybrides Laserdurchstrahlschweißen von Kunststoffen
LFT, 136 Seiten, 72 Bilder, 4 Tab.
2006. ISBN 978-3-87525-243-9.

Band 175: Peter Wölflick
Innovative Substrate und Prozesse mit feinsten Strukturen für bleifreie Mechatronik-Anwendungen
FAPS, 177 Seiten, 148 Bilder, 24 Tab. 2006.
ISBN 978-3-87525-246-0.

Band 176: Attila Komlodi
Detection and Prevention of Hot Cracks during Laser Welding of Aluminium Alloys Using Advanced Simulation Methods
LFT, 155 Seiten, 89 Bilder, 14 Tab. 2006. ISBN 978-3-87525-248-4.

Band 177: Uwe Popp
Grundlegende Untersuchungen zum Laserstrahlstrukturieren von Kaltmassivumformwerkzeugen
LFT, 140 Seiten, 67 Bilder, 16 Tab. 2006. ISBN 978-3-87525-249-1.

Band 178: Veit Rückel
Rechnergestützte Ablaufplanung und Bahngenerierung Für kooperierende Industrieroboter
FAPS, 148 Seiten, 75 Bilder, 7 Tab. 2006. ISBN 978-3-87525-250-7.

Band 179: Manfred Dirscherl
Nicht-thermische Mikrojustiertechnik mittels ultrakurzer Laserpulse
LFT, 154 Seiten, 69 Bilder, 10 Tab. 2007. ISBN 978-3-87525-251-4.

Band 180: Yong Zhuo
Entwurf eines rechnergestützten integrierten Systems für Konstruktion und Fertigungsplanung räumlicher spritzgegossener Schaltungsträger (3D-MID)
FAPS, 181 Seiten, 95 Bilder, 5 Tab. 2007. ISBN 978-3-87525-253-8.

Band 181: Stefan Lang
Durchgängige Mitarbeiterinformation zur Steigerung von Effizienz und Prozesssicherheit in der Produktion
FAPS, 172 Seiten, 93 Bilder. 2007. ISBN 978-3-87525-257-6.

Band 182: Hans-Joachim Krauß
Laserstrahlinduzierte Pyrolyse präkeramischer Polymere
LFT, 171 Seiten, 100 Bilder. 2007. ISBN 978-3-87525-258-3.

Band 183: Stefan Junker
Technologien und Systemlösungen für die flexibel automatisierte Bestückung permanent erregter Läufer mit oberflächenmontierten Dauermagneten
FAPS, 173 Seiten, 75 Bilder. 2007. ISBN 978-3-87525-259-0.

Band 184: Rainer Kohlbauer
Wissensbasierte Methoden für die simulationsgestützte Auslegung wirkmedienbasierter Blechumformprozesse
LFT, 135 Seiten, 50 Bilder. 2007. ISBN 978-3-87525-260-6.

Band 185: Klaus Lamprecht
Wirkmedienbasierte Umformung tiefgezogener Vorformen unter besonderer Berücksichtigung maßgeschneiderter Halbzeuge
LFT, 137 Seiten, 81 Bilder. 2007. ISBN 978-3-87525-265-1.

Band 186: Bernd Zolleiß
Optimierte Prozesse und Systeme für die Bestückung mechatronischerBaugruppen
FAPS, 180 Seiten, 117 Bilder. 2007. ISBN 978-3-87525-266-8.

Band 187: Michael Kerausch
Simulationsgestützte Prozessauslegung für das Umformen lokal wärmebehandelter Aluminiumplatinen
LFT, 146 Seiten, 76 Bilder, 7 Tab. 2007. ISBN 978-3-87525-267-5.

Band 188: Matthias Weber
Unterstützung der Wandlungsfähigkeit von Produktionsanlagen durch innovative Softwaresysteme
FAPS, 183 Seiten, 122 Bilder, 3 Tab. 2007. ISBN 978-3-87525-269-9.

Band 189: Thomas Frick
Untersuchung der prozessbestimmenden Strahl-Stoff-Wechselwirkungen beim Laserstrahlschweißen von Kunststoffen
LFT, 104 Seiten, 62 Bilder, 8 Tab. 2007. ISBN 978-3-87525-268-2.

Band 190: Joachim Hecht
Werkstoffcharakterisierung und Prozessauslegung für die wirkmedienbasierte Doppelblech-Umformung von Magnesiumlegierungen
LFT, 107 Seiten, 91 Bilder, 2 Tab. 2007. ISBN 978-3-87525-270-5.

Band 191: Ralf Völkl
Stochastische Simulation zur Werkzeuglebensdaueroptimierung und Präzisionsfertigung in der Kaltmassivumformung
LFT, 178 Seiten, 75 Bilder, 12 Tab. 2008. ISBN 978-3-87525-272-9.

Band 192: Massimo Tolazzi
Innenhochdruck-Umformen verstärkter Blech-Rahmenstrukturen
LFT, 164 Seiten, 85 Bilder, 7 Tab. 2008. ISBN 978-3-87525-273-6.

Band 193: Cornelia Hoff
Untersuchung der Prozesseinflussgrößen beim Presshärten des höchstfesten Vergütungsstahls 22MnB5
LFT, 133 Seiten, 92 Bilder, 5 Tab. 2008. ISBN 978-3-87525-275-0.

Band 194: Christian Alvarez
Simulationsgestützte Methoden zur effizienten Gestaltung von Lötprozessen in der Elektronikproduktion
FAPS, 149 Seiten, 86 Bilder, 8 Tab. 2008. ISBN 978-3-87525-277-4.

Band 195: Andreas Kunze
Automatisierte Montage von makromechatronischen Modulen zur flexiblen Integration in hybride Pkw-Bordnetzsysteme
FAPS, 160 Seiten, 90 Bilder, 14 Tab. 2008.
ISBN 978-3-87525-278-1.

Band 196: Wolfgang Hußnätter
Grundlegende Untersuchungen zur experimentellen Ermittlung und zur Modellierung von Fließortkurven bei erhöhten Temperaturen
LFT, 152 Seiten, 73 Bilder, 21 Tab. 2008. ISBN 978-3-87525-279-8.

Band 197: Thomas Bigl
Entwicklung, angepasste Herstellungsverfahren und erweiterte Qualitätssicherung von einsatzgerechten elektronischen Baugruppen
FAPS, 175 Seiten, 107 Bilder, 14 Tab. 2008.
ISBN 978-3-87525-280-4.

Band 198: Stephan Roth
Grundlegende Untersuchungen zum Excimerlaserstrahl-Abtragen unter Flüssigkeitsfilmen
LFT, 113 Seiten, 47 Bilder, 14 Tab. 2008. ISBN 978-3-87525-281-1.

Band 199: Artur Giera
Prozesstechnische Untersuchungen zum Rührreibschweißen metallischer Werkstoffe
LFT, 179 Seiten, 104 Bilder, 36 Tab. 2008. ISBN 978-3-87525-282-8.

Band 200: Jürgen Lechler
Beschreibung und Modellierung des Werkstoffverhaltens von presshärtbaren Bor-Manganstählen
LFT, 154 Seiten, 75 Bilder, 12 Tab. 2009. ISBN 978-3-87525-286-6.

Band 201: Andreas Blankl
Untersuchungen zur Erhöhung der Prozessrobustheit bei der Innenhochdruck-Umformung von flächigen Halbzeugen mit vor- bzw. nachgeschalteten Laserstrahlfügeoperationen
LFT, 120 Seiten, 68 Bilder, 9 Tab. 2009. ISBN 978-3-87525-287-3.

Band 202: Andreas Schaller
Modellierung eines nachfrageorientierten Produktionskonzeptes für mobile Telekommunikationsgeräte
FAPS, 120 Seiten, 79 Bilder, 0 Tab. 2009. ISBN 978-3-87525-289-7.

Band 203: Claudius Schimpf
Optimierung von Zuverlässigkeitsuntersuchungen, Prüfabläufen und Nacharbeitsprozessen in der Elektronikproduktion
FAPS, 162 Seiten, 90 Bilder, 14 Tab. 2009.
ISBN 978-3-87525-290-3.

Band 204: Simon Dietrich
Sensoriken zur Schwerpunktslagebestimmung der optischen Prozessemissionen beim Laserstrahltiefschweißen
LFT, 138 Seiten, 70 Bilder, 5 Tab. 2009. ISBN 978-3-87525-292-7.

Band 205: Wolfgang Wolf
Entwicklung eines agentenbasierten Steuerungssystems zur Materialflussorganisation im wandelbaren Produktionsumfeld
FAPS, 167 Seiten, 98 Bilder. 2009. ISBN 978-3-87525-293-4.

Band 206: Steffen Polster
Laserdurchstrahlschweißen transparenter Polymerbauteile
LFT, 160 Seiten, 92 Bilder, 13 Tab. 2009. ISBN 978-3-87525-294-1.

Band 207: Stephan Manuel Dörfler
Rührreibschweißen von walzplattiertem Halbzeug und Aluminiumblech zur Herstellung flächiger Aluminiumschaum-Sandwich-Verbundstrukturen
LFT, 190 Seiten, 98 Bilder, 5 Tab. 2009. ISBN 978-3-87525-295-8.

Band 208: Uwe Vogt
Seriennahe Auslegung von Aluminium Tailored Heat Treated Blanks
LFT, 151 Seiten, 68 Bilder, 26 Tab. 2009. ISBN 978-3-87525-296-5.

Band 209: Till Laumann
Qualitative und quantitative Bewertung der Crashtauglichkeit von höchstfesten Stählen
LFT, 117 Seiten, 69 Bilder, 7 Tab. 2009. ISBN 978-3-87525-299-6.

Band 210: Alexander Diehl
Größeneffekte bei Biegeprozessen-Entwicklung einer Methodik zur Identifikation und Quantifizierung
LFT, 180 Seiten, 92 Bilder, 12 Tab. 2010. ISBN 978-3-87525-302-3.

Band 211: Detlev Staud
Effiziente Prozesskettenauslegung für das Umformen lokal wärmebehandelter und geschweißter Aluminiumbleche
LFT, 164 Seiten, 72 Bilder, 12 Tab. 2010. ISBN 978-3-87525-303-0.

Band 212: Jens Ackermann
Prozesssicherung beim Laserdurchstrahlschweißen thermoplastischer Kunststoffe
LPT, 129 Seiten, 74 Bilder, 13 Tab. 2010. ISBN 978-3-87525-305-4.

Band 213: Stephan Weidel
Grundlegende Untersuchungen zum Kontaktzustand zwischen Werkstück und Werkzeug bei umformtechnischen Prozessen unter tribologischen Gesichtspunkten
LFT, 144 Seiten, 67 Bilder, 11 Tab. 2010. ISBN 978-3-87525-307-8.

Band 214: Stefan Geißdörfer
Entwicklung eines mesoskopischen Modells zur Abbildung von Größeneffekten in der Kaltmassivumformung mit Methoden der FE-Simulation
LFT, 133 Seiten, 83 Bilder, 11 Tab. 2010. ISBN 978-3-87525-308-5.

Band 215: Christian Matzner
Konzeption produktspezifischer Lösungen zur Robustheitssteigerung elektronischer Systeme gegen die Einwirkung von Betauung im Automobil
FAPS, 165 Seiten, 93 Bilder, 14 Tab. 2010. ISBN 978-3-87525-309-2.

Band 216: Florian Schüßler
Verbindungs- und Systemtechnik für thermisch hochbeanspruchte und miniaturisierte elektronische Baugruppen
FAPS, 184 Seiten, 93 Bilder, 18 Tab. 2010.
ISBN 978-3-87525-310-8.

Band 217: Massimo Cojutti
Strategien zur Erweiterung der Prozessgrenzen bei der Innhochdruck-Umformung von Rohren und Blechpaaren
LFT, 125 Seiten, 56 Bilder, 9 Tab. 2010. ISBN 978-3-87525-312-2.

Band 218: Raoul Plettke
Mehrkriterielle Optimierung komplexer Aktorsysteme für das Laserstrahljustieren
LFT, 152 Seiten, 25 Bilder, 3 Tab. 2010. ISBN 978-3-87525-315-3.

Band 219: Andreas Dobroschke
Flexible Automatisierungslösungen für die Fertigung wickeltechnischer Produkte
FAPS, 184 Seiten, 109 Bilder, 18 Tab. 2011.
ISBN 978-3-87525-317-7.

Band 220: Azhar Zam
Optical Tissue Differentiation for Sensor-Controlled Tissue-Specific Laser Surgery
LPT, 99 Seiten, 45 Bilder, 8 Tab. 2011. ISBN 978-3-87525-318-4.

Band 221: Michael Rösch
Potenziale und Strategien zur Optimierung des Schablonendruckprozesses in der Elektronikproduktion
FAPS, 192 Seiten, 127 Bilder, 19 Tab. 2011.
ISBN 978-3-87525-319-1.

Band 222: Thomas Rechtenwald
Quasi-isothermes Laserstrahlsintern von Hochtemperatur-Thermoplasten - Eine Betrachtung werkstoff-prozessspezifischer Aspekte am Beispiel PEEK
LPT, 150 Seiten, 62 Bilder, 8 Tab. 2011. ISBN 978-3-87525-320-7.

Band 223: Daniel Craiovan
Prozesse und Systemlösungen für die SMT-Montage optischer Bauelemente auf Substrate mit integrierten Lichtwellenleitern
FAPS, 165 Seiten, 85 Bilder, 8 Tab. 2011. ISBN 978-3-87525-324-5.

Band 224: Kay Wagner
Beanspruchungsangepasste Kaltmassivumformwerkzeuge durch lokal optimierte Werkzeugoberflächen
LFT, 147 Seiten, 103 Bilder, 17 Tab. 2011. ISBN 978-3-87525-325-2.

Band 225: Martin Brandhuber
Verbesserung der Prognosegüte des Versagens von Punktschweißverbindungen bei höchstfesten Stahlgüten
LFT, 155 Seiten, 91 Bilder, 19 Tab. 2011. ISBN 978-3-87525-327-6.

Band 226: Peter Sebastian Feuser
Ein Ansatz zur Herstellung von pressgehärteten Karosseriekomponenten mit maßgeschneiderten mechanischen Eigenschaften: Temperierte Umformwerkzeuge. Prozessfenster, Prozesssimuation und funktionale Untersuchung
LFT, 195 Seiten, 97 Bilder, 60 Tab. 2012. ISBN 978-3-87525-328-3.

Band 227: Murat Arbak
Material Adapted Design of Cold Forging Tools Exemplified by Powder Metallurgical Tool Steels and Ceramics
LFT, 109 Seiten, 56 Bilder, 8 Tab. 2012. ISBN 978-3-87525-330-6.

Band 228: Indra Pitz
Beschleunigte Simulation des Laserstrahlumformens von Aluminiumblechen
LPT, 137 Seiten, 45 Bilder, 27 Tab. 2012. ISBN 978-3-87525-333-7.

Band 229: Alexander Grimm
Prozessanalyse und -überwachung des Laserstrahlhartlötens mittels optischer Sensorik
LPT, 125 Seiten, 61 Bilder, 5 Tab. 2012. ISBN 978-3-87525-334-4.

Band 230: Markus Kaupper
Biegen von höhenfesten Stahlblechwerkstoffen - Umformverhalten und Grenzen der Biegbarkeit
LFT, 160 Seiten, 57 Bilder, 10 Tab. 2012. ISBN 978-3-87525-339-9.

Band 231: Thomas Kroiß
Modellbasierte Prozessauslegung für die Kaltmassivumformung unter Brücksichtigung der Werkzeug- und Pressenauffederung
LFT, 169 Seiten, 50 Bilder, 19 Tab. 2012. ISBN 978-3-87525-341-2.

Band 232: Christian Goth
Analyse und Optimierung der Entwicklung und Zuverlässigkeit räumlicher Schaltungsträger (3D-MID)
FAPS, 176 Seiten, 102 Bilder, 22 Tab. 2012.
ISBN 978-3-87525-340-5.

Band 233: Christian Ziegler
Ganzheitliche Automatisierung mechatronischer Systeme in der Medizin am Beispiel Strahlentherapie
FAPS, 170 Seiten, 71 Bilder, 19 Tab. 2012. ISBN 978-3-87525-342-9.

Band 234: Florian Albert
Automatisiertes Laserstrahllöten und -reparaturlöten elektronischer Baugruppen
LPT, 127 Seiten, 78 Bilder, 11 Tab. 2012. ISBN 978-3-87525-344-3.

Band 235: Thomas Stöhr
Analyse und Beschreibung des mechanischen Werkstoffverhaltens von presshärtbaren Bor-Manganstählen
LFT, 118 Seiten, 74 Bilder, 18 Tab. 2013. ISBN 978-3-87525-346-7.

Band 236: Christian Kägeler
Prozessdynamik beim Laserstrahlschweißen verzinkter Stahlbleche im Überlappstoß
LPT, 145 Seiten, 80 Bilder, 3 Tab. 2013. ISBN 978-3-87525-347-4.

Band 237: Andreas Sulzberger
Seriennahe Auslegung der Prozesskette zur wärmeunterstützten Umformung von Aluminiumblechwerkstoffen
LFT, 153 Seiten, 87 Bilder, 17 Tab. 2013. ISBN 978-3-87525-349-8.

Band 238: Simon Opel
Herstellung prozessangepasster Halbzeuge mit variabler Blechdicke durch die Anwendung von Verfahren der Blechmassivumformung
LFT, 165 Seiten, 108 Bilder, 27 Tab. 2013. ISBN 978-3-87525-350-4.

Band 239: Rajesh Kanawade
In-vivo Monitoring of Epithelium Vessel and Capillary Density for the Application of Detection of Clinical Shock and Early Signs of Cancer Development
LPT, 124 Seiten, 58 Bilder, 15 Tab. 2013. ISBN 978-3-87525-351-1.

Band 240: Stephan Busse
Entwicklung und Qualifizierung eines Schneidclinchverfahrens
LFT, 119 Seiten, 86 Bilder, 20 Tab. 2013. ISBN 978-3-87525-352-8.

Band 241: Karl-Heinz Leitz
Mikro- und Nanostrukturierung mit kurz und ultrakurz gepulster Laserstrahlung
LPT, 154 Seiten, 71 Bilder, 9 Tab. 2013. ISBN 978-3-87525-355-9.

Band 242: Markus Michl
Webbasierte Ansätze zur ganzheitlichen technischen Diagnose
FAPS, 182 Seiten, 62 Bilder, 20 Tab. 2013.
ISBN 978-3-87525-356-6.

Band 243: Vera Sturm
Einfluss von Chargenschwankungen auf die Verarbeitungsgrenzen von Stahlwerkstoffen
LFT, 113 Seiten, 58 Bilder, 9 Tab. 2013. ISBN 978-3-87525-357-3.

Band 244: Christian Neudel
Mikrostrukturelle und mechanisch-technologische Eigenschaften widerstandspunktgeschweißter Aluminium-Stahl-Verbindungen für den Fahrzeugbau
LFT, 178 Seiten, 171 Bilder, 31 Tab. 2014. ISBN 978-3-87525-358-0.

Band 245: Anja Neumann
Konzept zur Beherrschung der Prozessschwankungen im Presswerk
LFT, 162 Seiten, 68 Bilder, 15 Tab. 2014. ISBN 978-3-87525-360-3.

Band 246: Ulf-Hermann Quentin
Laserbasierte Nanostrukturierung mit optisch positionierten Mikrolinsen
LPT, 137 Seiten, 89 Bilder, 6 Tab. 2014. ISBN 978-3-87525-361-0.

Band 247: Erik Lamprecht
Der Einfluss der Fertigungsverfahren auf die Wirbelstromverluste von Stator-Einzelzahnblechpaketen für den Einsatz in Hybrid- und Elektrofahrzeugen
FAPS, 148 Seiten, 138 Bilder, 4 Tab. 2014. ISBN 978-3-87525-362-7.

Band 248: Sebastian Rösel
Wirkmedienbasierte Umformung von Blechhalbzeugen unter Anwendung magnetorheologischer Flüssigkeiten als kombiniertes Wirk- und Dichtmedium
LFT, 148 Seiten, 61 Bilder, 12 Tab. 2014. ISBN 978-3-87525-363-4.

Band 249: Paul Hippchen
Simulative Prognose der Geometrie indirekt pressgehärteter Karosseriebauteile für die industrielle Anwendung
LFT, 163 Seiten, 89 Bilder, 12 Tab. 2014. ISBN 978-3-87525-364-1.

Band 250: Martin Zubeil
Versagensprognose bei der Prozesssimulation von Biegeumform- und Falzverfahren
LFT, 171 Seiten, 90 Bilder, 5 Tab. 2014. ISBN 978-3-87525-365-8.

Band 251: Alexander Kühl
Flexible Automatisierung der Statorenmontage mit Hilfe einer universellen ambidexteren Kinematik
FAPS, 142 Seiten, 60 Bilder, 26 Tab. 2014.
ISBN 978-3-87525-367-2.

Band 252: Thomas Albrecht
Optimierte Fertigungstechnologien für Rotoren getriebeintegrierter PM-Synchronmotoren von Hybridfahrzeugen
FAPS, 198 Seiten, 130 Bilder, 38 Tab. 2014.
ISBN 978-3-87525-368-9.

Band 253: Florian Risch
Planning and Production Concepts for Contactless Power Transfer Systems for Electric Vehicles
FAPS, 185 Seiten, 125 Bilder, 13 Tab. 2014.
ISBN 978-3-87525-369-6.

Band 254: Markus Weigl
Laserstrahlschweißen von Mischverbindungen aus austenitischen und ferritischen korrosionsbeständigen Stahlwerkstoffen
LPT, 184 Seiten, 110 Bilder, 6 Tab. 2014. ISBN 978-3-87525-370-2.

Band 255: Johannes Noneder
Beanspruchungserfassung für die Validierung von FE-Modellen zur Auslegung von Massivumformwerkzeugen
LFT, 161 Seiten, 65 Bilder, 14 Tab. 2014. ISBN 978-3-87525-371-9.

Band 256: Andreas Reinhardt
Ressourceneffiziente Prozess- und Produktionstechnologie für flexible Schaltungsträger
FAPS, 123 Seiten, 69 Bilder, 19 Tab. 2014. ISBN 978-3-87525-373-3.

Band 257: Tobias Schmuck
Ein Beitrag zur effizienten Gestaltung globaler Produktions- und Logistiknetzwerke mittels Simulation
FAPS, 151 Seiten, 74 Bilder. 2014.
ISBN 978-3-87525-374-0.

Band 258: Bernd Eichenhüller
Untersuchungen der Effekte und Wechselwirkungen charakteristischer Einflussgrößen auf das Umformverhalten bei Mikroumformprozessen
LFT, 127 Seiten, 29 Bilder, 9 Tab. 2014. ISBN 978-3-87525-375-7.

Band 259: Felix Lütteke
Vielseitiges autonomes Transportsystem basierend auf Weltmodellerstellung mittels Datenfusion von Deckenkameras und Fahrzeugsensoren
FAPS, 152 Seiten, 54 Bilder, 20 Tab. 2014.
ISBN 978-3-87525-376-4.

Band 260: Martin Grüner
Hochdruck-Blechumformung mit formlos festen Stoffen als Wirkmedium
LFT, 144 Seiten, 66 Bilder, 29 Tab. 2014. ISBN 978-3-87525-379-5.

Band 261: Christian Brock
Analyse und Regelung des Laserstrahltiefschweißprozesses durch Detektion der Metalldampffackelposition
LPT, 126 Seiten, 65 Bilder, 3 Tab. 2015. ISBN 978-3-87525-380-1.

Band 262: Peter Vatter
Sensitivitätsanalyse des 3-Rollen-Schubbiegens auf Basis der Finite Elemente Methode
LFT, 145 Seiten, 57 Bilder, 26 Tab. 2015. ISBN 978-3-87525-381-8.

Band 263: Florian Klämpfl
Planung von Laserbestrahlungen durch simulationsbasierte Optimierung
LPT, 169 Seiten, 78 Bilder, 32 Tab. 2015. ISBN 978-3-87525-384-9.

Band 264: Matthias Domke
Transiente physikalische Mechanismen bei der Laserablation von dünnen Metallschichten
LPT, 133 Seiten, 43 Bilder, 3 Tab.
2015. ISBN 978-3-87525-385-6.

Band 265: Johannes Götz
Community-basierte Optimierung des Anlagenengineerings
FAPS, 177 Seiten, 80 Bilder, 30 Tab.
2015.
ISBN 978-3-87525-386-3.

Band 266: Hung Nguyen
Qualifizierung des Potentials von Verfestigungseffekten zur Erweiterung des Umformvermögens aushärtbarer Aluminiumlegierungen
LFT, 137 Seiten, 57 Bilder, 16 Tab.
2015. ISBN 978-3-87525-387-0.

Band 267: Andreas Kuppert
Erweiterung und Verbesserung von Versuchs- und Auswertetechniken für die Bestimmung von Grenzformänderungskurven
LFT, 138 Seiten, 82 Bilder, 2 Tab.
2015. ISBN 978-3-87525-388-7.

Band 268: Kathleen Klaus
Erstellung eines Werkstofforientierten Fertigungsprozessfensters zur Steigerung des Formgebungsvermögens von Alumi-niumlegierungen unter Anwendung einer zwischengeschalteten Wärmebehandlung
LFT, 154 Seiten, 70 Bilder, 8 Tab.
2015. ISBN 978-3-87525-391-7.

Band 269: Thomas Svec
Untersuchungen zur Herstellung von funktionsoptimierten Bauteilen im partiellen Presshärtprozess mittels lokal unterschiedlich temperierter Werkzeuge
LFT, 166 Seiten, 87 Bilder, 15 Tab.
2015. ISBN 978-3-87525-392-4.

Band 270: Tobias Schrader
Grundlegende Untersuchungen zur Verschleißcharakterisierung beschichteter Kaltmassivumformwerkzeuge
LFT, 164 Seiten, 55 Bilder, 11 Tab.
2015. ISBN 978-3-87525-393-1.

Band 271: Matthäus Brela
Untersuchung von Magnetfeld-Messmethoden zur ganzheitlichen Wertschöpfungsoptimierung und Fehlerdetektion an magnetischen Aktoren
FAPS, 170 Seiten, 97 Bilder, 4 Tab.
2015. ISBN 978-3-87525-394-8.

Band 272: Michael Wieland
Entwicklung einer Methode zur Prognose adhäsiven Verschleißes an Werkzeugen für das direkte Presshärten
LFT, 156 Seiten, 84 Bilder, 9 Tab.
2015. ISBN 978-3-87525-395-5.

Band 273: René Schramm
Strukturierte additive Metallisierung durch kaltaktives Atmosphärendruckplasma
FAPS, 136 Seiten, 62 Bilder, 15 Tab.
2015. ISBN 978-3-87525-396-2.

Band 274: Michael Lechner
Herstellung beanspruchungsangepasster Aluminiumblechhalbzeuge durch eine maßgeschneiderte Variation der Abkühlgeschwindigkeit nach Lösungsglühen
LFT, 136 Seiten, 62 Bilder, 15 Tab.
2015. ISBN 978-3-87525-397-9.

Band 275: Kolja Andreas
Einfluss der Oberflächenbeschaffenheit auf das Werkzeugeinsatzverhalten beim Kaltfließpressen
LFT, 169 Seiten, 76 Bilder, 4 Tab.
2015. ISBN 978-3-87525-398-6.

Band 276: Marcus Baum
Laser Consolidation of ITO Nanoparticles for the Generation of Thin Conductive Layers on Transparent Substrates
LPT, 158 Seiten, 75 Bilder, 3 Tab.
2015. ISBN 978-3-87525-399-3.

Band 277: Thomas Schneider
Umformtechnische Herstellung dünnwandiger Funktionsbauteile aus Feinblech durch Verfahren der Blechmassivumformung
LFT, 188 Seiten, 95 Bilder, 7 Tab.
2015. ISBN 978-3-87525-401-3.

Band 278: Jochen Merhof
Sematische Modellierung automatisierter Produktionssysteme zur Verbesserung der IT-Integration zwischen Anlagen-Engineering und Steuerungsebene
FAPS, 157 Seiten, 88 Bilder, 8 Tab.
2015. ISBN 978-3-87525-402-0.

Band 279: Fabian Zöller
Erarbeitung von Grundlagen zur Abbildung des tribologischen Systems in der Umformsimulation
LFT, 126 Seiten, 51 Bilder, 3 Tab.
2016. ISBN 978-3-87525-403-7.

Band 280: Christian Hezler
Einsatz technologischer Versuche zur Erweiterung der Versagensvorhersage bei Karosseriebauteilen aus höchstfesten Stählen
LFT, 147 Seiten, 63 Bilder, 44 Tab.
2016. ISBN 978-3-87525-404-4.

Band 281: Jochen Bönig
Integration des Systemverhaltens von Automobil-Hochvoltleitungen in die virtuelle Absicherung durch strukturmechanische Simulation
FAPS, 177 Seiten, 107 Bilder, 17 Tab.
2016.
ISBN 978-3-87525-405-1.

Band 282: Johannes Kohl
Automatisierte Datenerfassung für diskret ereignisorientierte Simulationen in der energieflexibelen Fabrik
FAPS, 160 Seiten, 80 Bilder, 27 Tab.
2016.
ISBN 978-3-87525-406-8.

Band 283: Peter Bechtold
Mikroschockwellenumformung mittels ultrakurzer Laserpulse
LPT, 155 Seiten, 59 Bilder, 10 Tab.
2016. ISBN 978-3-87525-407-5.

Band 284: Stefan Berger
Laserstrahlschweißen thermoplastischer Kohlenstofffaserverbundwerkstoffe mit spezifischem Zusatzdraht
LPT, 118 Seiten, 68 Bilder, 9 Tab.
2016. ISBN 978-3-87525-408-2.

Band 285: Martin Bornschlegl
Methods-Energy Measurement - Eine Methode zur Energieplanung für Fügeverfahren im Karosseriebau
FAPS, 136 Seiten, 72 Bilder, 46 Tab. 2016.
ISBN 978-3-87525-409-9.

Band 286: Tobias Rackow
Erweiterung des Unternehmenscontrollings um die Dimension Energie
FAPS, 164 Seiten, 82 Bilder, 29 Tab. 2016.
ISBN 978-3-87525-410-5.

Band 287: Johannes Koch
Grundlegende Untersuchungen zur Herstellung zyklisch-symmetrischer Bauteile mit Nebenformelementen durch Blechmassivumformung
LFT, 125 Seiten, 49 Bilder, 17 Tab. 2016. ISBN 978-3-87525-411-2.

Band 288: Hans Ulrich Vierzigmann
Beitrag zur Untersuchung der tribologischen Bedingungen in der Blechmassivumformung - Bereitstellung von tribologischen Modellversuchen und Realisierung von Tailored Surfaces
LFT, 174 Seiten, 102 Bilder, 34 Tab. 2016. ISBN 978-3-87525-412-9.

Band 289: Thomas Senner
Methodik zur virtuellen Absicherung der formgebenden Operation des Nasspressprozesses von Gelege-Mehrschichtverbunden
LFT, 156 Seiten, 96 Bilder, 21 Tab. 2016. ISBN 978-3-87525-414-3.

Band 290: Sven Kreitlein
Der grundoperationsspezifische Mindestenergiebedarf als Referenzwert zur Bewertung der Energieeffizienz in der Produktion
FAPS, 185 Seiten, 64 Bilder, 30 Tab. 2016.
ISBN 978-3-87525-415-0.

Band 291: Christian Roos
Remote-Laserstrahlschweißen verzinkter Stahlbleche in Kehlnahtgeometrie
LPT, 123 Seiten, 52 Bilder, 0 Tab. 2016. ISBN 978-3-87525-416-7.

Band 292: Alexander Kahrimanidis
Thermisch unterstützte Umformung von Aluminiumblechen
LFT, 165 Seiten, 103 Bilder, 18 Tab. 2016. ISBN 978-3-87525-417-4.

Band 293: Jan Tremel
Flexible Systems for Permanent Magnet Assembly and Magnetic Rotor Measurement / Flexible Systeme zur Montage von Permanentmagneten und zur Messung magnetischer Rotoren
FAPS, 152 Seiten, 91 Bilder, 12 Tab. 2016. ISBN 978-3-87525-419-8.

Band 294: Ioannis Tsoupis
Schädigungs- und Versagensverhalten hochfester Leichtbauwerkstoffe unter Biegebeanspruchung
LFT, 176 Seiten, 51 Bilder, 6 Tab. 2017. ISBN 978-3-87525-420-4.

Band 295: Sven Hildering
Grundlegende Untersuchungen zum Prozessverhalten von Silizium als Werkzeugwerkstoff für das Mikroscherschneiden metallischer Folien
LFT, 177 Seiten, 74 Bilder, 17 Tab. 2017. ISBN 978-3-87525-422-8.

Band 296: Sasia Mareike Hertweck
Zeitliche Pulsformung in der Lasermikromaterialbearbeitung – Grundlegende Untersuchungen und Anwendungen
LPT, 146 Seiten, 67 Bilder, 5 Tab. 2017. ISBN 978-3-87525-423-5.

Band 297: Paryanto
Mechatronic Simulation Approach for the Process Planning of Energy-Efficient Handling Systems
FAPS, 162 Seiten, 86 Bilder, 13 Tab. 2017. ISBN 978-3-87525-424-2.

Band 298: Peer Stenzel
Großserientaugliche Nadelwickeltechnik für verteilte Wicklungen im Anwendungsfall der E-Traktionsantriebe
FAPS, 239 Seiten, 147 Bilder, 20 Tab. 2017.
ISBN 978-3-87525-425-9.

Band 299: Mario Lušić
Ein Vorgehensmodell zur Erstellung montageführender Werkerinformationssysteme simultan zum Produktentstehungsprozess
FAPS, 174 Seiten, 79 Bilder, 22 Tab. 2017.
ISBN 978-3-87525-426-6.

Band 300: Arnd Buschhaus
Hochpräzise adaptive Steuerung und Regelung robotergeführter Prozesse
FAPS, 202 Seiten, 96 Bilder, 4 Tab. 2017. ISBN 978-3-87525-427-3.

Band 301: Tobias Laumer
Erzeugung von thermoplastischen Werkstoffverbunden mittels simultanem, intensitätsselektivem Laserstrahlschmelzen
LPT, 140 Seiten, 82 Bilder, 0 Tab. 2017. ISBN 978-3-87525-428-0.

Band 302: Nora Unger
Untersuchung einer thermisch unterstützten Fertigungskette zur Herstellung umgeformter Bauteile aus der höherfesten Aluminiumlegierung EN AW-7020
LFT, 142 Seiten, 53 Bilder, 8 Tab. 2017. ISBN 978-3-87525-429-7.

Band 303: Tommaso Stellin
Design of Manufacturing Processes for the Cold Bulk Forming of Small Metal Components from Metal Strip
LFT, 146 Seiten, 67 Bilder, 7 Tab. 2017. ISBN 978-3-87525-430-3.

Band 304: Bassim Bachy
Experimental Investigation, Modeling, Simulation and Optimization of Molded Interconnect Devices (MID) Based on Laser Direct Structuring (LDS) / Experimentelle Untersuchung, Modellierung, Simulation und Optimierung von Molded Interconnect Devices (MID) basierend auf Laser Direktstrukturierung (LDS)
FAPS, 168 Seiten, 120 Bilder, 26 Tab. 2017.
ISBN 978-3-87525-431-0.

Band 305: Michael Spahr
Automatisierte Kontaktierungsverfahren für flachleiterbasierte Pkw-Bordnetzsysteme
FAPS, 197 Seiten, 98 Bilder, 17 Tab. 2017. ISBN 978-3-87525-432-7.

Band 306: Sebastian Suttner
Charakterisierung und Modellierung des spannungszustandsabhängigen Werkstoffverhaltens der Magnesiumlegierung AZ31B für die numerische Prozessauslegung
LFT, 150 Seiten, 84 Bilder, 19 Tab. 2017. ISBN 978-3-87525-433-4.

Band 307: Bhargav Potdar
A reliable methodology to deduce thermo-mechanical flow behaviour of hot stamping steels
LFT, 203 Seiten, 98 Bilder, 27 Tab. 2017. ISBN 978-3-87525-436-5.

Band 308: Maria Löffler
Steuerung von Blechmassivumformprozessen durch maßgeschneiderte tribologische Systeme
LFT, viii u. 166 Seiten, 90 Bilder, 5 Tab. 2018. ISBN 978-3-96147-133-1.

Band 309: Martin Müller
Untersuchung des kombinierten Trenn- und Umformprozesses beim Fügen artungleicher Werkstoffe mittels Schneidclinchverfahren
LFT, xi u. 149 Seiten, 89 Bilder, 6 Tab. 2018.
ISBN: 978-3-96147-135-5.

Band 310: Christopher Kästle
Qualifizierung der Kupfer-Drahtbondtechnologie für integrierte Leistungsmodule in harschen Umgebungsbedingungen
FAPS, xii u. 167 Seiten, 70 Bilder, 18 Tab. 2018.
ISBN 978-3-96147-145-4.

Band 311: Daniel Vipavc
Eine Simulationsmethode für das 3-Rollen-Schubbiegen
LFT, xiii u. 121 Seiten, 56 Bilder, 17 Tab. 2018. ISBN 978-3-96147-147-8.

Band 312: Christina Ramer
Arbeitsraumüberwachung und autonome Bahnplanung für ein sicheres und flexibles Roboter-Assistenzsystem in der Fertigung
FAPS, xiv u. 188 Seiten, 57 Bilder, 9 Tab. 2018.
ISBN 978-3-96147-153-9.

Band 313: Miriam Rauer
Der Einfluss von Poren auf die Zuverlässigkeit der Lötverbindungen von Hochleistungs-Leuchtdioden
FAPS, xii u. 209 Seiten, 108 Bilder, 21 Tab. 2018.
ISBN 978-3-96147-157-7.

Band 314: Felix Tenner
Kamerabasierte Untersuchungen der Schmelze und Gasströmungen beim Laserstrahlschweißen verzinkter Stahlbleche
LPT, xxiii u. 184 Seiten, 94 Bilder, 7 Tab. 2018.
ISBN 978-3-96147-160-7.

Band 315: Aarief Syed-Khaja
Diffusion Soldering for High-temperature Packaging of Power Electronics
FAPS, x u. 202 Seiten, 144 Bilder, 32 Tab. 2018.
ISBN 978-3-87525-162-1.

Band 316: Adam Schaub
Grundlagenwissenschaftliche Untersuchung der kombinierten Prozesskette aus Umformen und Additive Fertigung
LFT, xi u. 192 Seiten, 72 Bilder, 27 Tab. 2019.
ISBN 978-3-96147-166-9.

Band 317: Daniel Gröbel
Herstellung von Nebenformelementen unterschiedlicher Geometrie an Blechen mittels Fließpressverfahren der Blechmassivumformung
LFT, x u. 165 Seiten, 96 Bilder, 13 Tab. 2019. ISBN 978-3-96147-168-3.

Band 318: Philipp Hildenbrand
Entwicklung einer Methodik zur Herstellung von Tailored Blanks mit definierten Halbzeugeigenschaften durch einen Taumelprozess
LFT, ix u. 153 Seiten, 77 Bilder, 4 Tab. 2019. ISBN 978-3-96147-174-4.

Band 319: Tobias Konrad
Simulative Auslegung der Spann- und Fixierkonzepte im Karosserierohbau: Bewertung der Baugruppenmaßhaltigkeit unter Berücksichtigung schwankender Einflussgrößen
LFT, x u. 203 Seiten, 134 Bilder, 32 Tab. 2019.
ISBN 978-3-96147-176-8.

Band 320: David Meinel
Architektur applikationsspezifischer Multi-Physics-Simulationskonfiguratoren am Beispiel modularer Triebzüge
FAPS, xii u. 166 Seiten, 82 Bilder, 25 Tab. 2019.
ISBN 978-3-96147-184-3.

Band 321: Andrea Zimmermann
Grundlegende Untersuchungen zum Einfluss fertigungsbedingter Eigenschaften auf die Ermüdungsfestigkeit kaltmassivumgeformter Bauteile
LFT, ix u. 160 Seiten, 66 Bilder, 5 Tab. 2019.
ISBN 978-3-96147-190-4.

Band 322: Christoph Amann
Simulative Prognose der Geometrie nassgepresster Karosseriebauteile aus Gelege-Mehrschichtverbunden
LFT, xvi u. 169 Seiten, 80 Bilder, 13 Tab. 2019.
ISBN 978-3-96147-194-2.

Band 323: Jennifer Tenner
Realisierung schmierstofffreier Tiefziehprozesse durch maßgeschneiderte Werkzeugoberflächen
LFT, x u. 187 Seiten, 68 Bilder, 13 Tab. 2019.
ISBN 978-3-96147-196-6.

Band 324: Susan Zöller
Mapping Individual Subjective Values to Product Design
KTmfk, xi u. 223 Seiten, 81 Bilder, 25 Tab. 2019.
ISBN 978-3-96147-202-4.

Band 325: Stefan Lutz
Erarbeitung einer Methodik zur semiempirischen Ermittlung der Umwandlungskinetik durchhärtender Wälzlagerstähle für die Wärmebehandlungssimulation
LFT, xiv u. 189 Seiten, 75 Bilder, 32 Tab. 2019.
ISBN 978-3-96147-209-3.

Band 326: Tobias Gnibl
Modellbasierte Prozesskettenabbildung rührreibgeschweißter Aluminiumhalbzeuge zur umformtechnischen Herstellung höchstfester Leichtbau-strukturteile
LFT, xii u. 167 Seiten, 68 Bilder, 17 Tab. 2019.
ISBN 978-3-96147-217-8.

Band 327: Johannes Bürner
Technisch-wirtschaftliche Optionen zur Lastflexibilisierung durch intelligente elektrische Wärmespeicher
FAPS, xiv u. 233 Seiten, 89 Bilder, 27 Tab. 2019.
ISBN 978-3-96147-219-2.

Band 328: Wolfgang Böhm
Verbesserung des Umformverhaltens von mehrlagigen Aluminiumblechwerkstoffen mit ultrafeinkörnigem Gefüge
LFT, ix u. 160 Seiten, 88 Bilder, 14 Tab. 2019.
ISBN 978-3-96147-227-7.

Band 329: Stefan Landkammer
Grundsatzuntersuchungen, mathematische Modellierung und Ableitung einer Auslegungsmethodik für Gelenkantriebe nach dem Spinnenbeinprinzip
LFT, xii u. 200 Seiten, 83 Bilder, 13 Tab. 2019.
ISBN 978-3-96147-229-1.

Band 330: Stephan Rapp
Pump-Probe-Ellipsometrie zur Messung transienter optischer Materialeigen-schaften bei der Ultrakurzpuls-Lasermaterialbearbeitung
LPT, xi u. 143 Seiten, 49 Bilder, 2 Tab. 2019.
ISBN 978-3-96147-235-2.

Band 331: Michael Scholz
Intralogistics Execution System mit integrierten autonomen, servicebasierten Transportentitäten
FAPS, xi u. 195 Seiten, 55 Bilder, 11 Tab. 2019.
ISBN 978-3-96147-237-6.

Band 332: Eva Bogner
Strategien der Produktindividualisierung in der produzierenden Industrie im Kontext der Digitalisierung
FAPS, ix u. 201 Seiten, 55 Bilder, 28 Tab. 2019.
ISBN 978-3-96147-246-8.

Band 333: Daniel Benjamin Krüger
Ein Ansatz zur CAD-integrierten muskuloskelettalen Analyse der Mensch-Maschine-Interaktion
KTmfk, x u. 217 Seiten, 102 Bilder, 7 Tab. 2019.
ISBN 978-3-96147-250-5.

Band 334: Thomas Kuhn
Qualität und Zuverlässigkeit laserdirektstrukturierter mechatronisch integrierter Baugruppen (LDS-MID)
FAPS, ix u. 152 Seiten, 69 Bilder, 12 Tab. 2019.
ISBN: 978-3-96147-252-9.

Band 335: Hans Fleischmann
Modellbasierte Zustands- und Prozessüberwachung auf Basis sozio-cyber-physischer Systeme
FAPS, xi u. 214 Seiten, 111 Bilder, 18 Tab. 2019.
ISBN: 978-3-96147-256-7.

Band 336: Markus Michalski
Grundlegende Untersuchungen zum Prozess- und Werkstoffverhalten bei schwingungsüberlagerter Umformung
LFT, xii u. 197 Seiten, 93 Bilder, 11 Tab. 2019.
ISBN: 978-3-96147-270-3.

Band 337: Markus Brandmeier
Ganzheitliches ontologiebasiertes Wissensmanagement im Umfeld der industriellen Produktion
FAPS, xi u. 255 Seiten, 77 Bilder, 33 Tab. 2020.
ISBN: 978-3-96147-275-8.

Band 338: Stephan Purr
Datenerfassung für die Anwendung lernender Algorithmen bei der Herstellung von Blechformteilen
LFT, ix u. 165 Seiten, 48 Bilder, 4 Tab. 2020.
ISBN: 978-3-96147-281-9.

Band 339: Christoph Kiener
Kaltfließpressen von gerad- und schrägverzahnten Zahnrädern
LFT, viii u. 151 Seiten, 81 Bilder, 3 Tab. 2020.
ISBN 978-3-96147-287-1.

Band 340: Simon Spreng
Numerische, analytische und empirische Modellierung des Heißcrimpprozesses
FAPS, xix u. 204 Seiten, 91 Bilder, 27 Tab. 2020.
ISBN 978-3-96147-293-2.

Band 341: Patrik Schwingenschlögl
Erarbeitung eines Prozessverständnisses zur Verbesserung der tribologischen Bedingungen beim Presshärten
LFT, x u. 177 Seiten, 81 Bilder, 8 Tab. 2020.
ISBN 978-3-96147-297-0.

Band 342: Emanuela Affronti
Evaluation of failure behaviour of sheet metals
LFT, ix u. 136 Seiten, 57 Bilder, 20 Tab. 2020.
ISBN 978-3-96147-303-8.

Band 343: Julia Degner
Grundlegende Untersuchungen zur Herstellung hochfester Aluminiumblechbauteile in einem kombinierten Umform- und Abschreckprozess
LFT, x u. 172 Seiten, 61 Bilder, 9 Tab. 2020.
ISBN 978-3-96147-307-6.

Band 344: Maximilian Wagner
Automatische Bahnplanung für die Aufteilung von Prozessbewegungen in synchrone Werkstück- und Werkzeugbewegungen mittels Multi-Roboter-Systemen
FAPS, xxi u. 181 Seiten, 111 Bilder, 15 Tab. 2020.
ISBN 978-3-96147-309-0.

Band 345: Stefan Härter
Qualifizierung des Montageprozesses hochminiaturisierter elektronischer Bauelemente
FAPS, ix u. 194 Seiten, 97 Bilder, 28 Tab. 2020.
ISBN 978-3-96147-314-4.

Band 346: Toni Donhauser
Ressourcenorientierte Auftragsregelung in einer hybriden Produktion mittels betriebsbegleitender Simulation
FAPS, xix u. 242 Seiten, 97 Bilder, 17 Tab. 2020.
ISBN 978-3-96147-316-8.

Band 347: Philipp Amend
Laserbasiertes Schmelzkleben von Thermoplasten mit Metallen
LPT, xv u. 154 Seiten, 67 Bilder. 2020. ISBN 978-3-96147-326-7.

Band 348: Matthias Ehlert
Simulationsunterstützte funktionale Grenzlagenabsicherung
KTmfk, xvi u. 300 Seiten, 101 Bilder, 73 Tab. 2020.
ISBN 978-3-96147-328-1.

Band 349: Thomas Sander
Ein Beitrag zur Charakterisierung und Auslegung des Verbundes von Kunststoffsubstraten mit harten Dünnschichten
KTmfk, xiv u. 178 Seiten, 88 Bilder, 21 Tab. 2020.
ISBN 978-3-96147-330-4.

Band 350: Florian Pilz
Fließpressen von Verzahnungselementen an Blechen
LFT, x u. 170 Seiten, 103Bilder, 4 Tab. 2020.
ISBN 978-3-96147-332-8.

Band 351: Sebastian Josef Katona
Evaluation und Aufbereitung von Produktsimulationen mittels abweichungsbehafteter Geometriemodelle
KTmfk, ix u. 147 Seiten, 73 Bilder, 11 Tab. 2020.
ISBN 978-3-96147-336-6.

Band 352: Jürgen Herrmann
Kumulatives Walzplattieren. Bewertung der Umformeigenschaften mehrlagiger Blechwerkstoffe der ausscheidungshärtbaren Legierung AA6014
LFT, x u. 157 Seiten, 64 Bilder, 5 Tab. 2020.
ISBN 978-3-96147-344-1.

Band 353: Christof Küstner
Assistenzsystem zur Unterstützung der datengetriebenen Produktentwicklung
KTmfk, xii u. 219 Seiten, 63 Bilder, 14 Tab. 2020.
ISBN 978-3-96147-348-9.

Band 354: Tobias Gläßel
Prozessketten zum Laserstrahlschweißen von flachleiterbasierten Formspulenwicklungen für automobile Traktionsantriebe
FAPS, xiv u. 206 Seiten, 89 Bilder, 11 Tab. 2020.
ISBN 978-3-96147-356-4.

Band 355: Andreas Meinel
Experimentelle Untersuchung der Auswirkungen von Axialschwingungen auf Reibung und Verschleiß in Zylinderrol-lenlagern
KTmfk, xii u. 162 Seiten, 56 Bilder, 7 Tab. 2020.
ISBN 978-3-96147-358-8.

Band 356: Hannah Riedle
Haptische, generische Modelle weicher anatomischer Strukturen für die chirurgische Simulation
FAPS, xxx u. 179 Seiten, 82 Bilder, 35 Tab. 2020.
ISBN 978-3-96147-367-0.

Band 357: Maximilian Landgraf
Leistungselektronik für den Einsatz dielektrischer Elastomere in aktorischen, sensorischen und integrierten sensomotorischen Systemen
FAPS, xxiii u. 166 Seiten, 71 Bilder, 10 Tab. 2020.
ISBN 978-3-96147-380-9.

Band 358: Alireza Esfandyari
Multi-Objective Process Optimization for Overpressure Reflow Soldering in Electronics Production
FAPS, xviii u. 175 Seiten, 57 Bilder, 23 Tab. 2020.
ISBN 978-3-96147-382-3.

Band 359: Christian Sand
Prozessübergreifende Analyse komplexer Montageprozessketten mittels Data Mining
FAPS, XV u. 168 Seiten, 61 Bilder, 12 Tab. 2021.
ISBN 978-3-96147-398-4.

Band 360: Ralf Merkl
Closed-Loop Control of a Storage-Supported Hybrid Compensation System for Improving the Power Quality in Medium Voltage Networks
FAPS, xxvii u. 200 Seiten, 102 Bilder, 2 Tab. 2021.
ISBN 978-3-96147-402-8.

Band 361: Thomas Reitberger
Additive Fertigung polymerer optischer Wellenleiter im Aerosol-Jet-Verfahren
FAPS, xix u. 141 Seiten, 65 Bilder, 11 Tab. 2021.
ISBN 978-3-96147-400-4.

Band 362: Marius Christian Fechter
Modellierung von Vorentwürfen in der virtuellen Realität mit natürlicher Fingerinteraktion
KTmfk, x u. 188 Seiten, 67 Bilder, 19 Tab. 2021.
ISBN 978-3-96147-404-2.

Band 363: Franziska Neubauer
Oberflächenmodifizierung und Entwicklung einer Auswertemethodik zur Verschleißcharakterisierung im Presshärteprozess
LFT, ix u. 177 Seiten, 42 Bilder, 6 Tab. 2021.
ISBN 978-3-96147-406-6.

Band 364: Eike Wolfram Schäffer
Web- und wissensbasierter Engineering-Konfigurator für roboterzentrierte Automatisierungslösungen
FAPS, xxiv u. 195 Seiten, 108 Bilder, 25 Tab. 2021.
ISBN 978-3-96147-410-3.

Band 365: Daniel Gross
Untersuchungen zur kohlenstoffdioxidbasierten kryogenen Minimalmengenschmierung
REP, xii u. 184 Seiten, 56 Bilder, 18 Tab. 2021.
ISBN 978-3-96147-412-7.

Band 366: Daniel Junker
Qualifizierung laser-additiv gefertigter Komponenten für den Einsatz im Werkzeugbau der Massivumformung
LFT, vii u. 142 Seiten, 62 Bilder, 5 Tab. 2021.
ISBN 978-3-96147-416-5.

Band 367: Tallal Javied
Totally Integrated Ecology Management for Resource Efficient and Eco-Friendly Production
FAPS, xv u. 160 Seiten, 60 Bilder, 13 Tab. 2021.
ISBN 978-3-96147-418-9.

Band 368: David Marco Hochrein
Wälzlager im Beschleunigungsfeld – Eine Analysestrategie zur Bestimmung des Reibungs-, Axialschub- und Temperaturverhaltens von Nadelkränzen –
KTmfk, xiii u. 279 Seiten, 108 Bilder, 39 Tab. 2021.
ISBN 978-3-96147-420-2.

Band 369: Daniel Gräf
Funktionalisierung technischer Oberflächen mittels prozessüberwachter aerosolbasierter Drucktechnologie
FAPS, xxii u. 175 Seiten, 97 Bilder, 6 Tab. 2021.
ISBN 978-3-96147-433-2.

Band 370: Andreas Gröschl
Hochfrequent fokusabstandsmodulierte Konfokalsensoren für die Nanokoordinatenmesstechnik
FMT, x u. 144 Seiten, 98 Bilder, 6 Tab. 2021.
ISBN 978-3-96147-435-6.

Band 371: Johann Tüchsen
Konzeption, Entwicklung und Einführung des Assistenzsystems D-DAS für die Produktentwicklung elektrischer Motoren
KTmfk, xii u. 178 Seiten, 92 Bilder, 12 Tab. 2021.
ISBN 978-3-96147-437-0.

Band 372: Max Marian
Numerische Auslegung von Oberflächenmikrotexturen für geschmierte tribologische Kontakte
KTmfk, xviii u. 276 Seiten, 85 Bilder, 45 Tab. 2021.
ISBN 978-3-96147-439-4.

Band 373: Johannes Strauß
Die akustooptische Strahlformung in der Lasermaterialbearbeitung
LPT, xvi u. 113 Seiten, 48 Bilder. 2021. ISBN 978-3-96147-441-7.

Band 374: Martin Hohmann
Machine learning and hyper spectral imaging: Multi Spectral Endoscopy in the Gastro Intestinal Tract towards Hyper Spectral Endoscopy
LPT, x u. 137 Seiten, 62 Bilder, 29 Tab. 2021.
ISBN 978-3-96147-445-5.

Band 375: Timo Kordaß
Lasergestütztes Verfahren zur selektiven Metallisierung von epoxidharzbasierten Duromeren zur Steigerung der Integrationsdichte für dreidimensionale mechatronische Package-Baugruppen
FAPS, xviii u. 198 Seiten, 92 Bilder, 24 Tab. 2021.
ISBN 978-3-96147-443-1.

Band 376: Philipp Kestel
Assistenzsystem für den wissensbasierten Aufbau konstruktionsbegleitender Finite-Elemente-Analysen
KTmfk, xviii u. 209 Seiten, 57 Bilder, 17 Tab. 2021.
ISBN 978-3-96147-457-8.

Band 377: Martin Lerchen
Messverfahren für die pulverbettbasierte additive Fertigung zur Sicherstellung der Konformität mit geometrischen Produktspezifikationen
FMT, x u. 150 Seiten, 60 Bilder, 9 Tab. 2021.
ISBN 978-3- 96147-463-9.

Band 378: Michael Schneider
Inline-Prüfung der Permeabilität in weichmagnetischen Komponenten
FAPS, xxii u. 189 Seiten, 79 Bilder, 14 Tab. 2021.
ISBN 978-3-96147-465-3.

Band 379: Tobias Sprügel
Sphärische Detektorflächen als Unterstützung der Produktentwicklung zur Datenanalyse im Rahmen des Digital Engineering
KTmfk, xiii u. 213 Seiten, 84 Bilder, 33 Tab. 2021.
ISBN 978-3-96147-475-2.

Band 380: Tom Häfner
Multipulseffekte beim Mikro-Materialabtrag von Stahllegierungen mit Pikosekunden-Laserpulsen
LPT, xxviii u. 159 Seiten, 57 Bilder, 13 Tab. 2021.
ISBN 978-3-96147-479-0.

Band 381: Björn Heling
Einsatz und Validierung virtueller Absicherungsmethoden für abweichungs-behaftete Mechanismen im Kontext des Robust Design
KTmfk, xi u. 169 Seiten, 63 Bilder, 27 Tab. 2021.
ISBN 978-3-96147-487-5.

Band 382: Tobias Kolb
Laserstrahl-Schmelzen von Metallen mit einer Serienanlage – Prozesscharakterisierung und Erweiterung eines Überwachungssystems
LPT, xv u. 170 Seiten, 128 Bilder, 16 Tab. 2021.
ISBN 978-3-96147-491-2.

Band 383: Mario Meinhardt
Widerstandselementschweißen mit gestauchten Hilfsfügeelementen - Umformtechnische Wirkzusammenhänge zur Beeinflussung der Verbindungsfestigkeit
LFT, xii u. 189 Seiten, 87 Bilder, 4 Tab. 2022.
ISBN 978-3-96147-473-8.

Band 384: Felix Bauer
Ein Beitrag zur digitalen Auslegung von Fügeprozessen im Karosseriebau mit Fokus auf das Remote-Laserstrahlschweißen unter Einsatz flexibler Spanntechnik
LFT, xi u. 185 Seiten, 74 Bilder, 12 Tab. 2022.
ISBN 978-3-96147-498-1.

Band 385: Jochen Zeitler
Konzeption eines rechnergestützten Konstruktionssystems für optomechatronische Baugruppen
FAPS, xix u. 172 Seiten, 88 Bilder, 11 Tab. 2022.
ISBN 978-3-96147-499-8.

Band 386: Vincent Mann
Einfluss von Strahloszillation auf das Laserstrahlschweißen hochfester Stähle
LPT, xiii u. 172 Seiten, 103 Bilder, 18 Tab. 2022.
ISBN 978-3-96147-503-2.

Band 387: Chen Chen
Skin-equivalent opto-/elastofluidic in-vitro microphysiological vascular models for translational studies of optical biopsies
LPT, xx u. 126 Seiten, 60 Bilder, 10 Tab. 2022.
ISBN 978-3-96147-505-6.

Band 388: Stefan Stein
Laser drop on demand joining as bonding method for electronics assembly and packaging with high thermal requirements
LPT, x u. 112 Seiten, 54 Bilder, 10 Tab. 2022.
ISBN 978-3-96147-507-0

Band 389: Nikolaus Urban
Untersuchung des Laserstrahlschmelzens von Neodym-Eisen-Bor zur additiven Herstellung von Permanentmagneten
FAPS, x u. 174 Seiten, 88 Bilder, 18 Tab. 2022.
ISBN 978-3-96147-501-8.

Band 390: Yiting Wu
Großflächige Topographiemessungen mit einem Weißlichtinterferenzmikroskop und einem metrologischen Rasterkraftmikroskop
FMT, xii u. 142 Seiten, 68 Bilder, 11 Tab. 2022.
ISBN: 978-3-96147-513-1.

Band 391: Thomas Papke
Untersuchungen zur Umformbarkeit hybrider Bauteile aus Blechgrundkörper und additiv gefertigter Struktur
LFT, xii u. 194 Seiten, 71 Bilder, 16 Tab. 2022.
ISBN 978-3-96147-515-5.

Band 392: Bastian Zimmermann
Einfluss des Vormaterials auf die mehrstufige Kaltumformung vom Draht
LFT, xi u. 182 Seiten, 36 Bilder, 6 Tab. 2022.
ISBN 978-3-96147-519-3.

Band 393: Harald Völkl
Ein simulationsbasierter Ansatz zur Auslegung additiv gefertigter FLM-Faserverbundstrukturen
KTmfk, xx u. 204 Seiten, 95 Bilder, 22 Tab. 2022.
ISBN 978-3-96147-523-0.

Band 394: Robert Schulte
Auslegung und Anwendung prozessangepasster Halbzeuge für Verfahren der Blechmassivumformung
LFT, x u. 163 Seiten, 93 Bilder, 5 Tab. 2022.
ISBN 978-3-96147-525-4.

Band 395: Philipp Frey
Umformtechnische Strukturierung metallischer Einleger im Folgeverbund für mediendichte Kunststoff-Metall-Hybridbauteile
LFT, ix u. 180 Seiten, 83 Bilder, 7 Tab. 2022.
ISBN 978-3-96147-534-6.

Band 396: Thomas Johann Luft
Komplexitätsmanagement in der Produktentwicklung - Holistische Modellierung, Analyse, Visualisierung und Bewertung komplexer Systeme
KTmfk, xiii u. 510 Seiten, 166 Bilder, 16 Tab. 2022.
ISBN 978-3-96147-540-7.

Band 397: Li Wang
Evaluierung der Einsetzbarkeit des lasergestützten Verfahrens zur selektiven Metallisierung für die Verbesserung passiver Intermodulation in Hochfrequenzanwendungen
FAPS, xxii u.151 Seiten, 72 Bilder, 22 Tab. 2022.
ISBN 978-3-96147-542-1.

Band 398: Sebastian Reitelshöfer
Der Aerosol-Jet-Druck Dielektrischer Elastomere als additives Fertigungsverfahren für elastische mechatronische Komponenten
FAPS, xxv u. 206 Seiten, 87 Bilder, 13 Tab. 2022.
ISBN 978-3-96147-547-6.

Band 399: Alexander Meyer
Selektive Magnetmontage zur Verringerung des Rastmomentes permanenterregter Synchronmotoren
FAPS, xv u. 164 Seiten, 90 Bilder, 18 Tab. 2022.
ISBN 978-3-96147-555-1.

Band 400: Rong Zhao
Design verschleißreduzierender amorpher Kohlenstoffschichtsysteme für trockene tribologische Gleitkontakte
KTmfk, x u. 148 Seiten, 69 Bilder, 14 Tab. 2022.
ISBN 978-3-96147-557-5.

Band 401: Christian P. J. Schwarzer
Kupfersintern als Fügetechnologie für Leistungselektronik
FAPS, xxvii u. 234 Seiten, 125 Bilder, 24 Tab. 2022.
ISBN 978-3-96147-566-7.

Band 402: Alexander Horn
Grundlegende Untersuchungen zur Gradierung der mechanischen Eigenschaften pressgehärteter Bauteile durch eine örtlich begrenzte Aufkohlung
LFT, xii u. 204 Seiten, 58 Bilder, 6 Tab. 2022.
ISBN 978-3-96147-568-1.

Band 403: Artur Klos
Werkstoff- und umformtechnische Bewertung von hochfesten Aluminiumblechwerkstoffen für den Karosseriebau
LFT, x u. 192 Seiten, 73 Bilder, 12 Tab. 2022.
ISBN 978-3-96147-572-8.

Band 404: Harald Schmid
Ganzheitliche Erarbeitung eines Prozessverständnisses von Tiefziehprozessen mit Ziehsicken auf Basis mechanischer und tribologischer Analysen
LFT, xiii u. 211 Seiten, 78 Bilder, 5 Tab. 2022.
ISBN 978-3-96147-577-3.

Band 405: Johannes Henneberg
Blechmassivumformung von Funktionsbauteilen aus Bandmaterial
LFT, viii u. 176 Seiten, 101 Bilder, 2 Tab. 2022.
ISBN 978-3-96147-579-7.

Band 406: Anton Schmailzl
Festigkeits- und zeitoptimierte Prozessführung beim quasi-simultanen Laser-Durchstrahlschweißen
LPT, xiii u. 157 Seiten, 84 Bilder, 7 Tab. 2022.
ISBN 978-3-96147-583-4.

Band 407: Alexander Wolf
Modellierung und Vorhersage menschlichen Interaktionsverhaltens zur Analyse der Mensch-Produkt Interaktion
KTmfk, x u. 207 Seiten, 69 Bilder, 10 Tab. 2022.
ISBN 978-3-96147-585-8.

Band 408: Tim Weikert
Modifikationen amorpher Kohlenstoffschichten zur Anpassung der Reibungsbedingungen und zur Erhöhung des Verschleißschutzes
KTmfk, xvii u. 258 Seiten, 91 Bilder, 9 Tab. 2022.
ISBN 978-3-96147-589-6.

Band 409: Stefan Götz
Frühzeitiges konstruktionsbegleitendes Toleranzmanagement
KTmfk, ix u. 276 Seiten, 127 Bilder, 13 Tab. 2022.
ISBN 978-3-96147-593-3.

Band 410: Markus Hubert
Einsatzpotenziale der Rotationsschneidtechnologie in der Verarbeitung von metallischen Funktionsfolien für mechatronische Produkte
FAPS, xviii u. 139 Seiten, 86 Bilder, 7 Tab. 2022.
ISBN 978-3-96147-603-9.

Band 411: Manfred Vogel
Grundlagenuntersuchungen und Erarbeitung einer Methodik zur Herstellung maßgeschneiderter Halbzeuge auf Basis eines neuartigen flexiblen Walzprozesses
LFT, ix u. 176 Seiten, 61 Bilder, 11 Tab. 2022.
ISBN 978-3-96147-605-3.

Band 412: Michael Weigelt
Multidimensionale Optionenanalyse alternativer Antriebskonzepte für die individuelle Langstreckenmobilität
FAPS, xv u. 222 Seiten, 89 Bilder, 38 Tab. 2022.
ISBN 978-3-96147-607-7.

Band 413: Frank Bodendorf
Machine Learning im Cost Engineering des Supply Managements
FAPS, xiii u. 165 Seiten, 75 Bilder, 13 Tab. 2023.
ISBN 978-3-96147-609-1.

Band 414: Maximilian Metzner
Planung und Simulation taktiler, intelligenter und kollaborativer Roboterfähigkeiten in der Montage
FAPS, xix u. 174 Seiten, 72 Bilder, 3 Tab. 2023.
ISBN 978-3-96147-611-4.

Band 415: Tina Buker
Ein Ansatz zur Reduktion produktinduzierter Nutzerstigmatisierung durch Förderung einer gleichermaßen gebrauchstauglichen wie emotionalen Produktgestalt
KTmfk, x u. 236 Seiten, 54 Bilder, 44 Tab. 2022.
ISBN 978-3-96147-613-8.

Band 416: Marlene Kuhn
Model-based Traceability System Development for Complex Manufacturing Applying Blockchain and Graphs
FAPS, xv u. 167 Seiten, 63 Bilder, 10 Tab. 2022.
ISBN 978-3-96147-615-2.

Band 417: Benjamin Lengenfelder
Remote photoacoustic sensing using speckle-analysis for biomedical imaging
LPT, xv u. 124 Seiten, 86 Bilder, 10 Tab. 2023.
ISBN 978-3-96147-617-6.

Band 418: Benjamin Pohrer
Analyse des Zusammenhangs zwischen dem tribochemischen Aufbau von Grenzschichten und der Ausbildung von White Etching Crack-Schäden
KTmfk, xv u. 258 Seiten, 103 Bilder, 10 Tab. 2023.
ISBN 978-3-96147- 621-3.

Band 419: Matthias Friedlein
Zuverlässigkeitsmethoden zur Beschleunigung von Qualifizierungsuntersuchungen für Steckkontakte
FAPS, xxv u. 162 Seiten, 98 Bilder, 7 Tab. 2023.
ISBN 978-3-96147-625-1.

Band 420: Thomas Stoll
Laser Powder Bed Fusion von Kupfer auf Aluminiumoxid-Keramiken
FAPS, xxvii u. 236 Seiten, 103 Bilder, 11 Tab. 2023.
ISBN 978-3-96147-631-2.

Band 421: Eric Eschner
Relation of Particle Motion and Process Zone Formation as a Basis for Sensing Approaches within PBF-LB/M
LPT, xiv u. 143 Seiten, 87 Bilder, 0 Tab. 2023.
ISBN 978-3-96147-633-6.

Band 422: Fanuel Mehari
Laser-induced Breakdown Spectroscopy (LIBS) as a diagnostics tool for biological tissue analysis.
LPT, xv u. 145 Seiten, 68 Bilder, 12 Tab. 2023.
ISBN 978-3-96147-641-1.

Band 423: Uwe Leicht
Ultraschallüberlagertes Umformen und Verstemmen von Stahlwerkstoffen
LFT, xi u. 165 Seiten, 65 Bilder, 6 Tab. 2023.
ISBN 978-3-96147-643-5.

Band 424: Thomas Braun
Potenzialanalyse der plasmabasierten, strukturierten Metallisierung thermoaktiver Oberflächen im industriellen Hausbau
FAPS, xvii u. 152 Seiten, 72 Bilder, 11 Tab. 2023.
ISBN 978-3-96147-653-4.

Band 425: Reinhardt Seidel
Modellbasierte Optimierung des Selektivwellenlötprozesses
FAPS, xxii u. 167 Seiten, 73 Bilder, 23 Tab. 2023.
ISBN: 978-3-96147-651-0.

Band 426: Matthias Lenzen
Maßgeschneiderte Werkstoffcharakterisierung für die numerische Auslegung von Blechumformprozessen
LFT, xi u. 187 Seiten, 77 Bilder, 13 Tab. 2023.
ISBN: 978-3-96147-663-3.

Band 427: Matthias Graser
Analyse lokaler Kurzzeitwärmebehandlungsmethoden zur Verbesserung des Umformverhaltens und der Bauteileigenschaften von Aluminiumstrangpresshohlprofilen
LFT, xi u. 169 Seiten, 81 Bilder, 1 Tab. 2023.
ISBN: 978-3-96147-666-4.

Band 428: Markus Lieret
Sicheres autonomes Flugrobotersystem für den Einsatz im Produktions- und Logistikumfeld
FAPS, xix u. 198 Seiten, 54 Bilder, 7 Tab. 2023.
ISBN 978-3-96147-668-8.

Band 429: Petar Vukovic
Simulation komplexer Kommunikationssysteme in der Fertigungsautomatisierung
FAPS, xiv u. 163 Seiten, 57 Bilder, 21 Tab. 2023.
ISBN 978-3-96147-673-2.

Band 430: Fabian Knieps
Finite Elemente Simulation dünnster Verpackungsstähle: Entwicklung einer geeigneten Charakterisierungs- und Validierungsstrategie
LFT, xix, 189 Seiten, 122 Bilder, 17 Tab. 2023.
ISBN 978-3-96147-689-3

Band 431: Julian Seßner
Multimodale Bildsegmentierung gering strukturierter Umgebungen für die Navigation am Beispiel eines Assistenzsystems für sehbeeinträchtigte Personen
FAPS, xxv, 203 Seiten, 57 Bilder, 25 Tab. 2023.
ISBN 978-3-96147-697-8

Band 432: Benjamin Samuel Lutz
Smart Manufacturing System for Process Optimization Regarding Deviations among Material Batches
FAPS, xix, 208 Seiten, 77 Bilder, 14 Tab. 2023.
ISBN 978-3-96147-703-6

Band 433: Michael Jüttner
Bewertung von Kantenpressungen auf Basis von Simulationen mehrfach überrollter elasto-plastischer Kontakte
KTmfk, xii, 162 Seiten, 59 Bilder, 7 Tab. 2024.
ISBN 978-3-96147-713-5.

Band 434: Sebastian Wiesenmayer
Untersuchungen zur Stoffflusssteuerung beim Fügen durch Umformen von hochfesten Aluminiumlegierungen mittels lokaler Kurzzeitwärmebehandlung
LFT, xii u. 197 Seiten, 81 Bilder, 19 Tab. 2024.
ISBN 978-3-96147-715-9.

Band 435: Clara-Maria Kuball
Grundlegende Untersuchungen zur umformtechnischen Herstellung von Halbhohlstanznieten aus hochverfestigenden Werkstoffen
LFT, viii u. 180 Seiten, 64 Bilder, 13 Tab. 2024.
ISBN 978-3-96147-717-3.

Band 436: Martin Roth
Sampling-based Tolerance-Cost Optimization: The Key to Optimal Tolerance Allocation
KTmfk, xxxvii u. 337 Seiten, 97 Bilder, 56 Tab. 2024.
ISBN 978-3-96147-719-7.

Band 437: Stephan Schirdewahn
Verbesserung des tribologischen Einsatzverhaltens im Presshärteprozess durch Verwendung maßgeschneiderter laserimplantierter Werkzeuge
LFT, viii u. 177 Seiten, 63 Bilder, 7 Tab. 2024.
ISBN 978-3-96147-721-0.

Band 438: Andreas Rohrmoser
Erarbeitung eines grundlegenden Verständnisses zum Fließpressen betriebsangepasster Verzahnungen für den Einsatz in der Materialpaarung Metall-Kunststoff
LFT, x u. 166 Seiten, 94 Bilder, 6 Tab. 2024.
ISBN: 978-3-96147-723-4.

Band 439: Andreas Selmaier
DMAICS-Zyklus zur Digitalisierung in produzierenden Unternehmen
FAPS, xv u. 185 Seiten, 73 Bilder, 19 Tab. 2024.
ISBN: 978-3-96147-733-3.

Band 440: Thomas Kistner
Entwicklung von Modellen der Oberflächenform für die Messunsicherheitsbestimmung von taktilen Koordinatenmessungen durch Simulation
FMT, xiii u. 134 Seiten, 64 Bilder, 9 Tab. 2024.
ISBN 978-3-96147-735-7.

Band 441: Fabian Dworschak
Selbstverstärkendes Lernen als Beitrag zur Automatisierung der Anpassungskonstruktion
KTmfk, x, 205 Seiten, 87 Bilder, 16 Tab. 2024.
ISBN 978-3-96147-739-5.

Band 442: Martin Killmann
Vorspannung und Ermüdung von Kaltmassivumformwerkzeugen für unrunde Bauteilgeometrien
LFT, ix u. 160 Seiten, 85 Bilder, 6 Tab. 2024.
ISBN 978-3-96147-741-8.

Band 443: Ann-Kathrin Wiemann
Beitrag zur Messunsicherheitsermittlung für die Messung großer Zahnräder zur Erweiterung des virtuellen Koordinatenmessgerätes der Physikalisch-Technischen Bundesanstalt
FMT, xxiv u. 133 Seiten, 41 Bilder, 22 Tab. 2024.
ISBN 978-3-96147-747-0.

Band 444: Andreas Jobst
Eigenspannungen beim Voll-Vorwärts-Fließpressen – Entstehung, Einstellung und Stabilität
LFT, ix u. 162 Seiten, 89 Bilder, 5 Tab. 2024.
ISBN: 978-3-96147-749-4.

Band 445: Martin Anton Kraus
Grundlagenwissenschaftliche Untersuchungen zum Kaltfließpressen kleinster metallischer Pin-Strukturen aus der Blechebene
LFT, x u. 191 Seiten, 64 Bilder, 10 Tab. 2024.
ISBN: 978-3-96147-757-9.

Band 446: Moritz Späth
Assessment of microcirculation
by shifted position-diffuse
reflectance imaging (SP-DRI)
LPT, xi u. 109 Seiten, 37 Bilder, 8
Tab. 2024.
ISBN 978-3-96147-759-3

Kurzfassung

Verschiedene Krankheiten wie Diabetes mellitus, Bluthochdruck oder Autoimmunerkrankungen können mit einem breiten Spektrum mikrovaskulärer Dysfunktionen, Mikroangiopathien und Mikrozirkulationsstörungen in Verbindung gebracht werden. Es ist daher davon auszugehen, dass die Überwachung der Mikrozirkulation zur Diagnose verschiedener lokaler und systemischer Durchblutungsstörungen und zur Überwachung kritisch kranker Patienten eingesetzt werden kann. Ein autarkes Messverfahren, das eine zuverlässige Erkennung von drohenden oder manifesten lokalen oder systemischen Durchblutungsstörungen ermöglicht, wäre somit von hohem Nutzen. In diesem Zusammenhang bietet Shifted Position-Diffuse Reflectance Imaging (SP-DRI) einen vielversprechenden Ansatz. Es handelt sich dabei um eine optische und damit nicht-invasive Methode, die auf diffus reflektiertem Licht fußt.

In dieser Dissertation wird die SP-DRI-Methode entwickelt, vorgestellt und die dahinter stehenden Algorithmen im Detail erläutert. Die Methode wird in Beziehung zu bereits bestehenden diagnostischen Ansätzen zur Beurteilung der Mikrozirkulation gesetzt. Der aktuelle Stand der Forschung zu SP-DRI wird beschrieben und das Zukunftspotenzial dieser Bildgebungstechnik aufgezeigt.

Der SP-DRI-Ansatz erwies sich sowohl simulativ als auch experimentell als in hohem Maße funktionell. Zuverlässige Informationen können in Echtzeit mit einem einfach zu implementierenden Aufbau gewonnen werden. SP-DRI könnte somit ein wichtiger Meilenstein auf dem Weg zu einer frühzeitigen und komfortablen Diagnose von Krankheiten sein, die mit der Konstriktion bzw. Dilatation von Arteriolen, Venolen oder dem Kapillarbett selbst zusammenhängen.

Multiple diseases like diabetes mellitus, hypertension or autoimmune diseases may be associated with a wide spectrum of microvascular dysfunctions, microangiopathies and microcirculatory disorders. It can thus be assumed that monitoring the microcirculation could be useful to diagnose various local and systemic circulatory disorders and could be used to monitor critically ill patients. A stand-alone measurement method that allows a reliable detection of impending or manifest local or systemic circulatory malfunctions would be of great value. In this context, shifted position-diffuse reflectance imaging (SP-DRI) offers a promising approach. It is an optical and thus non-invasive method based on the diffuse reflected light.

In this doctoral thesis, the SP-DRI method is developed and presented and the algorithms behind it are explained in detail. The method is set in relation to already existing diagnostic approaches for the assessment of the microcirculatory function. The current state of research on SP-DRI is described along with an outline of the future potential of this imaging technique. The SP-DRI approach proved to be highly functional both simulatively and experimentally. Reliable information can be obtained in real time with an easy to implement setup. SP-DRI may thus be an important milestone on the way to early and conveniently diagnosing diseases associated with the constriction or dilation of the arterioles, venules or the capillary bed itself.

ISBN 978-3-96147-759-3

FAU UNIVERSITY PRESS 2024